Multiscattering-enhanced optical probes for biosensing

THÈSE N^O 6655 (2015)

PRÉSENTÉE LE 29 MAI 2015
À LA FACULTÉ DES SCIENCES ET TECHNIQUES DE L'INGÉNIEUR
LABORATOIRE DE NANOPHOTONIQUE ET MÉTROLOGIE
PROGRAMME DOCTORAL EN PHOTONIQUE

ÉCOLE POLYTECHNIQUE FÉDÉRALE DE LAUSANNE

POUR L'OBTENTION DU GRADE DE DOCTEUR ÈS SCIENCES

PAR

Volodymyr KOMAN

acceptée sur proposition du jury:

Prof. J.-E. Moser, président du jury
Prof. O. Martin, Dr C. Santschi, directeurs de thèse
Prof. O. L. Muskens, rapporteur
Prof. P. Gehr, rapporteur
Prof. M. Gijs, rapporteur

EPFL

ÉCOLE POLYTECHNIQUE
FÉDÉRALE DE LAUSANNE

Suisse
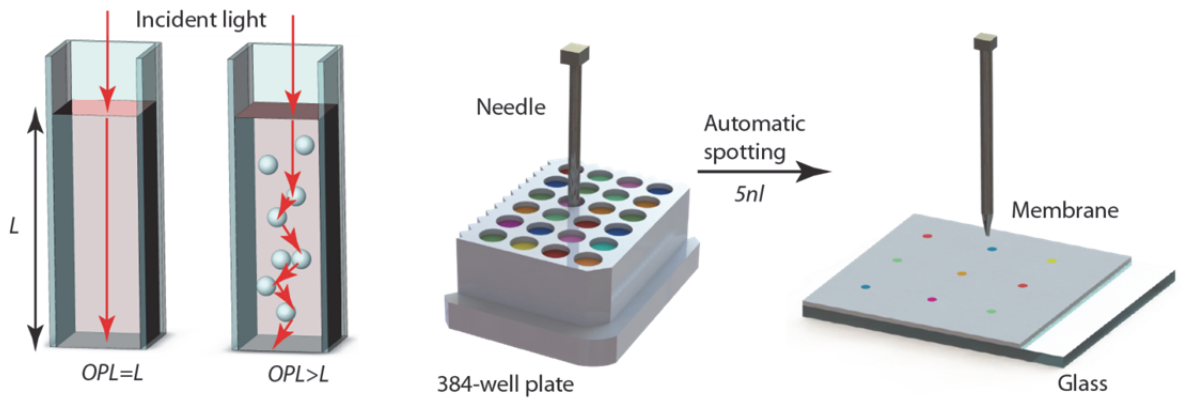2015

"There are no secrets that time does not reveal."

Jean Racine

To my parents;
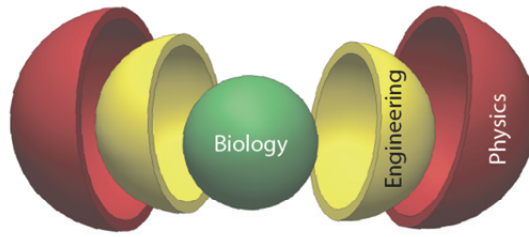
To Olia, who shaped my heart.

The graphical abstract depicts the interdisciplinary nature of this thesis, which combines physics, engineering and biology together. The main achievements are: an original technique for detecting minute quantities of analytes – multiscattering-enhanced absorption spectroscopy; a novel class of optical probes for highly sensitive and continuous biosensing experiments; a new portable oxidative stress sensor to assess the toxicity of nanomaterials; and finally, an advanced multi-layered microfluidic chip that paves the way for completely new ecotoxicological studies.
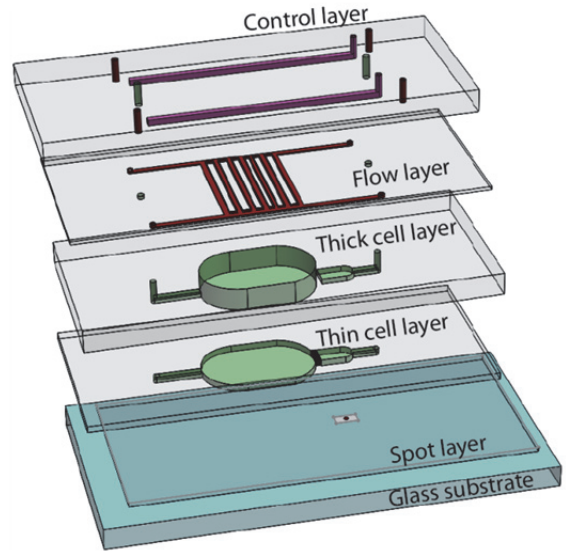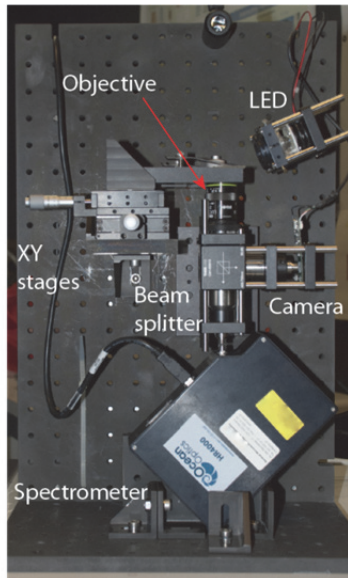
Incident light

L

$OPL=L$ $OPL>L$

Multiscattering-enhanced
absorption spectroscopy

Needle

Automatic
spotting

5nl

Membrane

384-well plate

Glass

Multianalyte optical probes
for biosensing

Biology   Engineering   Physics

Portable oxidative
stress sensor

Advanced microfluidics
for ecotoxicological studies

Objective   LED

XY
stages   Beam
splitter   Camera

Spectrometer

Control layer

Flow layer

Thick cell layer

Thin cell layer

Spot layer

Glass substrate

v

Abstract

Although reactive oxygen species (ROS) are an inescapable part of every living organism, we are at the beginning to understand their functions and mechanics. As of now, we know that ROS are involved in cell signalling, stress-response and defence against pathogens. New theories suggest that ROS also play an important role in various diseases and aging. However, further research is hindered by the fact that ROS are small and highly reactive molecules, making them very difficult to detect. Therefore, we need new sensitive and biocompatible tools with the ability to perform continuous measurements of ROS. The development of such a tool is the main objective of this thesis.

To realise such a sensor, I first developed an original scheme for sensitive absorption measurements – multiscattering-enhanced optical absorption or MEAS. MEAS benefits from the advantages of conventional absorption spectroscopy and relies on extending the optical path of light through the sensing volume by creating a multiscattering configuration. This way, higher sensitivity and lower limit of detection, compared to those of conventional absorption spectroscopy, were achieved. I further studied numerically the energy transfer from light into the absorbing background in the presence of a random medium. I discovered that there is a regime of maximal absorption in such a system, which corresponds to a specific filling factor of random medium. This is of particular interest not only for absorption spectroscopy, but also for improving solar cells and random lasers.

Having understood principles involved in sensing using random media, I designed and fabricated biocompatible and miniature optical probes: picomoles of the protein cytochrome c printed inside a porous matrix. The refractive index of porous membrane exhibits spatial variations leading to multiscattering of light and consequently to enhanced optical path lengths. Such probes can trace the dynamics of hydrogen peroxide (H_2O_2 – the most stable ROS) with a detection limit of 40 nM. Next, I have incorporated the developed optical probes into a portable oxidative stress sensor – a stand-alone device specifically designed for efficient and easy analysis in the field. As a potential application, I detected the dynamics of H_2O_2 release from the green alga *Chlamydomonas reinhardtii* exposed to either quantum dots or to TiO_2 nanoparticles. I further extended multiscattering-enhanced optical probes to continuous measurements of glucose and lactate – important metabolites in cells. The detection scheme is based on cytochrome c in conjunction with the respective enzymes. I obtained limits of detection of 240 nM and 110 nM for lactate and glucose, respectively. These values are at least one order of magnitude lower than the state of the art. To demonstrate the potential of these probes, I successfully traced the dynamics of micromolars of glucose uptake by

C.reinhardtii. Overall, the developed multifunctional detection scheme provides a powerful tool to study cellular biochemical processes.

After realising very sensitive optical probes with the possibility of continuous measurements, I used the developed portable sensor to study the dynamics of H_2O_2 released by *C.reinhardtii* under stress. Besides the tremendous importance for fundamental ROS biology, this is also a way to assess and compare the toxicity of different engineered nanomaterials (ENMs). Indeed, standard ecotoxicological methods are currently not applicable to describe the effect of ENMs. However, ENMs exhibit a correlation between the surface area and ROS-generating capabilities, which is often called an oxidative stress paradigm. In this context, I fabricated a multi-layered microfluidic chip with integrated microfluidic valves and microsieves that allows carrying out experiments with complex sequences of analytes exposure, mixing and rinsing. The response of algae to two Cd-based toxicants (ionic Cd and CdSe/ZnS quantum dots) was studied. As a result, I showed quantitative dynamics of extracellular H_2O_2, the recovery of cell homeostasis after short-term stress and the cumulative nature of two consecutive exposures. These experiments pave the way for completely new types of experiments for ROS biology as well as for the toxicity assessment of ENMs.

Résumé

B ien que les dérivés réactifs de l'oxygène (DRO) fassent inévitablement partie de tout organisme vivant, leurs mécanismes et leurs fonctions commencent seulement à être compris maintenant. Pour l'instant, nous savons que les DRO sont impliqués dans la signalisation cellulaire, la réponse des cellules au stress ainsi que la défense contre les pathogènes. De nouvelles théories suggèrent que les DRO jouent aussi un rôle important dans plusieurs maladies et dans le vieillissement. Néanmoins, des recherches plus approfondies sont entravées par le fait que les DRO sont des molécules petites et très réactives, rendant leur détection difficile. Il est donc nécessaire de trouver de nouveaux outils, sensibles et biocompatibles, capables de faire des mesures en continu. C'est l'objet principal de cette thèse.

Pour créer un tel capteur, j'ai d'abord développé un nouveau procédé sensible de mesure de l'absorption – l'absorption optique augmentée par multidiffusions (MEAS). La méthode MEAS a les avantages de la spectroscopie d'absorption et consiste à augmenter le chemin optique à travers le volume sensible en créant une configuration permettant de multiples diffusions. Grâce à cette technique, une meilleure sensibilité ainsi qu'une limite de détection plus basse (comparée aux autres méthodes conventionnelles de spectroscopie) a été obtenue. J'ai aussi étudié numériquement le transfert d'énergie entre la lumière et le milieu absorbant en présence d'un milieu aléatoire. J'ai découvert qu'il existe un régime d'absorption maximale, qui correspond à un certain facteur de remplissage du milieu aléatoire. Cette découverte est particulièrement intéressante non seulement pour la spectroscopie d'absorption, mais aussi pour améliorer les cellules solaires et les lasers aléatoires.

Une fois les principes relatifs à la détection avec un milieu aléatoire compris, j'ai conçu et créé des sondes optiques miniatures et biocompatibles: des picomoles de protéines cytochrome c imprimées dans une matrice poreuse. L'indice de réfraction des membranes poreuses possède des variations spatiales qui ont pour conséquence des diffusions multiples de la lumière et donc une augmentation du chemin optique. Ces sondes sont capables de détecter la dynamique de molécules de peroxyde d'hydrogène (H_2O_2, le plus stable des DRO) jusqu'à une limite de 40 nM. J'ai ensuite incorporé ces sondes dans un capteur portable de stress oxydant – un appareil autonome spécialement conçu pour des analyses efficaces sur le terrain. Dans l'idée d'une application potentielle, j'ai détecté la dynamique de la libération de H_2O_2 par l'algue verte *Chlamydomonas reinhardtii* exposée soit à des boites quantiques, soit à des nanoparticules de TiO_2. J'ai ensuite étendu la méthode de multidiffusion à une mesure continue de glucose et de lactate – des métabolites importantes. Le principe de détection est basé sur un mélange de cytochrome c avec les enzymes correspondantes. J'ai obtenu une limite de détection

de 240 nM et 110 nM pour le lactate et le glucose, respectivement. Ces valeurs sont plus petites d'au moins un ordre de grandeur comparées à l'état de l'art. Afin de montrer le potentiel de ces sondes, j'ai, avec succès, identifié la dynamique d'assimilation de micromoles de glucose par *C.reinhardtii*. De manière générale, le protocole de détection multifonction développé fournit un outil puissant pour étudier des processus cellulaires biochimiques.

Après avoir créé ces sondes optiques très sensibles permettant une mesure continue, j'ai utilisé le capteur portable pour étudier la dynamique de libération de H_2O_2 par *C.reinhardtii* sous stress. En plus de son importance majeure pour la biologie fondamentale des DRO, cette méthode permet aussi d'évaluer et de comparer la toxicité potentielle de différents nanomatériaux artificiels (ENMs). En effet, les méthodes standards d'écotoxicologie ne sont pour l'instant pas applicables pour décrire l'effet des ENMs. Cependant, les ENMs ont montré une corrélation entre leur surface et leur capacité à générer des DRO, ce qui est en général appelé paradigme de stress oxydant. Dans ce contexte j'ai introduit des puces microfluidiques multicouches munies de valves microfluidiques et de micro tamis qui permettent d'effectuer des expériences comprenant l'ajout, le mélange et le rinçage de séquences complexes d'analytes. La réponse de l'algue à deux toxiques basés sur le Cd (Cd ionique et des boites quantique CdSe/ZnS) est étudiée. Les résultats m'ont permis de montrer la dynamique quantitative de production d'H_2O_2 extracellulaire, le rétablissement de l'homéostasie des cellules après un stress de courte durée et la nature cumulative de deux expositions consécutives. Ces expériences ouvrent la voie pour de nouveaux types d'expériences pour la biologie des DRO ainsi que pour l'évaluation de la toxicité des ENMs.

Mots clefs: Milieu aléatoire; biodétection; cytochrome *c*; sonde améliorée multi-diffusions; toxicité; stress oxydant; dérivées réactifs de l'oxygène; microfluidique; peroxyde d'hydrogène; glucose; lactate; algue; mesure continue; spectroscopie d'absorption.

Анотація

Незважаючи на те, що реактивні форми кисню (РФК) є невід'ємною частиною кожного живого організму, ми тільки починаємо розуміти їхні функції і механізми. Наразі відомо, що РФК приймають участь у сигнальних клітинних системах, у реакції на подразнення та захисті від інфекційних збудників. Згідно новітніх теорій, кількість РФК визначає перебіг різноманітних хвороб та швидкість процесу старіння. Однак, подальше вивчення ускладнене тим, що РФК є малими і дуже реактивними молекулами, що робить їх виявлення дуже важким. Отже, нам потрібні нові дуже чутливі і біосумісні прилади зі здатністю до неперервних вимірювань РФК. Розробка таких приладів і є головним завданням даної роботи.

Щоб створити такі сенсори, спершу я розробив оригінальний метод для чутливих поглинальних вимірювань – оптичне поглинання підсилене мультирозсіянням (MEAS). MEAS базується на створенні мультирозсіювального режиму, який подовжує оптичний світловий шлях через вимірювальний зразок, водночас зберігаючи всі переваги звичайної поглинальної спектроскопії. Таким чином, у порівнянні зі звичайною поглинальною спектроскопією, чутливість вимірювань підвищується, а межа виявлення покращується. Також я чисельно вивчив передачу енергії від світла до поглинаючого зразка у присутності випадкового середовища. В такій системі я відкрив існування режиму максимального поглинання, що відповідає певному фактору заповнення випадкового середовища. Це відкриття є важливим не тільки для поглинальної спектроскопії, але також для покращення сонячних батарей та випадкових лазерів.

Зрозумівши принципи виявлення речовин на основі випадкових середовищ, я спроектував і виготовив біосумісні і мініатюрні оптичні проби: пікомолі білку хромосоми c надруковані всередині пористої матриці. Показник заломлення пористих матриць зазнає просторових варіацій, що створює ефект мультирозсіювання світла, яке подовжує його оптичний шлях. Такі проби можуть вимірювати динаміку гідроксиду водню (H_2O_2 – найбільш стабільний РФК) із межею виявлення 40 нМ. Я також інтегрував розроблені оптичні проби у портативний сенсор для окислювального стресу. Цей автономний прилад був спеціально розроблений для ефективного і простого аналізу. Для демонстрації я

виміряв динаміку H_2O_2 випущеного зеленими водоростями *Chlamydomonas reinhardtii* внаслідок контакту із квантовими точками і наночастинками TiO_2. В подальшому я також розробив покращені мультирозсіюванням оптичні проби для неперервного вимірювання глюкози та лактози – важливих клітинних метаболітів. Схема вимірювання базується на хромосомі *c* у поєднанні із відповідними ферментами. Я отримав межі виявлення 240 нМ і 110 нМ для лактози і глюкози. Ці значення є щонайменше вдесятеро меншими у порівнянні з іншими сучасними розробками. Для демонстрації я успішно відслідкував динаміку поглинання мікромолів глюкози клітинами *C.reinhardtii*. Розроблений мультифункціональний вимірювальний пристрій є потужним методом для вивчення біохімічних процесів.

Після створення дуже чутливих оптичних проб із можливістю неперервних вимірювань, я використав портативний сенсор для вивчення динаміки H_2O_2 випущеного *C.reinhardtii* під час стресу. Окрім величезного значення для фундаментальної РФК біології, така робота відкриває шлях для вимірювання та порівняння токсичності різних наноматеріалів (НМ). Дійсно, стандартні токсикологічні методи не в силі описати ефект НМ. Однак, НМ мають зв'язок між площею поверхні і здатністю до створення РФК, що часто називають парадигмою окислювального стресу. Саме тому я розробив багатошаровий мікрогідродинамічний прилад з інтегрованими мікрогідродинамічними клапанами і ситами, які дозволяють проводити експерименти зі складними послідовностями вводу, змішування і виводу токсичних речовин. Було вивчено реакцію водоростей на дві токсичні речовини (іонний Cd та CdSe/ZnS квантові точки). Результати проведених експериментів показали динаміку H_2O_2, відновлення клітинного гомеостазу після короткотривалого стресу і сукупну природу двох послідовних вимірювань. Ці дослідження відкривають шлях до цілковито нових видів експериментів у РФК біології, а також новітній метод для вивчення токсичності НМ.

Ключові слова: біосенсор, хромосома *c*, оптичні проби покращені мультирозсіянням, токсичність, окислювальний стрес, реактивні форми кисню, мікрогідродинаміка, пероксид водню, глюкоза, лактоза, водорості, неперервні вимірювання, поглинальна спектроскопія.

Contents

Chapter 1   Introduction and thesis objectives

Significant amounts of oxygen started to appear in our environment over 2.2 billion years ago, mostly with the evolution of O_2 produced by photosynthetic organisms [1]. Since an O_2 molecule has two unpaired electrons with the same spin quantum number, it is a free radical [2]. This spin restriction makes O_2 prefer to accept only one electron at a time, leading to the generation of $O_2\bullet-$, which is a prime example of reactive oxygen species (ROS). In general, ROS are chemically reactive molecules containing activated oxygen such as $HO\bullet$, H_2O_2, $HO_2\bullet-$, $ROO\bullet$ and $RO\bullet$, where R stands for any alkyle group [2, 3]. ROS are produced continuously as byproducts of various metabolic pathways in different cellular compartments such as chloroplasts, mitochondria and peroxisomes [4, 5]. Although ROS have been an inevitable part of our life since ages, we have only recently started to discover their importance and functions. For instance, in 1908 Warburg discovered increased consumption of oxygen by sea urchin eggs [6]. Only in 1978, this was explained by the H_2O_2 producing respiratory bursts [7]. In 1929, Fleming discovered that *Penicillium notatum* releases an antibacterial product, but it took another 78 years before it was discovered that many antibiotics, including penicillin, partly work by causing bacteria to generate ROS [8]. Nowadays it is known that in biological systems ROS keep a fragile equilibrium with antioxidants (AOX) securing cellular homeostasis [2]. ROS are involved in different physiological processes including stress-response, signaling and pathogen defense [2, 9-13]. Imbalanced generation of ROS, called oxidative stress, plays an important role in many diseases and aging [14-18]. Our current knowledge about ROS biology is not complete, but represents a very promising and fascinating field: we can potentially step into physiological and medical advances with better understanding of ROS, their functions and dynamics [3, 12].

As the subject of ROS is very broad, in this thesis, I focus on stress-related ROS generation in aquatic microorganisms. This topic is interesting not only from the fundamental biological perspective, but also has immediate and very important practical aspects: ROS generation and oxidative stress are currently one of the best accepted paradigms to assess and compare the toxicity potentials of different engineered nanomaterials (ENMs) [19]. In this context, aquatic microorganisms are expected to be the primary targets for ENMs released in the environment [20].

By some estimates, nanotechnology promises to exceed the impact of the Industial Revolution [19]. ENMs have become a versatile new class of materials that are already

applied in an extremely broad range of industrial and consumer products including electronics, packaging, optics, ceramics, agriculture, textiles, paints, cosmetics, personal care products, biotechnology, pharmaceutics, energy, automotive and aerospace [20-24]. Such a success is governed by the unique material properties of ENMs that directly arise from their nanometer size and distinctly set them apart from equivalent bulk materials [25, 26]. These material properties have made ENMs so appealing for their exploitation but, at the same time, also a real challenge for hazard assessment and the currently used standard toxicity methods [27-29]. So far, no parameter has been identified that best describes the dose-response relationship for ENMs toxicity tests [30, 31]. Expressing the ENMs dose in terms of surface area instead of mass shows a promising correlation with toxicity [32]. However, it is broadly accepted that the underlying toxicity mechanisms of ENMs are generally poorly understood and that there is a severe lack of data linking the particles toxicity with the properties of the ambient medium [19, 33]. To fill this gap, the Swiss National Science Foundation launched an interdisciplinary program NRP 64 "Opportunities and risks of nanomaterials", and this thesis was framed within this program.

In addition to their direct effects on biological entities (dissolution, Fenton chemistry, redox cycling, electron-donor/acceptor groups, etc.), ENMs have also shown a correlation between the surface area and their ROS-generating capability [34-38]. This is presently the best developed paradigm to explain the toxic effects of ENMs. Briefly, ENMs have the potential to stimulate ROS generation and break the balance between ROS and AOX, creating oxidative stress [39]. According to the hierarchical oxidative stress hypothesis, the lowest level of oxidative stress is associated with the induction of antioxidant and detoxification enzymes [40, 41]. At higher levels of oxidative stress, this protective response is overtaken by inflammation and cytotoxicity. Prolonged or chronical oxidative stress can lead to the oxidative damage of subcellular components, including membrane and DNA, and ultimately to cell death [42-45].

With this in mind, the aim of this thesis is to provide a novel tool to detect ROS and to study ROS dynamics induced by toxicants in aquatic microorganisms. The working principle is based on another fascinating subject – light propagation in random media.

Historically, random media first received attention as an obstacle: astronomers trying to image distant galaxies were hindered by light scattered by the interstellar medium [46]. Additionally, biologists struggled with a similar problem – imaging through a turbid tissue for sensing and medical diagnostics [47, 48]. Since then, the field of random media has grown immensely. After the fundamental experiments, the discovery of Anderson localization for electrons [49] has stimulated works on strong localization in optics [50-55]. In parallel, numerous works on weak localization have also emerged [56-61]. Recent developments in adaptive wavefront shaping techniques have opened new possibilities for experiments on the highly transmitting (or so-called open) channels in random media [62-65], light focusing below the diffraction limit [66, 67] and coherently enhanced absorption [64]. From the application perspective, works are devoted to random lasing [68-72] and imaging through turbid media [73-77]. Random media also offer a possibility to improve photovoltaic devices by enhancing their absorption and

increasing the optical path of light [78-82]. Finally, elongated optical paths – present in random media – recently paved the way for new applications in gas camera sensors [83]. In this context, the thesis concentrates on using random media to extend sensing applications further. The main principle will rely on embedding absorbing analytes in non-absorbing random media.
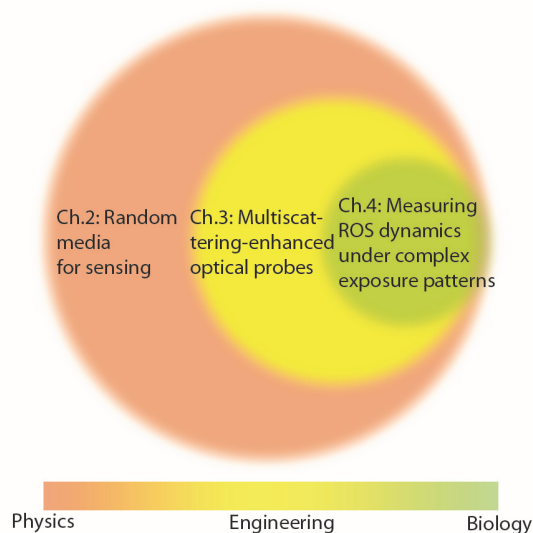
Figure 1.1. **Illustration of the different thesis chapters.** Circles sizes represent moving to more specific sensing applications as the thesis progresses. Colors indicate the topical transition from physics to biology through engineering.

The main objectives of this thesis are the following:

1. To optimize random media for sensing applications.

2. To develop a sensitive and continuous, multiscattering-enhanced optical probe to detect ROS.

3. To develop a stand-alone setup for oxidative stress measurements.

4. To develop microfluidic chips that can hold aquatic microorganisms together with the sensing probe in order to perform complex exposures to toxicants.

5. Using the developed platform, to gain new insights into the ROS dynamics induced by toxicants in aquatic microorganisms.

The thesis is organized as follows. In Chapter 2, I give a brief overview of absorption spectroscopy and present an extension called multiscattering-enhanced absorption spectroscopy, based on light propagation in random media, to improve the detection of

low concentration analytes. I further discuss how to engineer random media to maxim-maximize the energy transfer from the incident light to the absorber. I start Chapter 3 with an overview of the existing techniques to detect ROS. Next, I present a multiscattering-enhanced optical probe to detect H_2O_2 down to 40 nM as well as a portable oxidative stress sensor. I also extend this platform to multianalyte and multiplexed measurements for glucose and lactate. In Chapter 4, I combine the developed optical probe with a multi-layered microfluidic chip to study the dynamics of ROS during the exposure of aquatic microorganisms to ionic Cd and CdSe/ZnS quantum dots. In the last chapter I conclude and provide an outlook for further research.

Chapter 2 Multiscattering in random media for sensing applications

An original scheme for sensitive absorption measurements, particularly well-suited for low analyte concentrations, is presented in the first part of this chapter. The technique is based on multiscattering-enhanced absorption spectroscopy and benefits from the advantages of conventional absorption spectroscopy: simplicity, rapidity and low costs. The technique relies on extending the optical path through the sensing volume by dispersing dielectric beads in the solution containing the analytes of interest. This results in multiple scattering of light, which increases the optical path length through the sample. The influence of different parameters describing the scattering medium is investigated in detail experimentally and numerically, with a very good agreement between the two. The investigated parameters can be effectively used to tailor the enhancement for specific applications and analytes.

In the second part of this chapter, I engineer random media so that the absorption for a given volume is maximized. In particular, I study the influence of the geometrical and scattering properties of the system on the absorption. By combining a random medium with an open photonic cavity, I numerically demonstrate a 23-fold enhancement of the absorbed energy. These findings are of particular interest for sensing applications as well as for solar cells, light trapping platforms and random lasers.

2.1   Introduction

Absorption spectroscopy is a fast, simple and inexpensive method for the detection of biomolecules such as nucleotides, proteins, steroids, antibiotics, amino acids and terpenoids, as well as pharmaceuticals, pesticides or hydrocarbons [84-92]. This diversity makes absorption spectroscopy a tool of choice for a broad range of applications in research, medical laboratories and industry. Additionally, it complements separation techniques such as high performance liquid chromatography [93] and capillary electrophoresis [94] to identify and quantify analytes. Recently, its field of applications has been broadened by novel assays, where molecules are tagged to quantum dots, nanoparticles or fluorescent dyes to enhance the assay performance [95-98]. Alternative methods for detecting biochemical entities such as mass spectroscopy [99] and electrochemistry [100] have their own limitations. Mass spectrometry requires

extensive equipment while in electrochemistry the analyte must undergo a redox reac-reaction, which limits the materials where it can be applied. Further alternatives are chemoluminescence [101] and fluorescence [102]. However, these techniques can result in bleaching and require specific and often expensive optical filters and, furthermore, invasive chemical species which interact with the sample of interest. Due to all these limitations associated with competing techniques, absorption spectroscopy is a commonly used detection method.

In conventional absorption spectroscopy, the light beam passes through the absorbing sample and the spectral intensity of the light is measured before (I_0) and after the sample (I). Knowing the absorption coefficient of the analyte under study, its concentration can be determined using Beer-Lambert's law [103]:

$$I = I_0 exp(-\alpha Cl), \tag{2.1}$$

where C is the molar concentration, l the optical path length of light and α the molar absorption coefficient. The minimal detectable concentration is determined by the relative change of intensity $\Delta I/I_0 = (I_0 - I)/I_0$, which depends on the equipment used, the amount of averaging, etc. $\Delta I/I_0$ is typically limited for spectroscopic measurements to $\sim 10^{-4}$ or using specific data analysis algorithms to $5 \cdot 10^{-6}$, while smaller signals cannot be distinguished anymore from the noise [104, 105]. For many practical applications the concentrations of the analyte provide intensity changes lying below the limit of detection (LOD). For example, a typical dye – rhodamine 6G – has the strongest absorption of $116000 \text{ cm}^{-1} \cdot \text{M}^{-1}$ at the wavelength $\lambda = 532$ nm [106]. The detection of 0.1 nM rhodamine would require an optical path of 86 cm with a $\Delta I/I_0 \sim 10^{-3}$ accuracy.

The sensitivity of absorption spectroscopy can be improved by increasing the optical path of light (OPL) and several techniques have been developed to do so: photoacoustic spectroscopy [107], thermal-lensing effects [108], liquid-waveguide capillary cells [109], cavity enhanced spectroscopy [110], integrating sphere [111] and attenuated total reflection spectroscopy [112]. Unfortunately, all these techniques require rather expensive and sophisticated equipment and a simple technique able to push the LOD below the limit of conventional absorption spectroscopy is of great interest. In the following, I demonstrate both experimentally and numerically that disordered media, which increases the OPL via multiscattering, can significantly improve the LOD for absorption spectroscopy and, therefore, can be utilized in efficient sensing applications.

2.2 Monte Carlo simulations for light propagation in random media

Scattering of light in random media is a complex phenomenon, especially when the size of the scatterer is comparable to the wavelength of the light, as is the case here. The scattering for an individual particle in such a system is shown in Fig. 2.1a. The total scattering cross section of the system results from the superposition of the individual

amplitudes, making the problem rather complicated. Transport theory (or diffusion approximation) [59, 80, 113] and probabilistic Monte Carlo simulations [114, 115] are the two main numerical methods used to tackle this problem. While the former method requires the knowledge of the macroscopic parameters of the system such as density and diffusion coefficient, the latter resorts to microscopic parameters such as distance between the particles and their size. Here, I use the Monte Carlo procedure to get a better understanding of the multiscattering phenomenon and to study the influence of the various parameters describing the PS beads dispersion in the absorbing medium. This choice is dictated by the broad range of the validity of Monte Carlo procedure as compared to the diffusion theory, which is generally faster, but is only valid in the strongly scattering regime.

The scattering process is simulated as follows. I divide the incident light into wavepackets, which are sequentially launched into the system. Wavepackets have been chosen instead of single photons in order to simulate the absorption along the OPL. To describe each scattering event between wavepackets and particles, I introduce a probability function $p(\theta)$, which describes the angular dependence of the scattering. This function depends on the scattering cross section σ of the particle; and is approximated by the Henyey-Greenstein distribution [46], [116]:

$$p(\theta) = \frac{1-g^2}{4\pi(1+g^2-2g\cos\theta)^{3/2}},$$

(2.2)

where $g = <\cos\ \theta>$ is the average scattering angle [117]. The wavepacket continues to propagate after the scattering event in a randomly chosen direction determined using the probability function that reproduces the angular dependence of the scattering (Fig. 2.1b). Thus, scattering from a large ensemble of wavepackets resembles a realistic scattering distribution. Since the absorption of polystyrene beads (which are used as scatterers in this work) is very weak and, moreover, is cancelled out by the appropriate baseline in the experiment, it can be neglected in the simulations. Hence, only absorption from the background medium between two successive scattering events is considered.

Next, I proceed to describe a probabilistic approach based on a Monte Carlo scheme. A validation of this framework can be found elsewhere [114, 118]. The random medium consists of spherical scatterers with diameter d distributed homogeneously in an absorbing background. The simulation is performed on a finite volume of the random medium with the form of cuboid (Fig. 2.1c,d). Incident light is launched though the central point of one of the surfaces at normal incidence unless stated otherwise. Between two successive scattering events the wavepacket travels in a straight line losing a part of its energy through absorption in the background according to Beer-Lambert's law [119]. The mean free path of light l_{free} between two successive scattering events is determined as:

$$l_{free} = \frac{2d}{3FQ_{sca}},$$

(2.3)

where $F = \pi d^3 C^{PS}/6$ is the filling factor, C^{PS} the concentration of scatterers and Q_{sca} the scattering efficiency for each individual scatterer. The transport mean free path is de-determined as: $l^* = l_{free}/(1-g)$. Q_{sca} and g are calculated using Mie theory [118]. I assume that the interparticle distance p follows the random distribution expressed by: $p = -l_{free} \log \Sigma$, where Σ is sampled uniformly between 0 and 1. When a wavepacket experiences a scattering event from a particle, it changes its direction.
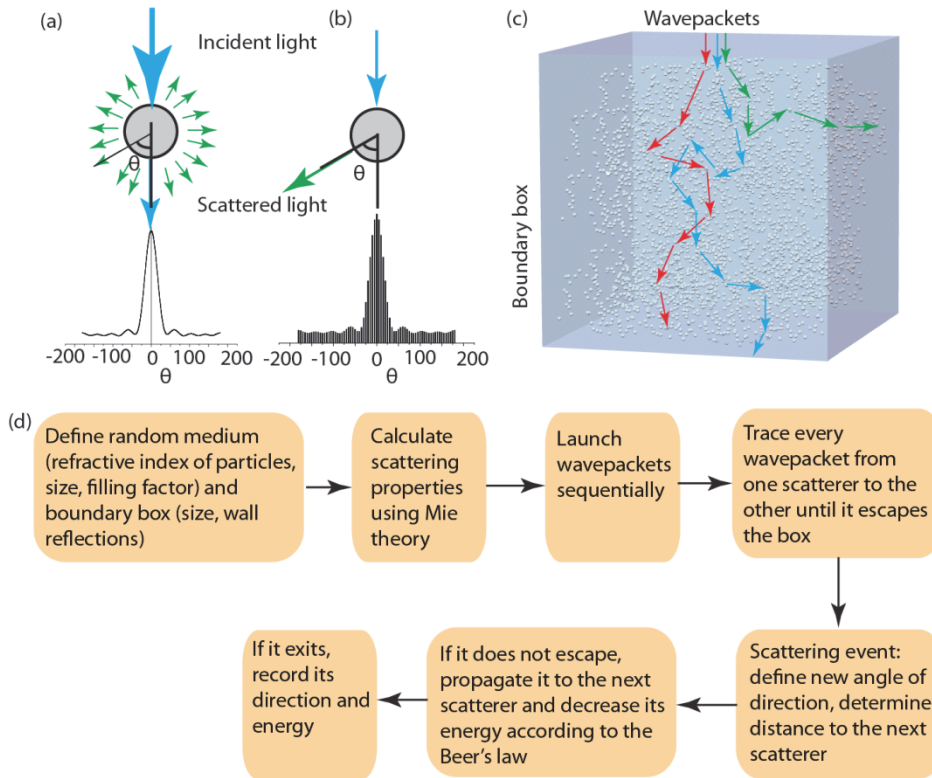
Figure 2.1. **Light propagation in a random medium.** (a) Schematic illustration of the Mie scattering process: the incident light is scattered by the particle in all directions. The graph shows the scattering angle θ distribution. (b) Simulated scattering process: the incident light is scattered probabilistically in one direction, following Mie theory. A collection of wavepackets leads to the probability distribution shown in the graph, which agrees well with the Mie scattering distribution in (a). (c) Schematic drawing of three wavepackets propagating through a box with a random scattering medium. (d) Schematic illustrating the principal steps involved in the computation of wavepackets propagating through random medium.

The wavepackets are sequentially traced until they reach the box boundaries, where the directions and energies of such output wavepackets are recorded. The total initial ener-energy of all wavepackets is set to unity for normalization purposes. The transmitted energy T (respectively, reflected energy R) is calculated as the total energy of wavepackets that exit the system with a zero or positive (respectively, negative) scalar product between their direction and the incident light direction. In this way, wavepackets that exit the side walls of the medium are also accounted for in transmission and reflection. Finally, the absorbed energy E_{abs} is calculated as the difference between incident energy and the sum of reflected and transmitted energies. The optical path of light (OPL) for transmitted OPL_T (respectively, reflected OPL_R) direction is calculated by taking the ratio of transmitted (respectively, reflected) light energy to the corresponding energy in the absence of the absorber T_0 (respectively, R_0) and using Beer-Lambert's law: $OPL_T = -log(T/T_0)/\alpha$, where α is the absorption coefficient and $OPL_R = -log(R/R_0)/\alpha$. Unless otherwise stated, I use the following values for the simulation parameters: the spherical scatterers have a diameter $d = 0.5\,\mu m$; the surrounding medium is a solution with refractive index $n = 1.33$. The simulations have been carried out at the absorption peak wavelength (λ_d) of the solution of interest (e.g., $\lambda_d = 570\,nm$ for phenol red).

Let us now briefly discuss the validity of Beer-Lambert's law in the random medium. The expression for the intensity of the collected light can be written as the sum of the individual packets having initial intensity I_{packet} and travelling individual paths with different lengths l_i: $I = I_{packet}\sum_i e^{-\alpha C l_i}$. In the absence of scatterers all wavepackets trajectories have the same length, thus the sum represents a single exponential function (Eq. (2.1)). In the case of random media, characterized by trajectories having different l_i, an exponential function can be constructed by introducing a function G: $I = I_0 e^{-\alpha C G}$. The parameter G represents a virtual OPL, which allows quantification of the optical enhancement for every individual configuration of the random media. For very low absorption, the contribution of every wavepacket can be approximated as $e^{-\alpha C l_i} \approx 1 - \alpha C l_i$ (there are always some wavepackets, which have very long l_i, but there contribution is negligible). In this case, the absorbance in random medium (A_{rm}) can be written as $A_{rm} = \alpha C G$, which obviously follows Beer-Lambert's law.

Note that this approach does not hold for densely packed or so-called short-range random media [120]. In that case, densely packed scatterers modify the refractive index of their neighbours and influence the Mie scattering properties of each particle. The short-range regime is reached when l_{free} becomes smaller than the diameter d of the scatterer. I refer to low scatterer concentrations if the following relation holds: $l_{free} \gg d$, whereas moderate concentrations are associated with $l_{free} \gtrsim d$. In this thesis, I am working in the former regime with l_{free} ranging from 5 to 25 μm as compared to $d = 0.5\,\mu m$, therefore, the model can be applied. On the other hand, l_{free} will be much smaller than the geometrical thickness L, which fulfills the condition that wavepackets propagating in such a medium experience multiscattering.

2.3 Multiscattering-enhanced absorption spectroscopy

Here, I present a simple, tunable and sensitive optical method, based on multiscattering in random media, for measuring low concentrations of dispersed or dissolved analytes. Examples of a random media are thick membranes with high filling factor used by Svensson *et al.* [83]. Those membranes exhibit large OPLs and show an excellent performance for gas detection. However, similar porous membranes show an increased response time for measurements in liquids, due to slow diffusion of the analyte [121]. Hence, diffusion of the analyte into the random medium is a limiting factor for dynamic measurements performed in liquids. In this section, the multiscattering configuration is achieved by introducing an appropriate density of dielectric spheres inside a solution containing the analyte of interest. In such a configuration the diffusion is not an issue because active mixing can be performed and consequently a rapid diffusion of the analyte can be achieved. This multiscattering-enhanced absorption spectroscopy (MEAS) allows us to enhance the absorbance with respect to conventional absorption spectroscopy for a broad variety of analytes. Specifically, I demonstrate this technique for phenol red, 10 nm gold nanoparticles and envy green fluorescent dyes. By applying MEAS to a hydrogen peroxide bioassay I show that the sensitivity of the measurements can be increased and the optimal optical path length can be determined. This way, I show both experimentally and numerically that variations in size, concentration, as well as geometrical thickness of the scattering medium, control the optical path enhancement. The possibility of OPL tuning provides a way to design disordered media adapted to the application at hand (limit of detection, diffusion, sensitivity, robustness).

2.3.1 Chemicals

DMEM (Dulbecco's modified Eagle's medium) medium with phenol red (40 µM), hexanedithiol, 10 nm gold particles and envy fluorescence dye encapsulated in 60 nm latex beads are purchased from Life Technologies, Sigma Aldrich, BBI solutions and Bangs Laboratories, respectively. The polystyrene beads (PS) microsphere kit is purchased from Polysciences and the colorimetric assay for hydrogen peroxide detection is purchased from Cell BioLabs (OxiSelect). Since the DMEM medium without phenol red does not absorb in the visible range, in our experiments I attribute the absorption of the DMEM mixture with phenol red to the corresponding concentration of phenol red. In the following, when I mention "phenol red" dilutions, I refer to the dilution of pure phenol red, not to dilutions of the mixture DMEM with phenol red.

All dilutions are done with deionized water if not stated otherwise. Different PS beads diameters and concentrations are used to investigate the influence of multiscattering, as described in the text. It should be noted here that PS beads do not aggregate thanks to the presence of negatively charged surfactants (e.g. <0.1 % sodium dodecyl sulfate, according to the supplier).

2.3.2   Optical measurements

The spectral measurements are carried out in transmission mode using a 20x objective (UPlanFL 20x, Olympus, NA = 0.41) and inverted microscope (IX71, Olympus) coupled to a monochromator (TRIAX 550, Horiba Scientific) and a liquid nitrogen cooled CCD camera (Symphony, Horiba Scientific). The typical integration time to record one spectrum is on the order of 300 ms. Absorption spectra are normalized with reference spectra obtained by measuring the same solution without the absorbing element; i.e. pure water is used as reference spectrum for conventional absorption spectroscopy, while water with dispersed PS beads is used as the reference for MEAS. It has to be mentioned that not the entire spectrum, but only the values at the absorption peaks are used as reference points: values at $\lambda = 520$ nm for gold nanoparticles, at $\lambda = 530$ nm for envy green dye, at $\lambda = 570$ nm for phenol red and at $\lambda = 595$ nm for H_2O_2 bioassays. Standard 384-well plates containing cuvettes with a 3.3×3.3 mm^2 square cross-section are used as sample chamber, except for the experiments with varying thicknesses, where 96-well plates with a 7.3×7.3 mm^2 cross section are used. This precaution prevents crosstalk between neighboring cells. For 40 µl samples I did not observe crosstalk in 384-well plates, but experiments with a 1 cm optical path, require a 96-well plate with a larger cross-section to effectively suppress crosstalk. Using such wells demands only small volumes of analyte, which is advantageous for expensive biological samples. However, MEAS can also be implemented in larger absorption spectroscopy cuvettes.

2.3.3   Improving the limit of detection

When light goes through the cuvette containing a homogeneous solution, its optical path is determined by the geometrical thickness L of the sample. In the following, absorption enhancement refers to a configuration corresponding to the standard absorption spectroscopy. If the sample is inhomogeneous, i.e. exhibits noticeable spatial variations of the refractive index, the passing light undergoes multiscattering. Consequently the OPL is increased as schematically illustrated in Fig. 2.2a. In this work, this is achieved by adding spherical PS particles to the solution containing the analyte. Hence the OPL becomes longer than the geometrical thickness of the sample, resulting in multiscattering-enhanced absorption spectroscopy.

Let us first illustrate this approach by measuring the transmission through a cuvette containing 40 µl of 0.6 µM phenol red solution diluted in water, corresponding to a geometrical thickness $L = 3.7$ mm. The base line is determined by transmission measurements trough the cuvette containing the same volume of pure water. In the second cuvette, I prepared a mixture containing 0.6 µM phenol red and 0.6 nM of PS beads with a diameter of $d = 0.5$ µm. To determine the base line for this configuration I recorded the transmission spectrum of a 40 µl dispersion containing the same concentration of PS beads in pure water. I obtained two normalized transmission spectra for the same concentration of phenol red solution. As displayed in Fig. 2.2b, the absorption dip of phenol red is much less pronounced in the absorption spectroscopy

11

measurement than in the MEAS configuration, which clearly indicates in the latter case an enhanced absorption due to multiscattering.
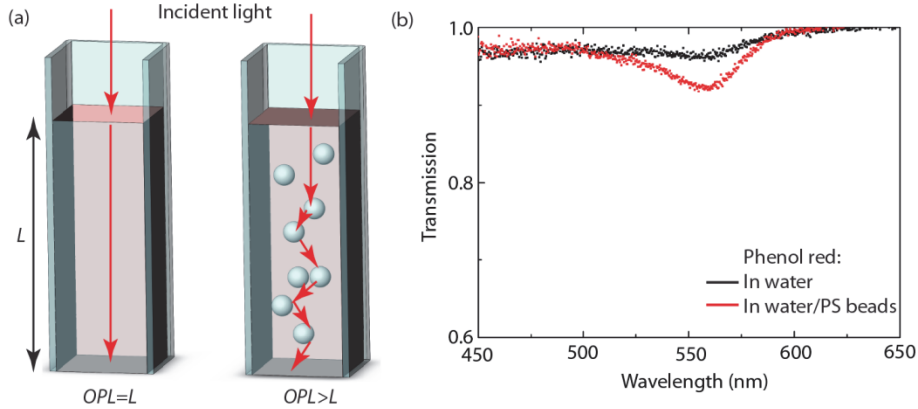
Figure 2.2. **MEAS configuration.** (a) A schematic drawing of the absorption spectroscopy and the MEAS configurations. The optical path length (OPL) is increased by the presence of the scatterers in the MEAS configuration.(b) Normalized transmission measurements for the two configurations: 0.6 μM phenol red in water and 0.6 μM phenol red with 0.6 nM PS beads ($d = 0.5$ μm) in water.

I quantified the enhancement provided by MEAS and compared the performance of this technique with conventional absorption spectroscopy for three different analytes: phenol red, 10 nm gold nanoparticles and envy green fluorescence dye. Phenol red is a commonly used molecule for colorimetric measurements to determine the pH of a solution, since the magnitude of its absorption dip at $\lambda = 570$ nm is sensitive to the pH [122]. Following the same experimental procedure as described above for Fig. 2.2, I measured the unitless absorbance A for different phenol red concentrations, using Eq. (2.4):

$$A = -\ln\left(\frac{I}{I_0}\right) = \alpha C l, \tag{2.4}$$

where I, respectively I_0, is the measured intensities of the outcoming light, respectively the baseline. The measurements are carried out using water and two mixtures containing 0.5 μm PS beads in two different concentrations: $C_1^{PS} = 0.6$ nM and $C_2^{PS} = 3.0$ nM. Figure 2.3a shows that the absorbance A is proportional to the phenol red concentration, which is in agreement with Beer-Lambert's law. In order to quantify the enhancement of the absorbance, I introduced a factor k defined as the ratio between the absorbance of the analyte in water and in water/PS beads dispersion for a given wavelength:

$$k = A_{In\ water/PS}/A_{In\ water}. \tag{2.5}$$

The presence of PS beads increases the absorbance A by a factor $k_1 = 3.3$ for C_1^{PS} and a factor $k_2 = 7.2$ for C_2^{PS}. The horizontal line in the Fig. 2.3a corresponds to three times the noise level. Its intersection with the absorbance of the solution gives the calculated LOD, which scales linearly with the invers of k. Defining LOD_{PS} as the limit of detection in the solution with dispersed PS beads and LOD as the limit of detection without them, I obtained:

$$LOD_{PS} = LOD/k. \tag{2.6}$$

Therefore, MEAS significantly improves the LOD for phenol red from 200 nM to 28 nM. The amplification factor k does not depend on the phenol red concentration C and, according to Eq. (2.4), the OPL scales linearly with k:

$$OPL_{PS} = k \cdot OPL, \tag{2.7}$$

where OPL_{PS} refers to the bead configuration and OPL to the optical path length without PS beads. While absorption spectroscopy is routinely used for colorimetric measurements, other assays use tagging strategies where the molecule of interest is attached onto various types of quantum dots, nanoparticles or fluorescent dyes that enhance the performance of such assays and serve as indicators for the presence of molecules. MEAS can also be utilized in that context and I demonstrated its utilization for the detection of gold nanoparticles or fluorescent dyes. The scattering of gold nanoparticles with sizes larger than 100 nm dominates over their absorption and such nanoparticles can be detected with high sensitivity using a dark-field configuration [123, 124]. This is not the case for nanoparticles smaller than 55 nm in diameter, for which the scattering cross section drops dramatically and the absorption cross section starts to dominate [123, 125]. However, the latter remains very weak for such small gold nanoparticles, which makes their detection quite challenging so that only a few complicated techniques have been successfully demonstrated so far [126-128]. This is detrimental for novel nanodevices that rely on extremely small metallic nanoparticles [129, 130]. Similarly, fluorescent dyes are the basis for a large number of assays commonly used in biology and chemistry and the ability to measure their absorption can provide additional quantitative information [131].

Applying the same experimental scheme, I measured the transmission for 10 nm gold nanoparticles and envy green fluorescent dyes dissolved in water or in water/PS beads ($d = 0.5\ \mu m$) dispersion with a bead concentration of $C^{PS} = 0.6$ nM. The corresponding absorbences A are shown in Fig. 2.3b and 2.3c. The 10 nm gold nanoparticles have an absorption peak at $\lambda = 520$ nm, while the envy green fluorescence dye absorbs at $\lambda = 530$ nm. Note that it is quite exceptional to be able to measure the signal of nanoparticles as small as 10 nm. As for the phenol red, the absorbance A is proportional to the concentration C of the solution. When the scattering medium is used, an enhancement factor of $k=3.3$ is observed for both the nanoparticles and the dye, while

the LOD decreases correspondingly. These results suggest that the enhancement factor k does not depend on the type of analyte, but only changes with C^{PS}, as will be investi-investigated in following.
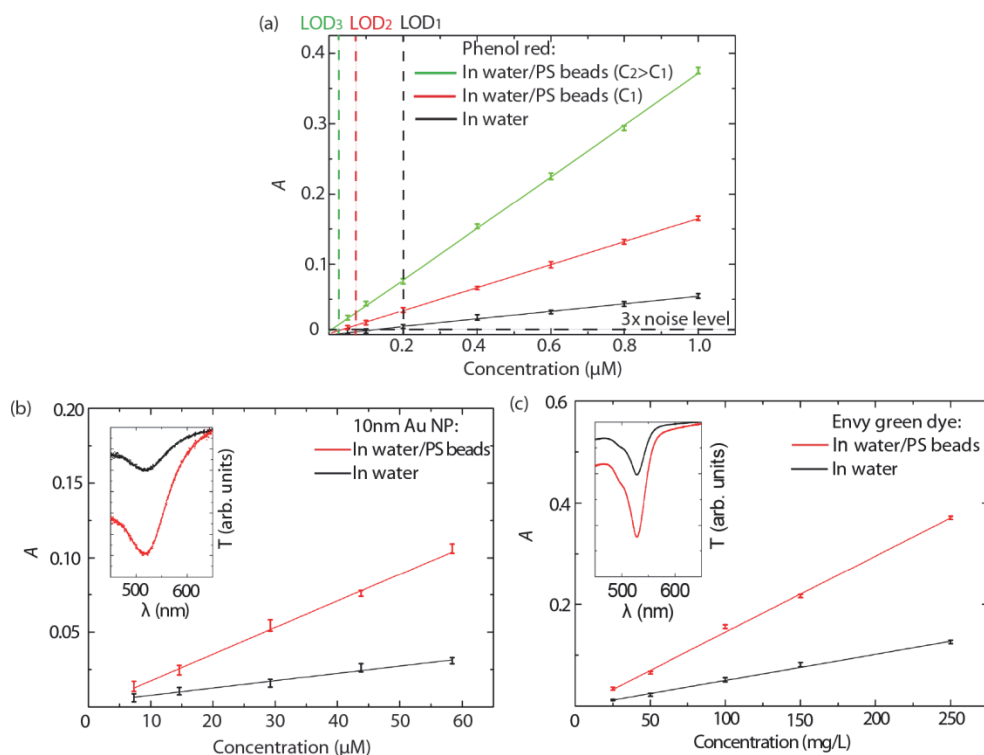
Figure 2.3. **Absorption enhancement for different analytes.** (a) Phenol red absorbance A in water only and in water with two different PS beads (0.5 µm) concentrations ($C_1^{PS} = 0.6$ nM and $C_2^{PS} = 3.0$ nM); 3 times the noise level determines the LOD at $\lambda = 570$ nm. (b) Absorbance A for 10 nm Au nanoparticles in water and in water/PS beads ($d = 0.5$ µm, C_1^{PS}) at $\lambda = 520$ nm. The inset shows the normalized transmission spectrum T of the nanoparticles. (c) Same as (b) for envy green fluorescence dye at $\lambda = 530$ nm. The error bars represent the standard deviation over 5 measurements.

2.3.4   Enhancing the sensitivity of bioassays

In addition to the LOD the sensitivity S represents an important parameter for bioassays. This parameter is of special interest when the analyte evolves with time (i.e. changes its absorption α or its concentration C), for instance, during a chemical reaction or a biological process. Here, I considered the case where the intensity changes only with the concentration, thus:

$$S = \left| \frac{\partial}{\partial C} \frac{\Delta I}{I_0} \right| = \alpha l e^{-\alpha C l}. \tag{2.8}$$

From Eq. (2.8), it can be seen that in a fixed volume with given α and C the sensitivity cannot be changed in conventional absorption spectroscopy. In contrast, S can be tuned by changing the OPL in MEAS (Fig. 2.4a). For short l, S is small since the system is in the weak-absorbing regime (regime I in Fig. 2.4a) and large changes in C are needed. On the other hand, when l is very large the medium absorbs most of the light and S drops also towards low sensitivity (regime III in Fig. 2.4a). The optimal OPL l_{opt} for which the sensitivity reaches its maximum is where $\partial S / \partial l = 0$, leading to Eq. (2.9) (regime II in Fig. 2.4a):

$$l_{opt} = \frac{1}{\alpha C}. \tag{2.9}$$

For a given α and C, with the corresponding l_{opt} given by Eq. (2.9), the maximal sensitivity is $S_{opt} = e^{-1}/C$. To demonstrate this experimentally, I showed that S and LOD of a commercially available assay for the detection of hydrogen peroxide (OxiSelect) can be improved for low concentrations. As already mentioned in Chapter 1, H_2O_2 plays an important role in biological systems: it acts as the signalling molecule in a broad variety of transduction processes and is a marker for oxidative stress which is involved in ageing but also in various diseases [132, 133]. OxiSelect works on the principle of the oxidation of Fe^{2+} to Fe^{3+} in the presence of H_2O_2 which forms a ferric xylenol orange (Fe-XO) complex. The formation of Fe-OX complexes leads to an alteration of the molar absorption coefficient, providing information on the H_2O_2 concentration present in the solution.

The experiments in this work are carried out using the bioassay according to the instructions provided by the supplier, particularly the absorption is determined at $\lambda = 595$ nm. Not only the H_2O_2 concentration but also the rate of change is a very important parameter providing information about the dynamics of biological processes under study. The sensitivity for different H_2O_2 concentrations is determined by measuring the change in the signal when 1 µM of H_2O_2 is added to a known concentration. Similarly I measured the sensitivity S^{PS} in the presence of 0.6 nM of PS beads having a diameter of 0.5 µm. As observed in the previous experiments, the OPL increases by a factor of $k = 3.3$ for $L = 3.7$ mm and consequently S^{PS} is enhanced for low concentrations as shown in Fig. 2.4b. Moreover, the lower limit of the working range, given as 1 µM by the manufacturer, can be reduced to 300 nM. In the configuration at hand S^{PS} is larger than S in water for H_2O_2 concentrations lower than the threshold value $C_{th} = 30$ µM, while for higher concentrations the sensitivity S without PS beads dominates. The expressions for S_{opt} and l_{opt} suggest that very high sensitivities can be achieved for low concentrations with a corresponding large l_{opt}, Eq. (2.9). In our experiments, I showed that it is possible to improve the performance of the bioassay by the factor $S^{PS}/S = 2.5$ for 2 µM of H_2O_2. Therefore, the concentration of the PS beads can be adapted in order to obtain maximal sensitivity for the concentration range of interest.
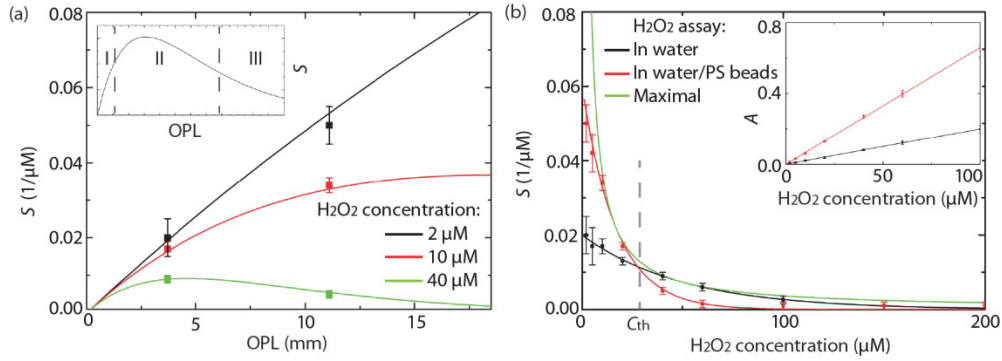
Figure 2.4. **Enhancing the sensitivity using MEAS.** (a) Sensitivity S of the H_2O_2 assay as a function of the OPL for a fixed concentration and (b) as the function of the concentration, in a $L = 3.7$ mm cuvette filled with water and with 0.6 nM PS beads dispersion ($d = 0.5$ μm, $k = 3.3$) at $\lambda = 595$ nm. Points refer to measurements and the lines are fitted according to Eq. (2.8). The OPL is calculated using Eq. (2.7). Inset in (a) shows three distinct regions: I – growing sensitivity, II – maximal sensitivity and III – decreasing sensitivity. Inset in (b) shows the absorbance A in water and in water/PS beads dispersion ($d = 0.5$ μm) ($C^{PS} = 0.6$ nM, $L = 3.7$ mm, $k = 3.3$). The error bars represent the standard deviation over 5 measurements.

2.3.5 Enhancing the sensitivity of colorimetric detection with gold nanoparticle probes

For a further demonstration of the performance of MEAS, I study the aggregation of 10 nm gold nanoparticles in the presence of hexanedithiol. Dispersed gold nanoparticles can be used as basis for sensitive colorimetric probes [134]. In this experiment, the two free thiol groups of hexanedithiol can bind two or more gold nanoparticles together. This leads to a gradual aggregation of the nanoparticles, which can be monitored via the optical response. As shown earlier, 10 nm gold nanoparticles exhibit an absorption peak at $\lambda = 520$ nm, which decreases with progressive aggregation of the nanoparticles (Fig. 2.5). At the same time, a broad peak corresponding to the aggregated particles emerges at higher wavelength. Thus, A can be directly related to the amount of hexanedithiol in the solution. Applying the described experimental scheme to Au nanoparticles suspended in water, A decreases from 0.05 to 0.02 upon addition of hexanedithiol. In contrast, in water/PS beads dispersion with a bead concentration of $C^{PS} = 0.6$ nM A changes from 0.16 to 0.07, indicating an enhancement of $k = 3.3$. To be complete, it is worth mentioning that hexanedithiol does not bind to the PS beads surface. In conclusion, I demonstrated an enhanced sensitivity to hexanedithiol using 10 nm gold nanoparticles as colorimetric probes in MEAS, compared to conventional absorption spectroscopy.
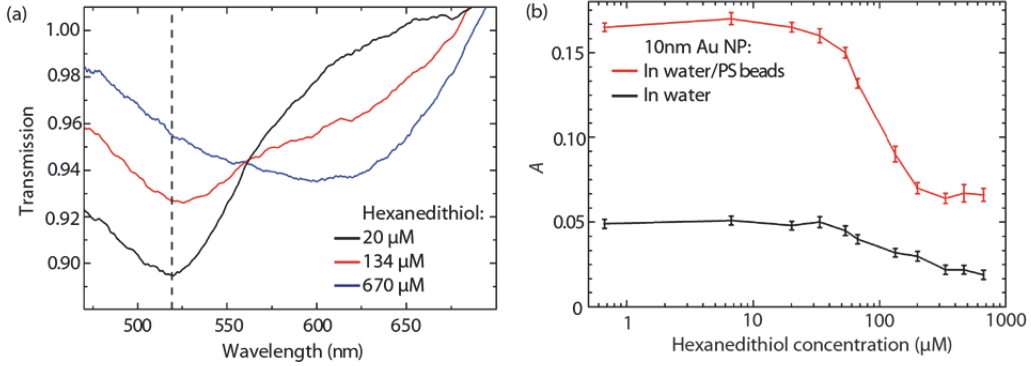
Figure 2.5. **Enhancing the sensitivity of gold nanoprobes.** (a) Normalized transmission spectra for 20 μM (black), 134 μM (red) and 670 μM (dark blue) hexanedithiol with 10 nm gold nanoparticles (80 μM). The dashed line indicates the wavelenegth (λ = 520 nm) at which A was calculated. (b) Absorbance A of 10 nm gold nanoparticles (80 μM) with respect to different concentrations of hexanedithiol in water and in water/PS beads dispersion (d = 0.5 μm, C^{PS} = 0.6 nM, L = 3.7 mm, k = 3.3). The error bars represent the standard deviation over 5 measurements.

2.3.6   Control of the path length enhancement

Let us now discuss the parameters that influence the OPL in a random medium. The enhancement of the OPL is determined by the number of times the wavepackets are scattered while travelling through the disordered medium. For a multiscattering medium the OPL in transmission scales with the reciprocal of the mean free path l^* in the dispersion [135]:

$$OPL \sim \frac{1}{l^*}. \tag{2.10}$$

I only considered non-opaque samples since low absorption measurements are of special interest for absorption spectroscopy.

As seen from the experiments with phenol red (Fig. 2.3a), the PS beads concentration, and thus the filling factor F, affects the OPL enhancement [82]. If C^{PS} is low, l^* becomes larger than L, hence, k goes to unity and the system is no longer in the multiscattering regime. Figure 2.6a displays both the measured and simulated k as a function of F for phenol red. The graph indicates that k can be increased up to 15 for F = 0.1. The value of F has an upper limit, which is determined by the close-packed configuration i.e. F cannot go beyond 0.5-0.7 depending on the type of packing [136]. Note in Fig. 2.6a the excellent agreement between simulations and measurements.

The numerical analysis of MEAS relies on a homogeneous statistical distribution of the scatterers within the sample volume. Hence, aggregation of the scatterers can reduce

the OPL enhancement. Such an aggregation is more likely for a high PS beads concen-concentration. Aggregation can be caused by the background media, which could reduce the OPL enhancement and hence the sensitivity. More detrimental is the case where aggregation is caused by the analyte itself, since in that case the base line measurement corresponds to a non-aggregated system. However, in our experiments I targeted very low concentrations of analytes, which limits aggregation. It goes without saying that the scattering medium should not interfere chemically with the species under study; this is the case for the PS beads used in the different experiments reported here.
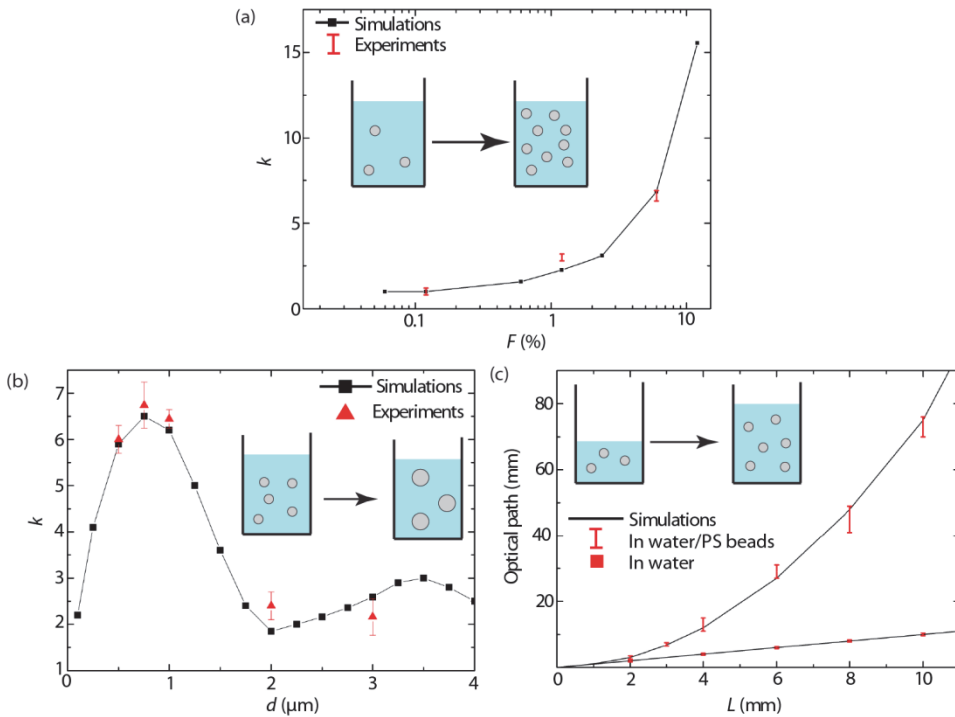
Figure 2.6. **Tuning optical path length (OPL).** (a) Optical path length (OPL) enhancement as a function of PS beads filling factor F for a 40 µl mixture, when changing the PS beads ($d = 0.5$ µm) concentration. (b) OPL enhancement for PS beads with different sizes for a 40 µl mixture, keeping the filling factor F equal to 0.052. (c) Optical path for phenol red in water and in water/PS beads dispersion ($d = 0.5$ µm) (calculated using Eq. (2.7)) as a function of the measurement cell thickness L. The PS beads concentration is kept constant C^{PS} =0.6 nM. Error bars represent the standard deviation for 5 samples.

To investigate the influence of the PS beads size I prepared bead dispersions with dif-different concentrations C^{PS} and different diameters d while keeping the filling factor F constant; the following PS beads diameter/concentrations are used: 0.5 μm / 3.0 nM, 0.75 μm / 0.9 nM, 1 μm / 0.375 nM, 2 μm / 38 pM and 3 μm / 14 pM. Since 2 and 3 μm beads sediment in water within a few minutes, the solution density must be increased by addition of 0.05 g/ml of glucose leading to a final density of 1.02 g/ml, which efficiently hinders sedimentation (PS density ρ = 1.05 g/ml, glucose ρ = 1.6 g/cm³). This addition of glucose does not affect the refractive index of the solution significantly, which changes from 1.33 to 1.34. In this case Eqs. (2.3) and (2.10) lead to $OPL \sim Q_{sca}(1 - g)/d$. I compare k for a 40 μl solution with 1 μM phenol red solution (Fig. 2.6b). A maximum of the k value can be observed for PS beads with a diameter $d = 0.75$ μm. Simple calculations using Mie theory show that Q_{sca} strongly varies with d while the change in the value of g is insignificant. Furthermore, the two maxima of the k values around $d = 0.75$ and 3.5 μm agree well with maxima in Q_{sca} obtained from Mie theory. It is worth mentioning that Q_{sca} can also be tailored by tuning the refractive index contrast Δn between the surrounding medium and the particle [137].

It is known that for disordered media the OPL increases with L^2 since the number of scattering events increases with L [83]. Consequently, according to Eq. (2.7), the enhancement factor k increases with L and therefore MEAS, compared to absorption spectroscopy, benefits even more from increasing L. In order to vary the geometrical thickness L, I prepared a solution of 1 μM phenol red with 0.6 nM PS beads ($d = 0.5$ μm) and fill different volumes of the mixture in a 96-well plate (the larger cross section area available in such a well ensures no cross talk between neighboring wells). Transmission measurements confirm that the OPL of phenol red in water increases linearly with L (Fig. 2.6c), whereas in water/PS bead dispersion it grows quadratically with L. For conventional absorption spectroscopy L changes from 4 to 10 mm, whereas for MEAS an OPL increase from 13.2 to 73 mm was observed as shown in Fig. 2.6c, corresponding to a change in absorption enhancement k from 3.3 to 7.3.

2.3.7 Spectral dependence of the path length enhancement

Till now, I determined k only for a single wavelength. As follows from Eqs. (2.3) and (2.10), k changes with the wavelength due to the dispersive nature of Q_{sca} [137]. As indicated in the Appendix B, for the experiments on phenol red, gold nanoparticles and envy green reported here, k changes only by 2% in the wavelength range of 450–650 nm ($d = 0.5$ μm, $F = 0.0104$, $L = 4$ mm), with the largest value of k obtained for the smallest wavelength, in good agreement with Mie scattering [137]. The optical dispersion increases further with the cell thickness L, the F factor and the PS beads diameter d.

2.4   Maximal absorption regime in random media

Collecting light transmitted through random media gives access to photons with long optical paths. However, in this configuration most of the light is lost. In the present section, I aim to find conditions of maximal absorption of light in the presence of

random medium. This regime would correspond to the optimal coupling between light and the absorber. Additionally, if one finds the way to collect all non-absorbed light, then maximal absorption would also lead to the best sensing. With this in mind, I studied three-dimensional random medium with varying filling factors – ranging from a homogenous medium to a diffusion-like and, finally, to a close-packed random medium – in an absorbing background using numerical simulations. To this end, vast number of theoretical works that studied reflection and transmission of light in random media with absorption or gain has to be acknowledged [138-150]. This work is distinct because the effects of geometrical parameters as well as scattering properties on the absorbed energy are examined. Additionally, embedding the random medium into an open cavity increases the absorbed energy further, providing 23-fold enhancement compared to the random medium without cavity. As a potential application, I theoretically demonstrate that random medium improves the absorption of light in the existing light trapping system. In this section, I use an absorption coefficient $\alpha = 30 \text{ m}^{-1}$ and the incident free-space wavelength is $\lambda = 550 \text{ nm}$.

2.4.1   Identifying maximal absorption

As the filling factor F of the random medium is increased, OPL_T increases from being equal to the thickness of the medium L (horizontal dashed line in Fig. 2.7a) to much larger values corresponding to the multiscattering regime. However, for $F > 1\%$ only small part of energy is transmitted in the forward direction as indicated by blue line in the inset of Fig. 2.7b. Concurrently, OPL_R rises slightly at first due to the multiscattering, but decreases for $F > 1\%$ because the sample reflectivity increases. The nature of light propagation evolves from ballistic to highly scattering: according to Eq. (2.1), the mean free path l_{free} changes from several meters (for $F < 10^{-4}\%$) to only a few micrometers ($F > 10\%$).

In such a system, the absorbed energy E_{abs} exhibits a non-monotonic dependence that peaks at $F_{cri} = 1.3\%$ corresponding to $l_{free} = 7\,\mu\text{m}$ (Fig. 2.7b). This behaviour is associated with different regimes of light propagation: weak (I), moderate (II) and strong (III) (Fig. 2.7c). In the weak scattering regime ($F \ll 1\%$), most of the energy is transmitted in the forward direction along the path of incident light and, thus, E_{abs} grows with OPL_T. In the moderate or so-called diffusion regime, all photons lose their initial direction after having travelled about $100\,\mu\text{m}$ in the medium and spread over the entire absorber volume. In the strongly scattering regime ($F > 5\%$), the energy is mostly backreflected, so that negligible amount of light reaches the distant parts of the absorber (black regions in the colormap). In this case, E_{abs} follows the same trend as OPL_R, decreasing with increasing F. Therefore, maximal absorption occurs when the number of scatterers is high enough that the incident light experiences multiscattering, but low enough that the light is not strongly confined close to the incident interface and benefits from the full absorber volume. Finally, let us emphasize the difference between maximal absorption and maximal OPL_T, which is commonly used in sensing [83]. The latter is characterized by low transmission, high values of OPL_T and hence benefits from high F values in contrast to maximal absorption.
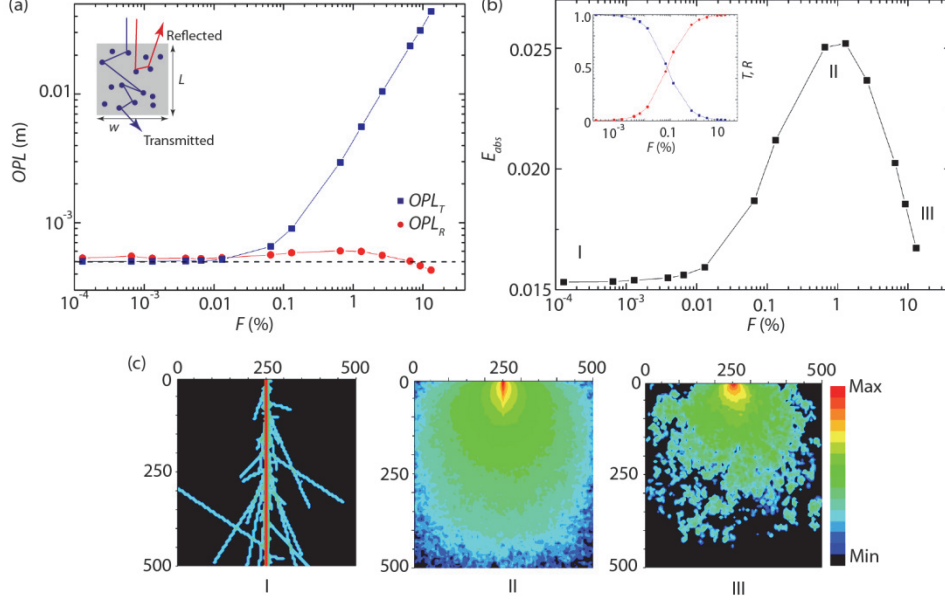
Figure 2.7. **Absorption in a random medium**. (a) Optical path lengths OPL_T and OPL_R in a cubic random medium $(L \times w \times w)$ with $L = 500\ \mu\text{m}$ and $w = 500\ \mu\text{m}$ formed by spherical scatterers $(d = 0.5\ \mu\text{m},\ n = 2.6)$. The dashed horizontal line corresponds to L. The inset shows the geometry under study. (b) Absorbed energy E_{abs} in the random medium. The inset shows the normalized transmitted T (dark blue) and reflected R (red) intensity of light. (c) Logarithmic energy distribution of the light propagating in the central plane of the random medium described in (a) corresponding to (I) $F = 10^{-4}$ %, (II) $F = 1$ %, and (III) $F = 10$ %. The color scale is common to all three colormaps. The dimensions are given in micrometers.

2.4.2 Effect of geometrical and scattering properties on the absorption

The absorbed energy is determined by the geometrical size and the optical properties of the random medium. To study the first effect, consider in Fig. 2.8a random media with various width w, while keeping L constant at $500\ \mu\text{m}$. For $F < 10^{-3}$ %, E_{abs} does not depend on w because light propagates mostly without scattering events (Fig. 2.8a). Defining E_0 as the absorbed energy in the absence of scatterers, I observed that the presence of a random medium increases E_{abs} as compared to E_0 for $w = 500\ \mu\text{m}$ and $750\ \mu\text{m}$, Fig. 2.8a. At the same time, for $w = 250\ \mu\text{m}$ and $100\ \mu\text{m}$, E_{abs} first decreases with increasing F and then reaches a local maximum. This is because for such small lateral dimensions, photons that undergo scattering events predominantly exit the system from the sides, resulting in a lower OPL as compared to photons that propagate along the incident direction in the absence of random medium. With further increase of F, the emergence of multiscattering improves OPL and E_{abs} reaches its local maximum.

21

However, for $F > 10$ %, E_{abs} decreases in all cases because of the strong reflection. If w increases above 500 μm, the peak value of E_{abs} (which I call E_{max}) grows until it satu-saturates for $w > 1000$ μm, implying that for very wide samples E_{abs} is limited not by the lateral confinement, but by the photons escaping through the top and bottom surfaces (Fig. 2.8c). Therefore, for those parameters, the presence of a random medium improves E_{abs} as compared to E_0, only if $w \geq 0.8\,L$.
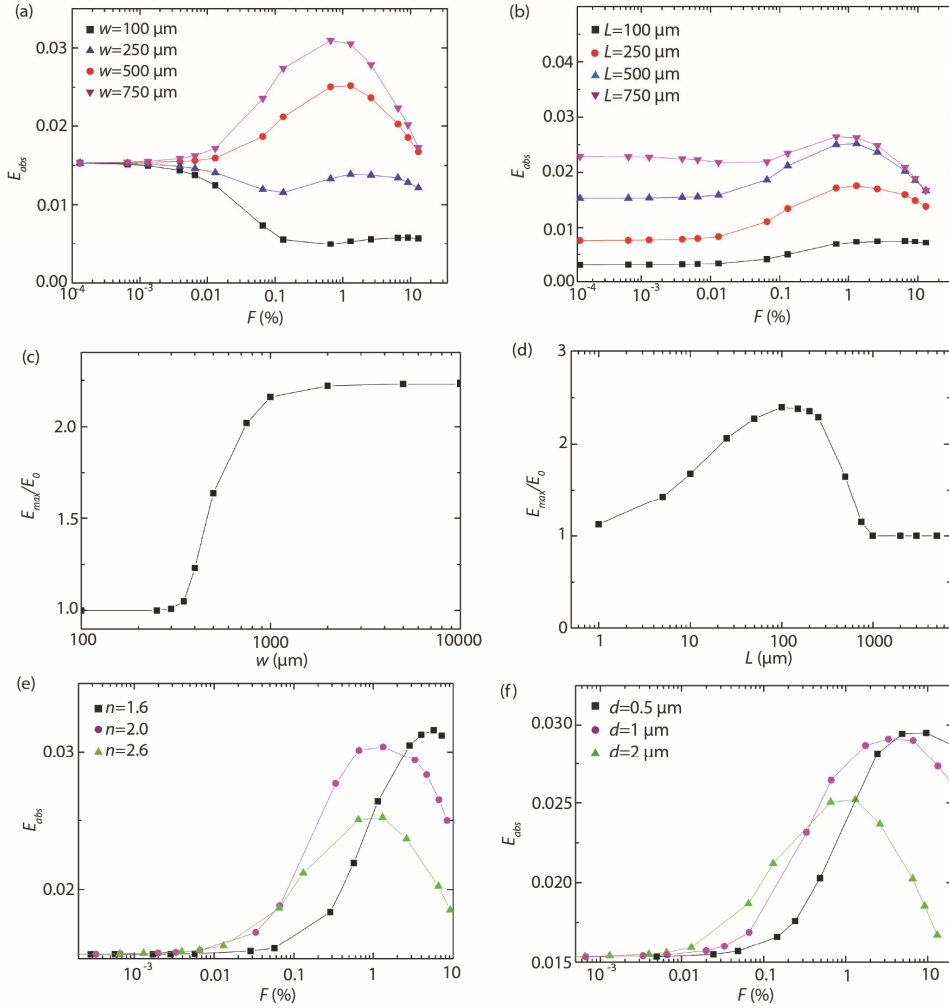
Figure 2.8. **Effect of geometrical and scattering properties in free random medium.** Absorbed energy E_{abs} for a square prism with dimensions $L \times w \times w$ filled with a random medium when varying: (a) the width w ($L = 500$ μm, $d = 0.5$ μm, $n = 2.6$); (b) the length L ($w = 500$ μm, $d = 0.5$ μm, $n = 2.6$); (c) the dependence on w of the maximum absorbed energy enhancement E_{max}/E_0; (d) E_{max}/E_0 as a function of L; (e) the refractive index n ($L = w = 500$ μm, $d = 0.5$ μm); and (f) the scatterers diameter d ($L = w = 500$ μm, $n = 2.6$).

Next, I varied L while keeping a constant width $w = 500\,\mu m$. Figure 2.8b shows that for $L = 100\,\mu m$, $250\,\mu m$ and $500\,\mu m$ ($w \geq L$) E_{abs} follows a bell-shaped curve. However, I ob-observed a local minimum for $L = 750\,\mu m$ at $F = 0.1\,\%$, which resembles the E_{abs} behaviour for $w < 250\,\mu m$ observed previously. For $L > 1000\,\mu m$ or $w \leq 0.8L$, the enhancement due the presence of a random medium E_{max}/E_0 tends toward unity (with F_{cri} going to zero), demonstrating that increasing L is not beneficial without simultaneously increasing w (Fig. 2.8d). If $L < 10\,\mu m$ the sample consists only of a few layers of scatterers and does not support multiscattering, therefore E_{max}/E_0 again goes to unity. I did not observe a similar behaviour for large w and $L = 500\,\mu m$ since in that case the medium was always in the multiscattering regime. The presence of a random medium brings maximum improvement (E_{max}/E_0 reaches its maximum value of 2.4) for a distance of $L \sim 200\,\mu m$, which corresponds to $w \sim 2.5L$.

Table 2.1. Properties of scatterers of different refractive index n ($d = 0.5\,\mu m$).

n	g	Q_{sca}	C_{cri} (part./ml)	F_{cri} (%)	l_{free} (µm) at F_{cri}	l^* (µm)	E_{max}
1.6	0.76	0.78	$8.59 \cdot 10^{11}$	5.62	7.61	31.68	0.0316
2.0	0.72	3.63	$1.84 \cdot 10^{11}$	1.20	7.63	27.33	0.0306
2.6	0.45	3.62	$1.85 \cdot 10^{11}$	1.21	7.61	13.84	0.0252

Table 2.2. Properties of scatterers of different diameter d ($n = 2.6$).

d (µm)	g	Q_{sca}	C_{cri} (part./ml)	F_{cri} (%)	l_{free} (µm) at F_{cri}	l^* (µm)	E_{max}
0.5	0.45	3.62	$1.85 \cdot 10^{11}$	1.21	7.61	13.84	0.0252
1	0.65	3.31	$5.04 \cdot 10^{10}$	2.64	7.62	21.80	0.0291
2	0.68	2.62	$1.59 \cdot 10^{10}$	6.66	7.64	23.88	0.0299

Let us now study the effect of the scatterer refractive index n and size d while the other parameters are kept fixed. Figures 2.8e, respectively 2.8f, depict E_{abs} as a function of F for selected values of n, respectively d. These parameters affect the values of Q_{sca} and g for individual scatterers as shown in Tables 2.1 and 2.2. While all E_{abs} curves have similar shapes, the values for F_{cri} and E_{max} differ. Furthermore, notice how media with spheres that have similar g ($n = 1.6$ and 2.0) or Q_{sca} ($n = 2.0$ and 2.6) still have different F_{cri}. In Table 2.2, I observe that the main parameter determining light confinement in the random medium l_{free} shows almost identical values at F_{cri} for the different diameters d. Hence the maximal absorption regime is linked to certain l_{free} for a given geometrical configuration. For example, it is clear from Eq. (2.3) that increasing d while keeping C^{PS} constant would decrease l_{free}. That is, to achieve the same value of l_{free} for increasing values of d, we have to decrease C^{PS}. This is why C_{cri} decreases on increasing

d as seen in Table 2.2. The behaviour observed here is similar to random lasers for which l_{free} determines their quality factor [69]. Finally, as evident from Fig.2.8a and 2.8b, the value of F_{cri} also depends on the geometry of the random medium.

Although l_{free} defines the position of maximal energy, E_{max} values are different. From Tables 2.1 and 2.2, notice a correlation between the mean free path l^* and E_{max}. In the diffusive regime, all OPLs and, in turn, E_{abs}, scale with l^* [151]. This is the reason why l^* determines E_{max}.

2.4.3 Random medium in an open cavity

To increase the absorbed energy in the random medium, I embedded it into an open fully reflective cavity, which contains two square openings with dimensions $s \times s$: one at the center of the top and one at the bottom face for the reflected and transmitted light (see the inset in Fig. 2.9c). I choose such a configuration to compare the performances of the random medium in an open cavity (henceforth referred to as the open cavity) to that of the random medium without reflective walls with exactly the same geometry (henceforth referred to as the free random medium). Additionally, I calculated different enhancement factors k to quantify the enhancement provided by the open cavity.

The open cavity configuration leads to an increase in the effective volume which, in turn, enhances OPLs. For instance, OPL_R increases by a factor $k_R = 32$ for low F compared to the free random medium (Fig. 2.9a, b). The OPL_T enhancement, k_T reaches a maximum of 27 at the critical filling factor $F_{cri} = 0.07 \%$ and then drops along with OPL_R. This is because for $F > 1 \%$ most of the light is confined in a volume smaller than the size of the cavity; hence very little is reflected from the walls leading to the decrease of the enhancement factors k to unity, Fig. 2.9b. The energy absorption E_{abs} peaks at $F_{cri} = 0.13 \%$, with an enhancement $k_E = 23$ for the absorbed energy compared to the free random medium (Fig. 2.9c, d). The fact that the maximum energy absorption occurs at different filling factors for the free random medium and for the open cavity is caused by the different effective volumes for these two geometries. To visualize the absorption in the cavity, in Fig. 2.9e I plot the light intensity in the central plane of the cavity with the same colour scale as in Fig. 2.7c. The second diagram illustrates the maximum of the absorbed energy, whereas the third diagram shows strong backreflections corresponding to high values of F.

Let us now study the influence on light absorption of various parameters describing the random medium in the open cavity. Similar to the free random medium, the filling factor F_{cri} producing the largest absorption shifts when the refractive index n of the scatterers changes; for the three different indices investigated in Fig. 2.10a, I observed that l_{free} at F_{cri} is close to 56 μm, which is about eight times larger than in the case of the free random medium. Furthermore, in contrast to the free random medium, now the E_{max} values remain similar for the different refractive indices. This is caused by the reflective walls which now play the major role, rather than l^*, for confining the light, as is evident from the 23-fold enhancement observed for E_{abs} in Fig. 2.9d. The probability

of light escaping from the open cavity is given by the ratio of the openings area to the total cavity area. This is demonstrated by changing w while keeping s fixed: E_{abs} chang-changes, but retains a bell-shaped profile for all w, in contrast to the free random medium (compare Fig. 2.10b and 2.8a). Similarly, the light confinement changes with s, leading to different E_{abs} (Fig. 2.10c). By reducing s to 5 μm, absorption of 99% can be achieved simply due to the high confinement of the cavity.
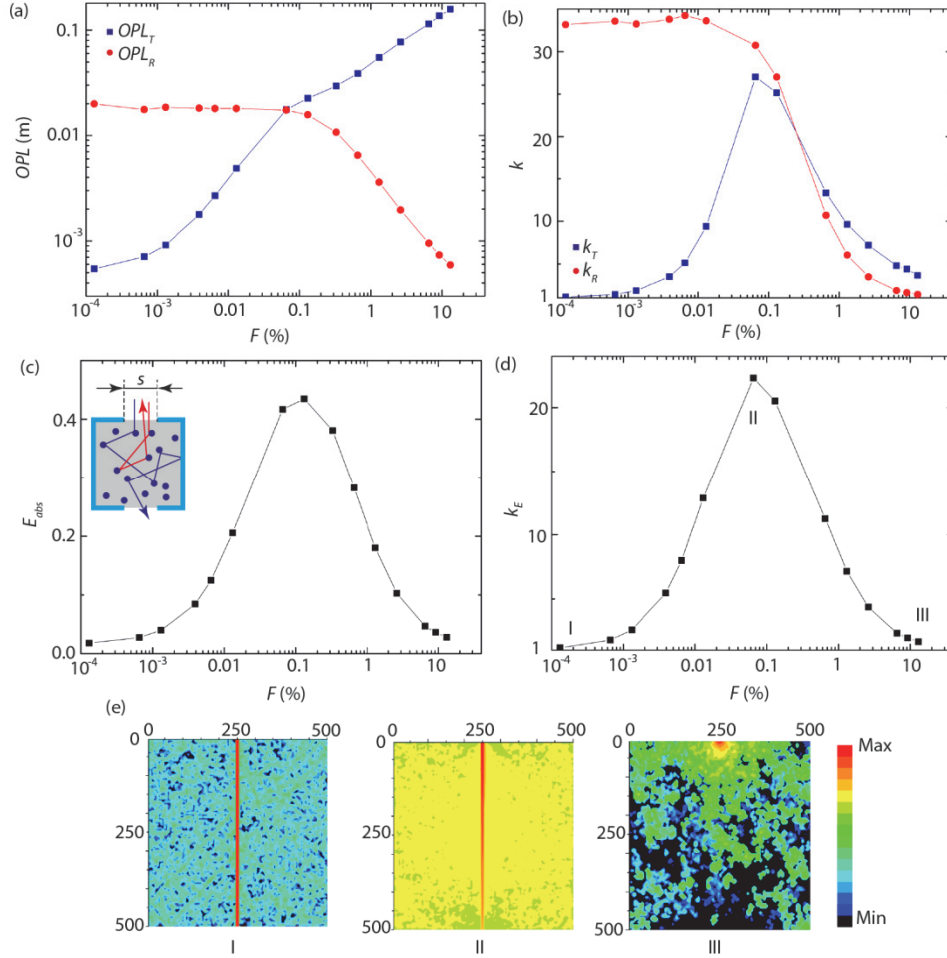
Figure 2.9. **Random medium in an open cavity.** Absorption in a random medium ($d = 0.5$ μm, $n = 2.6$) surrounded by a fully reflective cavity ($L = w = 500$ μm) containing two square openings with size $s = 100$ μm. (a) OPL_T and OPL_R. (b) OPL enhancements compared to the free random medium k_T and k_R. (c) E_{abs} in the medium; the inset shows a schematic of the geometry. (d) Enhancement of the absorbed energy compared to the free random medium k_E. (e) Logarithmic intensity distribution of light propagating in the central plane corresponding to (I) $F = 10^{-4}$ %, (II) $F = 0.05$ %, (III) $F = 10$ %. The color scale is common for all three colormaps. The dimensions are given in micrometers.

25
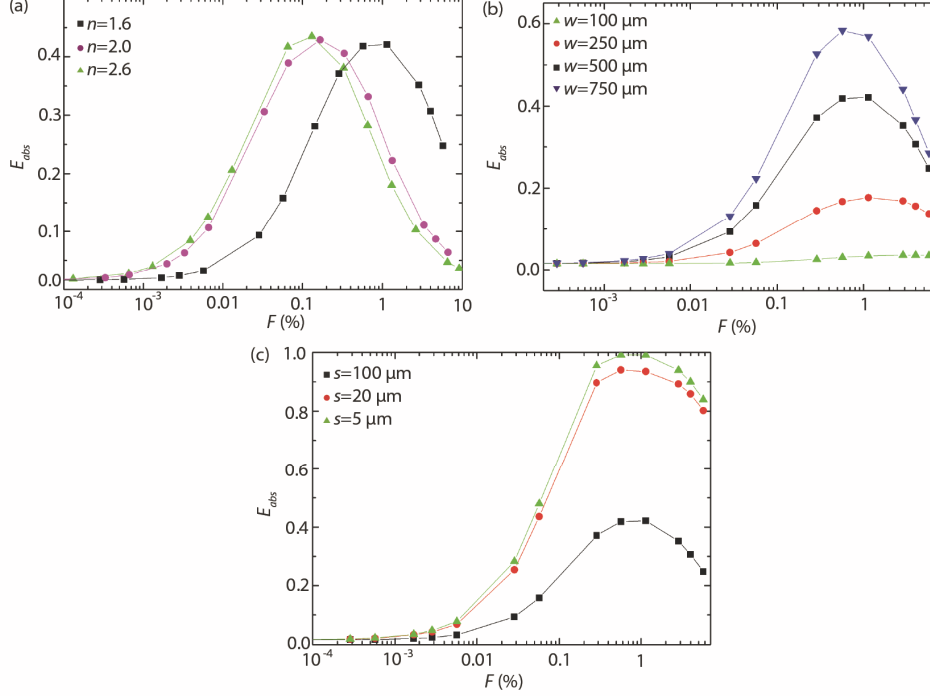
Figure 2.10. **Effect of geometrical and scattering properties in an open cavity.** Absorbed energy E_{abs} for a random medium ($d = 0.5\,\mu m$) surrounded by a fully reflective cavity ($L = 500\,\mu m$) containing two square openings with size s (see Fig. 2.9c inset) as a function of: (a) the refractive index n of the scatterers ($s = 100\,\mu m$, $w = 500\,\mu m$), (b) the cavity width w ($s = 100\,\mu m$, $n = 1.6$) and (c) the openings size s ($w = 500\,\mu m$, $n = 1.6$).

2.4.4　From weak to strong absorbers

Different light trajectories have different OPLs in the random medium. With the presence of the absorber, the energy transmitted through the system for a given trajectory is modified according to Beer-Lambert's law [119]. The trajectories with longer OPL undergo stronger absorption. As a result, the nature of light propagation also depends on the value of the absorption α: while for weak absorbers it is diffusion-like, it becomes dominantly ballistic for strong absorbers, reducing multiscattering effects [152]. In the latter case, Fig. 2.11 shows that E_{max}/E_0 decreases to unity for $\alpha > 10^4\,\mathrm{m}^{-1}$, meaning that the benefits of multiscattering are then lost.

To characterize the effect of absorption in the medium, I introduced the absorption mean free path l_{abs} that can be related to l^* and to the inelastic mean free path l_i, which is defined as the travelled length over which the light intensity is reduced by a factor $1/e$

due to absorption ($l_i = 1/\alpha$); l_{abs} is then defined as the average distance between begin and end points for paths of length l_i [70]:

$$l_{abs} = \sqrt{\frac{1}{3} l^* l_i} = \sqrt{\frac{l^*}{3\alpha}}.$$ (2.11)

The parameter l_{abs} reflects the nature of light propagation in random media with gain or losses [69]. As the absorption α in the background is increased, F_{cri} decreases, as can be seen in the Fig. 2.11c. This shift is less pronounced for the open cavity since the light confinement in that geometry is dominated by the reflective walls (for $F < 10\,\%$) and, thus, weakly depends on l_{abs} (Fig. 2.11b and d).
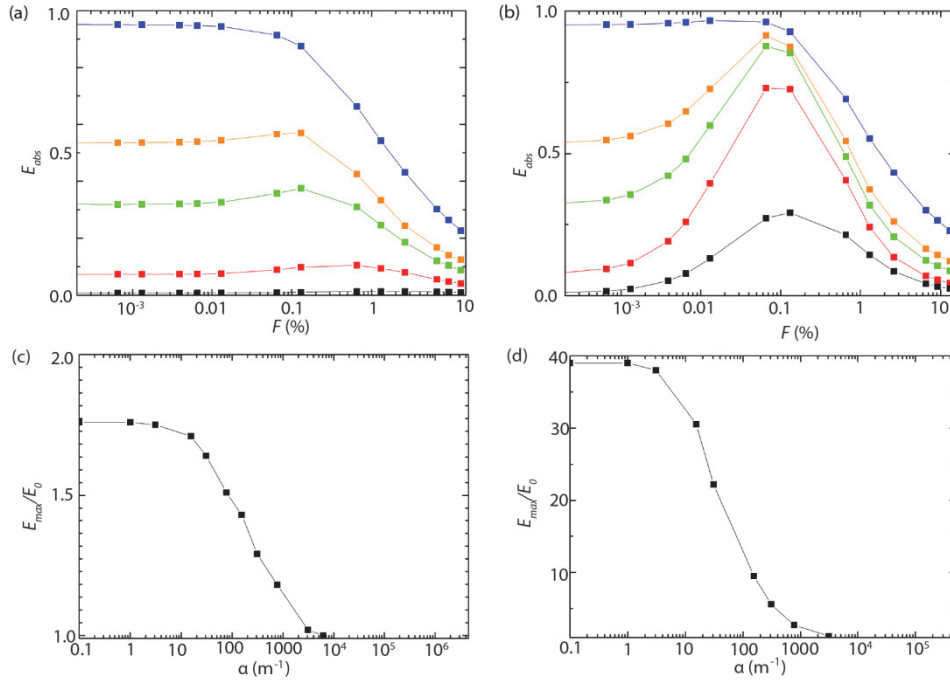
Figure 2.11. **Effect of α on multiscattering.** Absorbed energy E_{abs} on the absorption coefficient α for: (a) free random medium ($L = 500$ μm, $w = 500$ μm, $d = 0.5$ μm, $n = 2.6$); (b) open cavity with same parameters as in (a) and $s = 100$ μm. $\alpha = 30$ m^{-1} (black), 150 m^{-1} (red), 750 m^{-1} (green), 1500 m^{-1} (orange) and 6000 m^{-1} (dark blue). (c,d) Dependence of E_{max}/E_0 for the respective geometries as in (a) and (b).

2.4.5   Light trapping scheme to improve the absorption of light

Photovoltaics or light transformation into electric current is a renewable and pollution-free source of energy. Recent trends suggest moving towards thin film solar cells, where recombination losses of generated hole-electron pairs would be minimized [153]. However, such a trend also requires efficient light trapping methods to maximize the absorption of solar cells [154]. Existing light trapping schemes utilize geometric engineering [155-159], plasmonic nanoparticles [160-162], metallic and dielectric gratings [163, 164], resonant dielectric nanoparticles [165, 166] and photonic crystals [167-169]. Geometric engineering schemes and gratings can suffer from defects and often require alignment or a tracking system, whereas nanoparticles and photonic crystals are resonant and do not necessarily cover the full solar spectrum [167]. In this context, random structures offer broadband and wide-angle performance, which is crucial in solar energy harvesting [79].

To date, random structures for light trapping applications include randomly textured patterns on front or back sides of solar cells [79, 170-172]. Interestingly, these works mainly focus on two dimensional structures. From the other perspective, their performance is evaluated only in terms of structural correlations: authors seek the optimal conditions, in which the light can be efficiently coupled to the Anderson closed loops that provide high absorption. However, recently it was shown that the so-called diffusive regime with moderate filling factors is also beneficial for the absorption because of the formation of eigenchannels with long optical paths [152].

To illustrate an application of maximal absorption, consider the optimization of the light trapping system shown in Fig. 2.12a. Using such device for thin solar cells, Tvingstedt *et al.* demonstrated a 25% increase in the absorption of the solar cell and photocurrent [155]. The proposed geometry includes highly reflective mirrors with light trapped in the space between them. The absorption happens only in the thin layer (50 nm) of active material with the absorption coefficient $\alpha = 10^5 \, \mathrm{m}^{-1}$, while all the remaining material is non-absorbing. A concentrator focuses all the light reaching its surface into the opening in the top mirror. Here, an array of glass lenses with focal distance $f = 1 \, \mathrm{mm}$ acts as concentrator [155]. The choice of lens material and the quality of fabrication constrain the value of f for a given w [173]. The cone of light entering the solar cell covers a range of incident angles between $\beta = 0$ and $\beta = 14°$ for $w = 500 \, \mu\mathrm{m}$. Such a low β does not allow the solar cell to efficiently trap light inside, since the incident light is just reflected back by the structure. To overcome this limitation, I introduced a random medium in the space between the top mirror and the active layer. To simulate the light behaviour in this device, a truncated unit cell with reflective side walls is considered (Fig. 2.12b).
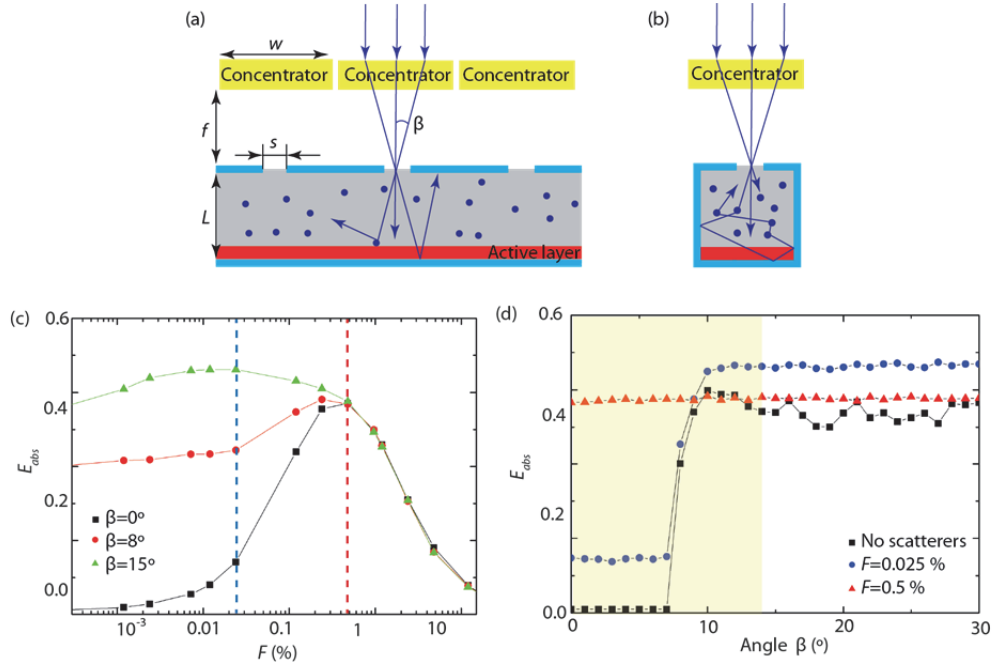
Figure 2.12. **Light trapping device.** (a) Schematic of light trapping device with two reflective surfaces, active photovoltaic layer (in red) and an array of concentrators on top. (b) Schematic of the truncated unit cell used in the numerical simulations. (c) E_{abs} as a function of F for light entering the opening at different angles in the presence of a random medium ($d = 0.5\,\mu m$, $n = 2.6$, $L = 100\,\mu m$, $w = 500\,\mu m$, $s = 50\,\mu m$). The blue dashed line corresponds to $F = 0.025\,\%$ and the red one to $F = 0.5\,\%$. (d) E_{abs} as a function of β; the yellow area corresponds to $β = 0 – 14°$, the angular range of light after it has passed through a concentrator with $f = 1$ mm.

Quite strikingly, an appropriate concentration of scatterers confines light inside the structure – even for low illumination angles β – and enhances absorption inside the active layer (Fig. 2.12c). For instance, even for $β = 0°$ (corresponding to light incident normally on the structure), the E_{max}/E_0 ratio reaches 55. Whereas for light incident at $β = 0°$ and 8°, E_{abs} peaks at $F = 0.5\,\%$ showing similar values of E_{max} in both cases; for $β = 15°$, E_{abs} dependence is much broader with a peak at $F = 0.025\,\%$. The latter effect is due to the different effective geometry that light experiences at a given angle as compared to $β = 0°$ case. To summarize the angular performance of the light trapping scheme in the presence of a random media, I show in Fig. 2.12d the absorbed energy E_{abs} for different angles. For $β < 8°$, the incident light is reflected from the bottom mirror and exits through the same opening as entered, not being absorbed significantly, while for higher β light is efficiently confined inside the cell. This is why there is a jump in E_{abs} at $β = 8°$ in the absence of scatterers. On the other hand, for $F = 0.5\,\%$ E_{abs} shows a weak dependence on β since light experiences strong multiscattering. Therefore, light

absorption significantly improves in the presence of random medium for angles $\beta < 8°$. Considering the total angular range of $\beta = 0 - 14°$, I observe a 2.2 enhancement of E_{abs} for $F = 0.5\%$ and 1.4 for $F = 0.025\%$ as compared to the case without scatterers. Fur-Furthermore, the proposed multiscattering phenomenon is non-resonant and hence broadband, which is important when working with solar energy. Although light trapping is more efficient with smaller s, larger values of s provide robustness and tolerance for the alignment of the solar concentrator with respect to the incident light [156], e.g. for the solar concentrator in Fig. 2.12 this tolerance is only 2.9°.

2.5   Summary

In this chapter, I have presented a new scheme for sensitive absorption measurements, particularly well-suited for low analytes concentrations. The technique is based on multiscattering-enhanced absorption spectroscopy (MEAS). Like conventional absorption spectroscopy, MEAS is fast, simple and inexpensive. By introducing PS beads into a solution containing the analyte, light undergoes multiscattering, which increases the optical path length through the sample. This way, a higher sensitivity and lower LOD, compared to conventional absorption spectroscopy, can be achieved. The approach is versatile and can be used for a broad variety of analytes. Here, it was applied to the detection of phenol red, 10 nm gold nanoparticles and envy green fluorescence dye and I showed that the LOD decreases by a factor of 7.2 times for phenol red and a factor of 3.3 for nanoparticles and dye. Furthermore, sensitivity and working range of a commercially available hydrogen peroxide bioassay were improved almost by one order of magnitude, which convincingly demonstrates the versatility of the technique. The influence of the PS beads concentration and size, as well as the geometrical thickness L of the sample on the OPL in the disordered medium were investigated numerically and experimentally. Those parameters can be effectively used to tailor the enhancement for specific applications and analytes. The performed experiments are in excellent agreement with numerical simulations based on a probabilistic approach.

In the second part, I showed that the maximal absorption regime for a random medium corresponds to the following conditions: the filling factor F has to be high enough to sustain multiscattering in the medium and, at the same time, low enough to allow light to penetrate inside the material. I identified design rules for geometries where the introduction of a random medium becomes beneficial in terms of absorbed energy. The filling factor F_{cri} which maximizes light absorption depends on the relation between the mean free path of light l_{free} and the geometrical size of the medium, while the maximal absorbed energy E_{max} can be correlated with the transport mean free path l^*. The amount of absorbed energy can be further increased (from 1.7 to 23-fold) by introducing an open cavity around the random medium. Furthermore, the enhancement provided by the scattering medium decreases as the absorption α grows, because the nature of light propagation changes from diffuse to ballistic. The application of these principles to absorption for a photovoltaic system has been illustrated by demonstrating a 2.2 absorption enhancement when introducing a

random medium with appropriate filling factor in the system. The combination of an open reflective cavity with a random medium ensures strong photon confinement, with the additional benefits of wide-angled and broadband operation. This approach is promising for improving the efficiency of solar cells, as well as for sensing applications where the optical absorption of minute quantities of analyte must be detected.

Chapter 3 Continuous measurements of extracellular hydrogen peroxide

I n this chapter, I present a new device for the continuous measurements of oxidative stress by measuring one of the most stable ROS, namely H_2O_2. This portable oxidative stress sensor contains the heme protein cytochrome c (cyt c) as sensing element whose spectral response enables the detection of H_2O_2 down to a detection limit of 40 nM. The continuous measurement of extracellular H_2O_2 with this high sensitivity optical sensor is a promising new approach for real-time cytotoxicity tests and the investigation of oxidative stress. This work is further extended to a multiplexed platform for multianalyte detection. Based on the corresponding enzymatic reactions leading to H_2O_2, I develop multiscattering-enhanced and continuous biosensors for glucose and lactate. Further microfluidics integration enables multiplexed and crosstalk-free detection. This multifunctional detection scheme provides a powerful tool to study cellular processes.

3.1 Introduction

ROS generated by aerobic organisms are essential for physiological processes such as cell signalling, apoptosis, immune defence and oxidative stress mechanisms [2, 9-13]. Unbalanced oxidant/antioxidant budgets are involved in many diseases and, therefore, the sensitive measurement of ROS is of great interest [14-18]. However, intracellular measurements of ROS can interfere with redox cycles of cells and, therefore, are often only qualitative [174, 175]. In this regard, extracellular measurements represent interesting alternative and can provide additional information about the cellular processes [176]. Most ROS species are not likely to escape outside the cell, due to their extremely short lifetime: for example, O_2, $O_2^{\bullet-}$ and $OH^\bullet$ have lifetimes of 4 μs, 1 μs and 1 ns, respectively [177]. In contrast, H_2O_2 represents one of the most stable ROS, which can diffuse through the cell membrane [38, 178]. Thus, tracing the kinetics of H_2O_2 in biological systems provides further insight into the dynamics of ROS [179].

Real-time information on metabolic processes in cell cultures provides important insights into the cell state and the cellular mechanisms [180]. Furthermore, metabolome data can be used for medical diagnostics and health monitoring [181, 182]. Many researchers focus their attention to the detection of different metabolites such as cholesterol, glutamate, glucose and lactate [183, 184]. In particular, the detection of

glucose is interesting in the context of the biochemical cycle of energy harvesting, dia-diabetes pathology, as well as fermentation control in food industry [185-189]. Lactate, in addition, acts as a cerebral energy substrate and as a product in anaerobic metabolism during muscle contractions, malnutrition and hypoxia [190-195]. A sensitive method for the continuous and simultaneous detection of several metabolites will broaden our understanding of cell biochemistry with a significant impact on medical diagnostics. One strategy to detect many of these metabolites (including glucose and lactate) is to use the respective enzymatic reactions that convert these metabolites into H_2O_2 [196].

Up to date, mainly electrochemical biosensors are used for the detection of extracellular H_2O_2 [197, 198]. Large efforts have been put into the design of those sensors, especially structuring the electrodes with mediators, gels, polymeric matrices and various nanomaterials [199, 200]. Most reported methods are based on sample collection prior to laboratory analysis and are, therefore, end-point assays [201, 202]. Yet, most of the electrochemical sensors suffer from electrode fouling and lack of long-term stability [203]. Chemiluminescent and fluorescent biosensors represent another very sensitive way of sensing H_2O_2 [177, 204-208]; although their use for continuous measurements remains problematic because of their limited stability and deactivation by photobleaching [174, 175]. Overall, the development of a sensitive way to continuously measure extracellular H_2O_2 remains of great interest. In this context, I propose to use multiscattering-enhanced optical absorption as an alternative to existing methods.

In the first part of this chapter, I demonstrate a novel route for the sensitive detection of H_2O_2 based on the optical path length enhancement in random media discussed in the previous chapter. Additionally, I present a stand-alone portable oxidative stress sensor (POSS) for the non-invasive and continuous measurements of H_2O_2. To illustrate the potential use of the POSS in biological experiments, I study stress-related H_2O_2 release from the green microalga *Chlamydomonas reinhardtii*, a widespread microorganism present in soil and freshwater throughout the world. It is a primary producer at the base of the food chain and thus highly relevant from an ecotoxicological perspective [209]. To induce H_2O_2 generation, algae were either treated with functionalized CdSe/ZnS core shell Qdots that are widely used as fluorescent labels [210] or with TiO_2 nanoparticles, which are common constituents of everyday consumer products [211].

In the second part, I introduce non-invasive, multiscattering-enhanced and real-time biosensors with sub-micromolar LODs for lactate and glucose measurements. These sensors are integrated in a microfluidic multiplexed platform and, using this sensor, I demonstrated multianalyte detection. As an example, the uptake of exogenously supplied glucose on algae *C. reinhardtii* is quantified. Enabling the study of glucose uptake in algae provides new insights on several biochemical aspects: (1) the ability of algae to accumulate glucose, (2) whether glucose feeding can substitute light harvesting and (3) glucose metabolic pathways [212, 213]. It is known that large doses of glucose may misbalance cellular homeostasis and, therefore, harm the cells [214]. To assess the physiological state of algae, I simultaneously detect extracellular H_2O_2 using the multiplexing feature of our biosensor platform [176].

3.2 Multiscattering-enhanced optical probes based on cytochrome c

3.2.1 Protein cytochrome c and its properties

Cyt c is a hemoprotein consisting of a heme group that coordinates an iron atom. Cyt c is found in the membrane of mitochondria in plant and mammalian cells and forms an essential component of the electron transport chain [215, 216]. For instance, cyt c is capable of undergoing oxidation and reduction, changing the charge of the iron atom from 2+ to 3+ (Fig. 3.1a) [215]. Finally, it is an intermediate in apoptosis or so-called controlled cell death [216].
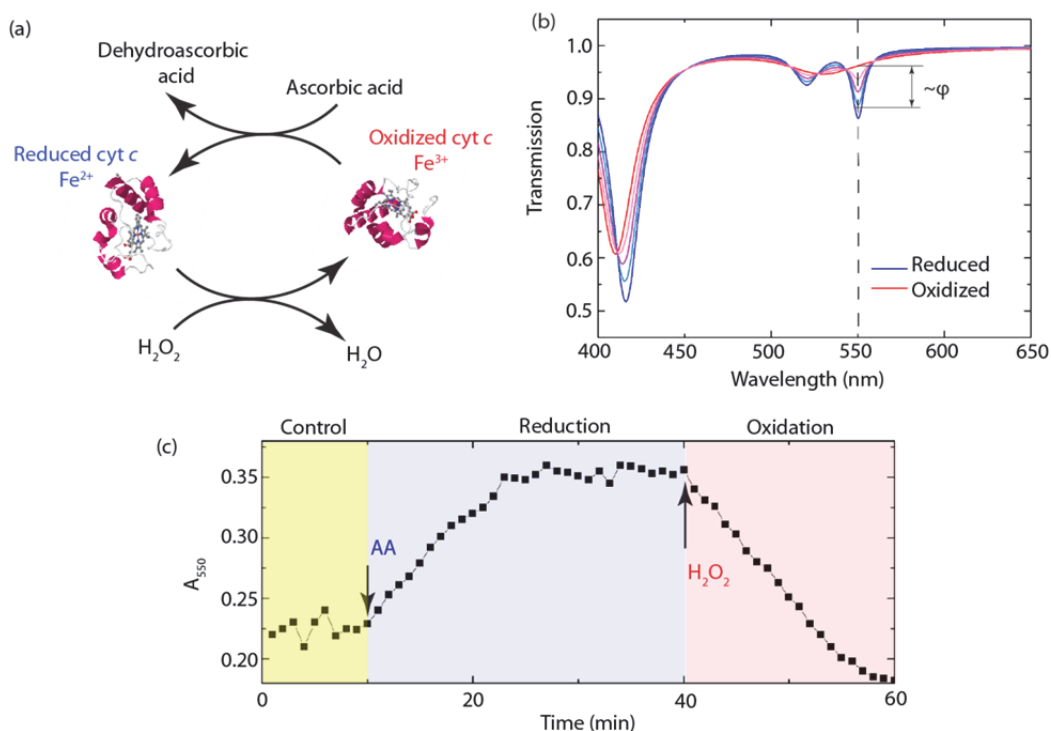
Figure 3.1. **Redox state-dependent optical absorption of cyt c.** (a) Schematic diagram of cyt c oxidizing in the presence H_2O_2, which is simultaneously converted to water, and reducing by ascorbic acid, which turns into dehydroascorbic acid. (b) Theoretical optical transmission spectra of cyt c in different redox states. The dashed line corresponds to the dip at $\lambda = 550$ nm. (c) Temporal measurements of absorbance at $\lambda = 550$ nm A_{550} for 40 μM solution of cyt c upon the addition of 1 μl AA ($C = 10$ mM) and 1 μl H_2O_2 ($C = 400$ μM). Respective time points of additions are indicated with arrows.

A change of the charge of the iron atom induces a conformation change of the heme group, which, in turn, is reflected in the optical absorption spectrum [217]. In particular, cyt c in the reduced state exhibits two absorption peaks at $\lambda = 410$ nm and 550 nm (Fig. 3.1b). In the oxidized form, the bands at $\lambda = 416$ nm and 520 nm emerge. Although the change of the $\lambda = 410$ nm absorption band is the most pronounced, the $\lambda = 550$ nm peak is more sensitive. Therefore, optical monitoring of cyt c absorption sets a basis for the detection of oxidation species, such as H_2O_2 or of reduction species like ascorbic acid (AA).

To illustrate the basic principle, I monitored the absorbance A_{550} at $\lambda = 550$ nm for a 40 μM cyt c (Sigma Aldrich) dissolved in deionized water (Fig. 3.1c). For this, the solution was introduced into the measurement chamber (60 μl, O-ring delimited). The absorption spectra were recorded in transmission mode under white-light illumination using an objective (UPlanFL 20x, Olympus, NA = 0.41) and a grating spectrometer (Triax 550, Horiba Scientific) equipped with a liquid nitrogen cooled CCD camera (Symphony, Horiba Scientific). All other experiments in this chapter are performed in the above mentioned configuration, unless stated otherwise. As a result, the value of A_{550} remains stable if nothing added. After the addition of AA (Sigma Aldrich) at $t = 10$ min, A_{550} starts to increase and reaches a plateau at $t = 25$ min, which corresponds to the reduction of cyt c. After the addition of H_2O_2 (Sigma Aldrich) at $t = 40$ min, A_{550} starts to decrease, meaning that cyt c switches from the reduced to the oxidized form. In conclusion, its oxidation/reduction capability makes cyt c an ideal candidate for H_2O_2 sensing.

3.2.2 Normalized redox state coefficient

To quantify the redox state of cyt c, I introduce a normalized redox state coefficient φ:

$$\varphi = \frac{A_{550}/A_{542} - A_{550}^{ox}/A_{542}^*}{A_{550}^{red}/A_{542}^* - A_{550}^{ox}/A_{542}^*},\tag{3.1}$$

where A_{550} and A_{542} are the measured cyt c absorbance at $\lambda = 550$ and $\lambda = 542$ nm, respectively. The parameters A_{550}^{ox}, A_{550}^{red} and A_{542}^* are values taken from the literature, representing the absorbance for the oxidized and reduced states at $\lambda = 550$ nm, and the absorbance at $\lambda = 542$ nm, respectively [215]. The absorbance is calculated as follows: $A = -\log(I/I_0)$, where I and I_0 are the intensities measured after the light passed through the cyt c and in the absence of cyt c, respectively. The optical path length can vary between different measurements, which can lead to ambiguity if we would only normalize A_{550} between A_{550}^{ox} and A_{550}^{red}. To overcome this difficulty, I rather work with the ratio A_{550}/A_{542}, since the absorbance at $\lambda = 542$ nm is independent of the redox state. In this way, the path length is cancelled out as shown below. Taking into account Beer-Lambert's law ($A = \alpha C l$), Eq. (3.1) can be rewritten as follows:

$$\varphi = \frac{\alpha_{550}C_1 l_1/\alpha_{542}C_1 l_1 - \alpha_{550}^{ox}C_2 l_2/\alpha_{542}^*C_2 l_2}{\alpha_{550}^{red}C_2 l_2/\alpha_{542}^*C_2 l_2 - \alpha_{550}^{ox}C_2 l_2/\alpha_{542}^*C_2 l_2} = \frac{\alpha_{550} - \alpha_{550}^{ox}}{\alpha_{550}^{red} - \alpha_{550}^{ox}},\tag{3.2}$$

where α_{550}, α_{542}, α_{550}^{ox}, α_{550}^{red} and α_{542}^{*} are the respective absorption coefficients. C_1 and l_1 are the cyt c concentration and the optical length through the sample and C_2 and l_2 the respective values from the literature [215]. This normalization results in $\varphi = 1$ for the fully reduced and $\varphi = 0$ for the fully oxidized state of cyt c.

3.2.3 Fabrication process: designs, preparation and pitfalls

To date, Vandewalle *et al.* detected micromolars of H_2O_2 by measuring A_{550} for cyt c in solution [218]. In order to detect lower H_2O_2 concentrations, the cyt c absorbance A must be amplified. Here, I discuss three approaches that I have attempted to enhance the absorption of cyt c in the random medium as well as difficulties associated with them.

Aggregates

The first approach is based on crosslinked aggregates of cyt c with PS beads. The incident light passing through such an aggregate experiences multiscattering due to the presence of PS beads that have a refractive index of $n = 1.6$ (Fig. 3.2a). To fabricate such aggregates, 200 μl of cyt c and 50 μl PS beads (0.49 μm diameter, Polysciences) were mixed under vigorous stirring in the presence of 0.5 μl of glutaraldehyde (25 %, Sigma-Aldrich). Glutaraldehyde crosslinks cyt c, forming spherical aggregates. PS beads are trapped inside this matrix (Fig. 3.2b). After one hour reaction time the formed aggregates were intensively washed by centrifugation (2 min, 8000 rpm), and then collected in deionized water and kept at 4 °C.

Fabricated samples show a redox behaviour changing their φ after the addition of 1 μM AA and 8 μM of H_2O_2 (Fig. 3.2c). They also demonstrate excellent optical path enhancement, which was estimated to be around 40 [176]. However, aggregates have several limitations. Since the crosslinking process is random, they come at broad range of sizes (from <0.1 to 3 mm in diameters). After manual selection and careful examination under the microscope, the aggregates with one specific size were chosen (0.5 mm diameter). Due to the variations in the number of PS beads and the amount of active cyt c in each aggregate, these samples showed quite different responses under exposure to the same amount of H_2O_2 (8 μM) (Fig. 3.2d). As a result, this configuration shows insufficient repeatability and reproducibility, since each aggregate is different.

Ink-jet printing

The second approach is based on ink-jet printing (MD-K-140, Microdrop Technologies GmbH, Germany) of a PS beads/cyt c solution [219]. This approach is based on drop on demand technology: a printing nozzle is connected to a piezoelectric material. When a voltage is applied, the piezoelectric material changes shape, generating a pressure pulse in the fluid, which forces a droplet of ink from the nozzle. In this way, controllable amounts of cyt c can be deposited on the surface of glass, while the presence of PS beads enables multiscattering (Fig. 3.3a,b). The fabrication process is the following: a mixture of 0.6 nM PS beads and 4 mM cyt c is prepared immediately before ink-jet

printing. I start printing by obtaining stable drops of water with optimized printing pa-
parameters (frequency of spotting, pulse length and voltage applied to the nozzle).
Afterwards the PS/cyt c mixture is printed on the glass microscope slide. As soon as the
printing is finished, the mixture is quickly replaced by water in order not to clog the tip
of the nozzle during drying. After deposition the printed aggregates are crosslinked
using glutaraldehyte in vapour phase for 1 h. Finally, the produced PS/cyt c aggregates
are stored at 4 °C in a closed container at 100 % relative humidity.
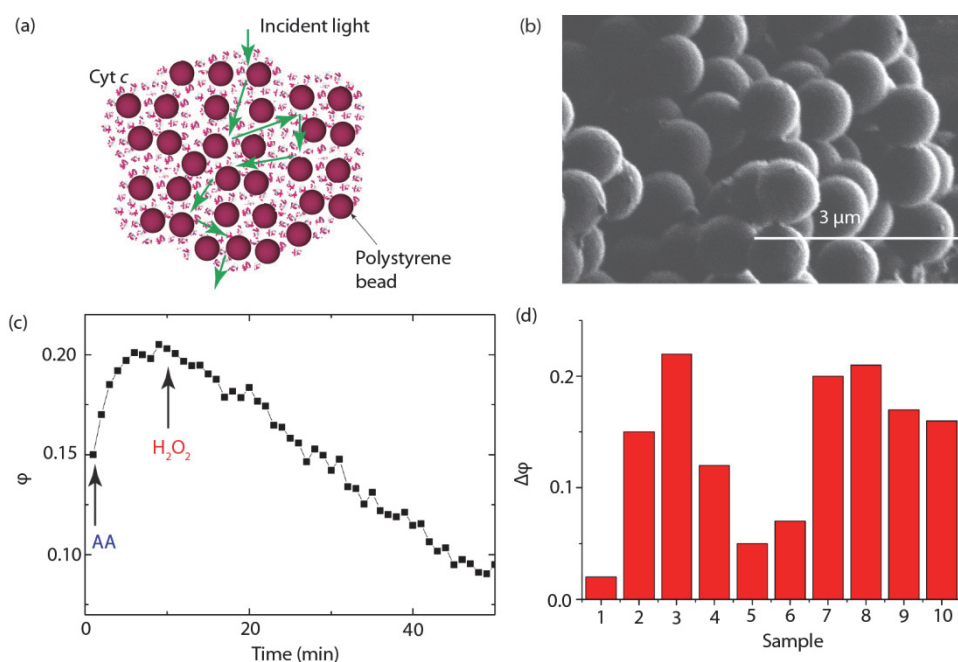
Figure 3.2. Cyt c/PS beads aggregates. (a) Schematic illustration of optical length
enhancement in an aggregate. (b) Focused Ion Beam image of the fabricated aggregate
(courtesy of Ch. Santschi). (c) Temporal measurements of φ for cyt c+PS bead aggregate
upon the addition of 1 μM AA and 8 μM of H_2O_2 into the measurement chamber.
Respective time points of additions are indicated with arrows. (d) The change of redox
state $\Delta\varphi$ within 30 min for 0.5 mm diameter aggregates in the presence of 8 μM H_2O_2; ten
different aggregates are measured.

With this ink-jet technique, it is possible to deposit in a controllable manner spots
containing different numbers of drops on the glass surface (Fig. 3.3c). However, there
are two difficulties associated with ink-jet printing. The first one is drying: spots dry
within a few seconds after printing. As a result, spots lose their 3D geometry and hence
their optical path enhancement. Indeed, optical profilometry confirmed that the spot
contains only a few layers of PS beads (Fig. 3.3d). Here, two possible improvements are

suggested: silanization of the surface and control of humidity. Indeed, silanization of the surface helps to retain the shape of the printed drop, but usually it is not compatible with biological measurements [220]. Moreover, the drop does not stick to the silanized surface and hence gets detached during measurements. The control of humidity (up to 80%) only partially improves the spreading of the spots over the glass substrate.
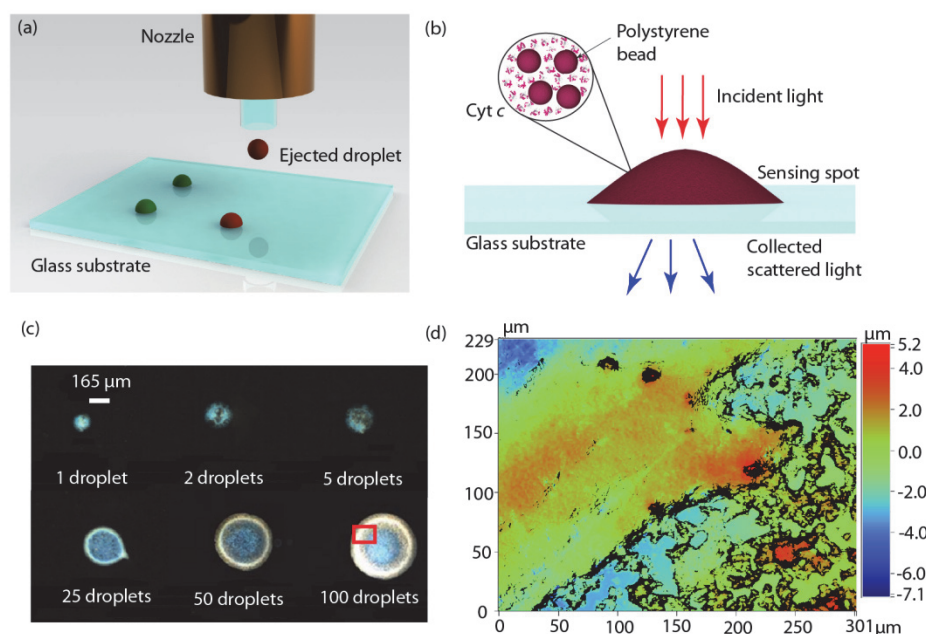
Figure 3.3. **Ink-jet printing of cyt *c*/PS beads drops.** (a) Schematic illustration of ink-jet printing. (b) Schematic illustration of an ink-jet printed spot on the glass substrate, with the bright-field measurement configuration. (c) Photographs of ink-jet printed drops consisting of different numbers of droplets. The round circle at the boundary is due to the coffee ring effect. (d) Optical profilometry measurement of the red area marked in the previous panel showing height of the printed spot (using Veeco Wyko NT1100 with a 30 nm resolution).

Another difficulty which occurs is clogging of the nozzle. When the nozzle with PS/cyt *c* solution is left alone for a few minutes (for example, between printing different samples), the water dries out and the PS beads clog the nozzle. Once I became aware of it, I have minimized the standalone time of the nozzle and the results improved. Nevertheless, clogging continued. It means that drying of the nozzle is one, but not the only problem of the system. After some time (around 30-60 min), PS beads start to sediment in the solution. Therefore, another reason for clogging is the uptake of the high concentration of PS beads, which sediment to the bottom of the vessel. To overcome this, I periodically stirred the mixture. Furthermore, I discovered that the

clogging reduces when the printer takes the mixture from the top part of the bottle and, instead of stirring, I just slightly shook the vessel. The drawback is that this process is not reproducible and the PS beads concentration is not well controlled. It has to be noted here that a very significant amount of work and time was invested into the cleaning of the clogged nozzles. The most efficient way was ultrasonication of the nozzle with periodic backpulling of the liquid with a syringe. Besides that, PS beads could be diluted in toluene. Despite the fact that the main problem of clogging was the presence of PS beads, there were cases where dissolution by toluene did not help. Sometimes at the tip of the nozzle I observed fibres which cause the clogging. Filtering water and cyt c solution with 0.2 μm filter did not improve the results. PS beads are produced in solution and therefore cannot be filtered. However, at this stage it is not entirely clear why exactly clogging occurs.

Microarray spotting

The third approach consists in microarray spotting of cyt c into a porous substrate. In contrast to the two previous approaches, here it is light scattering in the porous substrate (not the PS beads) that enhances the optical path length. Using the microarray robot (QArray2, Genetix) the aqueous droplets containing cyt c (4 mM) were picked up from a 384-well plate with a 5 nl delivery-volume spotting pin (946MP8XB, Arrayit) and subsequently deposited onto the hydrophilic membranes (GSWP 220 nm, Millipore, refractive index $n = 1.6$), which were placed on a glass substrate (Fig. 3.4a). Immediately after depositing cyt c, the spots were exposed to vaporous glutaraldehyde for 1 h. These crosslinked spots were then transferred into water and stored at 4°C prior the use. During the crosslinking process the spots are kept at 100 % relative humidity in order to avoid drying, which would, otherwise, denature the heme protein.

Optical measurements show an increased absorption of cyt c in the membrane, compared to the same amount of cyt c deposited on a flat glass substrate (Fig. 3.4b). This effect is caused by two factors: (1) due to the surface tension, drops on the glass surface form a thin layer (<10 μm), resulting in a smaller optical thickness; (2) light scattering taking place in the pores of the membrane enhances the optical path length [83]. The first effect was confirmed by observing cross-sections of the printed spot in the membrane. The enhancement factor f is defined as the ratio between cyt c absorbance A at $\lambda = 542$ nm for a spot on glass and a spot in the membrane. For a 20 pmol spot f is 4.6 ± 0.8 and 4.6 ± 1.2 in membranes with pore sizes 220 nm and 450 nm, respectively (Fig. 3.4f). Due to crosslinking, cyt c is partially denatured, remaining in its oxidized form and losing some of its pseudo-peroxidase behaviour, which is essential for our sensing purpose. To estimate the degree of denaturation, we measured the spectral response of several spots which were reduced in excess of AA (Fig. 3.4e). Spots deposited on glass and in 220 nm and 450 nm pore size membranes have φ values of 0.53±0.20, 0.41±0.03 and 0.48±0.09, respectively.

Cyt c in printed spots shows an excellent redox behavior: a completely oxidized spot can be reduced to its original redox state and, hence, reused for H_2O_2 detection up to five times (Fig. 3.4c). However, high H_2O_2 concentrations (>100 μM) irreversibly oxidize

and denature cyt c [217]. Yet, ten days old spots have constant coefficients φ demon-demonstrating a good lifetime for the sensing element (Fig. 3.4d).
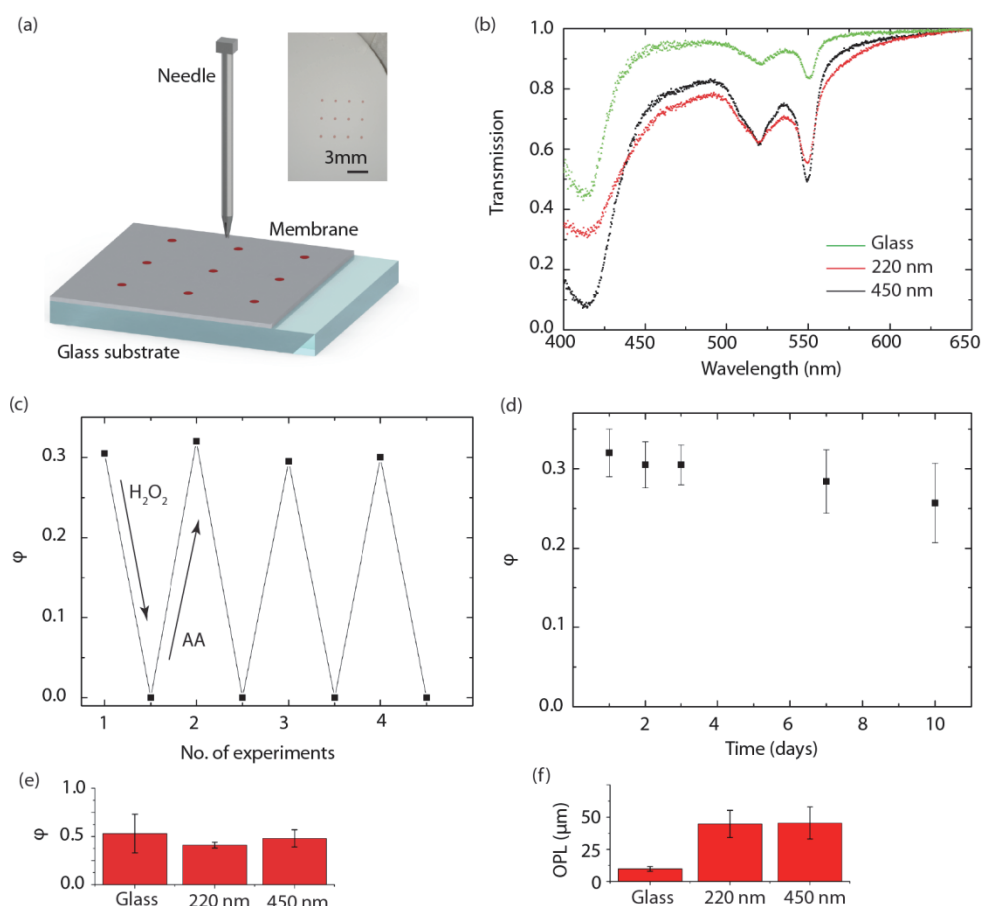
Figure 3.4. **Printed cyt c spots in a porous membrane.** (a) Schematic illustration of contact printing of cyt c onto the membrane. The inset shows a photograph of an array of printed spots. (b) Optical transmission of 20 pmol cyt c spots printed on glass, in 220 nm, or in 450 nm pore size membranes in the presence of AA. (c) Redox state coefficient φ of a cyt c spot in a 220 nm pore size membrane in AA and H_2O_2, as a function of the number of consecutive oxidation/reduction cycles. Prior to their utilization, the spots were reduced with AA and subsequently washed. φ was measured immediately after the addition of 20 µM of H_2O_2 and 30 min later. (d) Redox state coefficient φ of a cyt c spot in a 220 nm pore size membrane as a function of storage time. The spots were prepared as in (c). The error bars represent the standard deviation for 5 measurements. (e) Redox state coefficient φ in the presence of AA and (f) optical path length (OPL) for spots on glass, in 220 nm and 450 nm pore membranes. The error bars correspond to the standard deviation for 9 measurements, each on different sample.

3.3 Portable oxidative stress sensor: dynamic and extracellular H_2O_2 detection released from algae

In this section, I present a portable oxidative stress sensor (POSS) for the non-invasive and continuous measurements of H_2O_2 using the developed cyt *c* spots fabricated as described in the previous section. This compact POSS was specifically designed for efficient and easy field analysis.

3.3.1 Overview of the sensor

POSS is a home-built setup that can operate in both dark- and bright-field transmission modes. In order to guarantee a proper alignment and good stability, all components were fixed on a vertical mounting plate [221]. The sample holder and all optical elements including the spectrometer and light source are situated on the front side of the mounting plate (Fig. 3.5a, b), whereas the electromechanical components, including the power supply (TXH 120 124, Traco Power) and liquid pump (Xcalibur, Tecan), were mounted on the rear side. The sample was fixed on an *x-y*-translation stage (Thorlabs, MT1/M), which allowed for proper alignment with the objective. A LED (R11/D3/N/B, Relco Group Ltd, 3 W) was used as light source and the scattered light, containing the spectral information from the sample, was collected by the objective (UPlanFL 20x, Olympus, NA = 0.45). The collimated beam at the output of the objective was split into a camera (C270, Logitech) for imaging the sample and a spectrometer (HR4000+, Ocean Optics) for spectral analysis of the scattered light. The objective was mounted on a z-translation stage in order to adjust the focal distance to the sample. Finally, the microfluidic pump was controlled with Labview. The entire portable setup has the dimensions $30{\times}15{\times}45$ cm^3.

Samples were measured in two regimes: static and microfluidic. For measurements in the static regime, a small chamber, delimited by an O-ring ($9{\times}1$ mm, Volume = 60 μl, BRW), was filled with the solution of interest and the membrane containing the printed sensing spot (Fig. 3.5c). The chamber was sealed with a cover slip and any excess liquid was removed. For every measurement a new O-ring and a new sensing spot were used.

In the flow regime, the sensing spots were integrated into a microfluidic channel ($0.3{\times}1$ mm^2 cross-section area and 4 mm length) fabricated in PDMS using a casting replication process with molds prepared using standard photolithography (Fig. 3.5d). To guarantee an optimal tightness of the microfluidic channels, an additional PDMS layer (100 μm thickness) containing a hole to accommodate the porous membrane was added. These two PDMS layers along with the glass substrate were then clamped between two metallic plates. In order to optimize the performance of the sensor, the spot was aligned with respect to the center axis of the channel. The membranes were cut larger than the channels and were henceforth pinched by the top PDMS layer. Prior to the measurement, the channel was washed with deionized water for 10 min at a constant flow of 2 mm/sec. The solution of interest was then introduced at a constant flow rate (2 mm/sec). At the end of every measurement, the spot was removed and all

microfluidic components were thoroughly rinsed with distilled water. A new spot was then inserted for the next measurement.
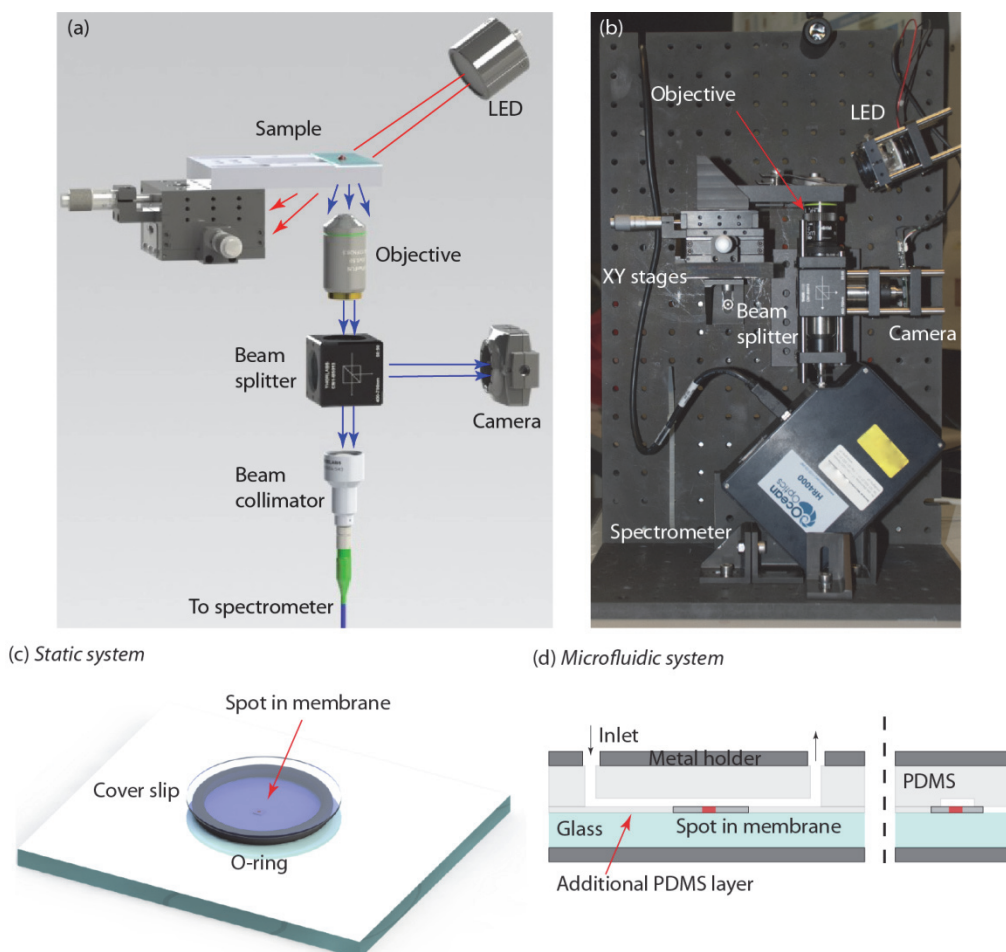
Figure 3.5. **POSS setup.** (a) Schematic drawing of the portable setup. For the sake of clarity, only the main elements are shown. Red arrows represent the light from the LED whereas blue arrows indicate the light scattered by the sample. (b) Picture of the portable setup (front view). (c) Schematic illustration of the static regime configuration: The membrane containing the spot is placed onto the glass substrate in the O-ring. (d) Schematic illustration of the microfluidic configuration in the flow regime (side and front views), the microfluidic chip is placed on the sample holder.

3.3.2 Sensor calibration

In order to relate the redox state coefficient φ to the H_2O_2 concentration, calibration experiments were performed. The kinetics of φ at different H_2O_2 concentrations in the static regime is shown in Fig. 3.6a. While 80 nM H_2O_2 only slightly oxidize cyt c ($\Delta\varphi = \varphi_0 - \varphi_t = 0.02$), 8 μM lead to a complete oxidation within 30 min. φ_0 and φ_t represent the redox states at $t = 0$ and $t = 30$ min, respectively. In the absence of H_2O_2 there is a slow oxidation of cyt c ($\Delta\varphi$ around 0.005 per 30 min), which has to be taken into account for data analysis. The calibration curve resembles a sigmoidal shape typical of such reactions (Fig. 3.6b) [222]. The achieved LOD, defined as the 3-fold of standard deviation, is 40 nM. For comparison, recently reported schemes for continuous H_2O_2 detection – based on fluorescent carbon nanotubes and electrochemistry – have their LODs in the micromolar range [177, 223]. The upper detection limit of the sensor corresponds to 4 μM for a 30 min measurement. Even higher H_2O_2 concentrations can be measured by tracking φ for shorter time periods. For a time interval of 1 min, I estimated an upper detection limit of 80 μM for a 20 pmol cyt c spot. Finally, the detection limit for this class of sensors exchanges with the observation time [177]. For example, cyt c spot can detect 1 μM of H_2O_2 with an acquisition time of 10 min.
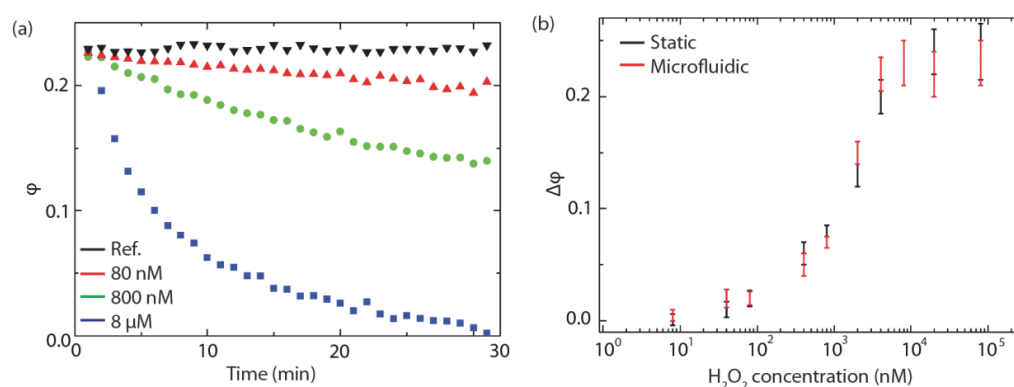
Figure 3.6. **Kinetics of cyt c redox reaction in the presence of H_2O_2.** (a) Time evolution of the redox state coefficient φ for different H_2O_2 concentrations for a 20 pmol spot of cyt c in a 220 nm pore membrane in the static regime measured using POSS. The reference measurements are performed in deionized water. (b) Calibration curve of the change of the redox state $\Delta\varphi$ after 30 min for the static and microfluidic regimes. Error bars represent the standard deviation over 3 measurements.

As follows from Fig. 3.4e, roughly 40% of the cyt c – corresponding to 8 pmol – remain active after crosslinking. On the other hand, the 60 μl O-ring filled with 80 nM H_2O_2 corresponds to 4.8 pmol. Provided a 1:1 stoichiometric relation, H_2O_2 can maximally oxidize 60% of cyt c in the spot. However, the reaction is very slow and within 30

minutes I only observe 2% oxidation. This can be due to the depletion of H_2O_2 near the cyt c spot and/or to slow reaction kinetics. Since a similar behaviour is observed in both static and microfluidic regimes, I exclude the H_2O_2 depletion scenario. Below, I provide a more quantitative discussion of the reaction kinetics.

3.3.3 Reaction kinetics

The reaction between cyt c and H_2O_2 is described by Fenton's reaction [224]:

$$Fe^{2+} + H_2O_2 = Fe^{3+} + HO\cdot + OH^-. \tag{3.3}$$
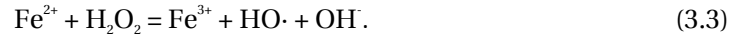
The rate of reaction (3.3) is only determined by the availability of H_2O_2 and cyt c, and can be expressed as follows:

$$\begin{cases} \frac{dN_{H2O2}}{dt} = -\tilde{k}N_{H2O2}N_{cytc} \\ \frac{dN_{cytc}}{dt} = \frac{dN_{H2O2}}{dt} \end{cases}, \tag{3.4}$$

where N_{cytc} and N_{H2O2} stand for the number of molecules of reduced cyt c and H_2O_2, respectively; $\tilde{k}$ is the reaction constant. In the microfluidic case fresh H_2O_2 is continuously injected into the system, resulting in a constant H_2O_2 concentration. Consequently, a first order approximation which fulfils Eq. (3.4) can be applied:

$$N_{cytc} = N_{cytc}^0 e^{-N_{H2O2}\tilde{k}t}, \tag{3.5}$$

where N_{cytc}^0 is the reduced amount of cyt c at $t = 0$. Dividing Eq. (3.5) by the total amount of cyt c and introducing $k = \tilde{k}V$ (V is the volume of the chamber) results in:

$$\varphi = e^{-C_{H2O2}kt}. \tag{3.6}$$

The interaction constant k is obtained by fitting Eq. (3.6) to the experimental data (Fig. 3.6a), yielding 0.24±0.06 min^{-1}·µM^{-1}. The obtained values agree well with data from literature for the interaction between cyt c and H_2O_2 in solution (0.13 min^{-1}·µM^{-1}) [218].

I propose a 1D diffusion model (Fick's second law) with a cyt c layer at $x = 0$ to simulate the reaction kinetics and the diffusion of H_2O_2 in the static configuration (Fig. 3.7a). The kinetics of the cyt c – H_2O_2 reaction is described by Eq. (3.4) and the reaction itself takes place in the proximity of the cyt c spot. H_2O_2 diffusion is simulated with the diffusion constant $D = 10^{-9}$ m^2/sec [225]. I study the reaction kinetics using two extreme conditions: (1) $N_{H2O2}^0 \gg N_{cytc}^0$ and (2) $N_{H2O2}^0 \ll N_{cytc}^0$, and compare them with the microfluidic regime, where N_{H2O2}^0 is constant over time. In the first case, I consider $N_{cytc}^0 = 20$ pmol of fully reduced cyt c and $N_{H2O2}^0 = 480$ pmol H_2O_2 (equivalent to $C_{H2O2} = 8$ µM in the reaction chamber). Only 2% of C_{H2O2} is sufficient to fully oxidize cyt c within 30 min (Fig. 3.7b,c). Static and microfluidic responses are identical, which is in agreement with our experiments. In the second case, I analyse $N_{cytc}^0 = 20$ pmol cyt c and $N_{H2O2}^0 = 0.48$ pmol H_2O_2 (equivalent to $C_{H2O2} = 8$ nM). Even after 5 h no H_2O_2 depletion

occurs (Fig. 3.7d). φ changes slowly from 1 to 0.97 (Fig. 3.7e). The difference between static and microfluidic regimes becomes significant only after 3 h, due to the H_2O_2 conconsumption in the former, while for shorter periods the φ responses are the same. Thus, our simulations confirm similar reaction kinetics in both regimes, which is also reflected by the calibration curves shown in Fig. 3.6b. Equations (3.5) and (3.6) can, therefore, be extended to the static case. Also, the presence of the cyt c spot only slightly affects the H_2O_2 concentration and, consequently, does not deteriorate the measurements.
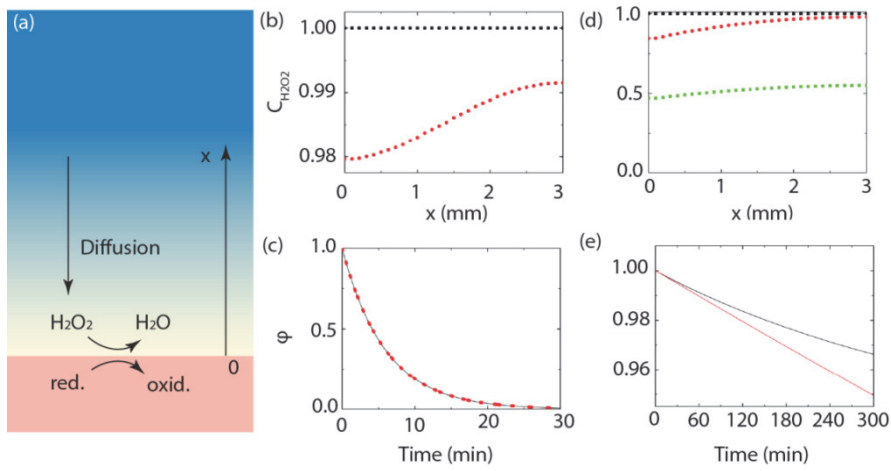
Figure 3.7. **Biosensor response simulations.** (a) Schematic of the 1D simulation showing a chamber filled with H_2O_2 reacting with cyt c at the interface $x = 0$. (b) Normalized H_2O_2 concentration C_{H2O2} for 20 pmol cyt c and 480 pmol H_2O_2 at $t = 0$ (black) and 30 min (red). (c) Redox state coefficient φ kinetics for the reaction in (b) for the microfluidic (dotted red) and static (black, overlaps) regimes. (d) C_{H2O2} for 20 pmol cyt c and 0.48 pmol H_2O_2 interaction at $t = 0$ (black), 30 min (red) and 5 h (green). (e) Redox state coefficient φ kinetics for the reaction in (d) for the microfluidic (red) and static (black) regimes.

In biological systems H_2O_2 is generated with time-dependent rates. I can quantify the H_2O_2 concentration at a given time t with Eq. (3.5) by considering the derivative of the measured φ value:

$$\frac{d\varphi/dt}{\varphi} = \frac{dN_{cytc}/dt}{N_{cytc}} = -kC_{H2O2}. \tag{3.7}$$

Finally, I introduce the probability of cyt c to be oxidized in the presence of a given H_2O_2 concentration. This coefficient is defined as the ratio between the amount of H_2O_2 that

interacts with cyt c ($dN_{interact}$) and the amount that reaches the spot in a given second (dN_0). The first quantity can be calculated using Eq. (3.7), while the latter is obtained from the molecular dynamics theory as the number of molecules hitting the surface in a given time:

$$\psi = \left|\frac{dN_{interact}}{dN_0}\right| = \left|\frac{dN_{H2O2}/dt}{\frac{1}{4}C_{H2O2}v_{H2O2}A_{spot}}\right| = \frac{kC_{H2O2}N_{cytc}}{\frac{1}{4}C_{H2O2}v_{H2O2}A_{spot}} = 4\frac{\varphi k N_{cytc}^0}{\frac{3D}{l_{free}}A_{spot}} = \frac{4kN_{cytc}^0 l_{free}}{3DA_{spot}}\varphi, \quad (3.8)$$

where v_{H2O2} is the thermal velocity of H_2O_2 molecule in water, A_{spot} the area of the sensing spot($\approx 2.83 \cdot 10^{-7}\ m^2$), l_{free} the mean free path of H_2O_2 molecules in water ($\approx$0.25 nm). ψ does not depend on the H_2O_2 amount and is only a property of the cyt c spot. A given spot can be fully characterized by N_{cytc}^0 and A_{spot}, by introducing the unitless coefficient of interaction:

$$\gamma = k\frac{4N_{cytc}^0 l_{free}}{3DA_{spot}}, \quad (3.9)$$

which can be approximated by $\gamma \approx 9.4 \cdot 10^{-5}$, representing the probability of H_2O_2 to oxidize cyt c per collision with cyt c when reaching the fully reduced spot surface ($\varphi = 1$). Finally, with $\psi = \gamma \cdot \varphi$, the probability of interaction with cyt c decreases proportionally with φ.

3.3.4   Proof of concept

Algal culture and exposure

The green alga *Chlamydomonas reinhardtii* strain (CPCC 11) was provided by the Canadian Phycological Culture Center. Axenic cultures were grown in four times diluted Tris-acetate-phosphate (TAP×4) liquid medium and maintained in an incubator (Infors, Bottmingen, Switzerland) at 20°C with a 24 h illumination regime (114.2 µmol·phot/(m²·s)) and constant rotary shaking (100 rpm). The algal culture was grown to a density of ca. 10^6 cells/ml.

In order to transfer the algae from the growth medium to water, they were centrifuged at 3000 rpm for 5 min and the supernatant was replaced by the same amount of PBS. This procedure was repeated twice. For oxidative stress studies algae were mixed (1:1 in volume) either with 18 nm primary size TiO_2 nanoparticles (Sigma Aldrich), or cadmium ion solution (Sigma Aldrich) or CdSe/ZnS Qdots (Life Technologies). To quench H_2O_2 in the measurement chamber, 100 µM of horseradish peroxidase (Sigma Aldrich) was added to the sample 10 min prior to the measurement. To measure intracellular ROS, the sample was incubated with 20 µM CM-H_2DCFDA dye (Sigma Aldrich) for 30 min in the dark. Its fluorescent intensity was measured in a multi-well plate reader (Safire2, Tecan) at $\lambda = 525$ nm with an excitation of $\lambda = 495$ nm. Positive controls were obtained by exposing algae for 30 minutes to 10 mM H_2O_2 before subsequent incubation with CM-H_2DCFDA. To determine H_2O_2 concentrations, I also used an alternative end-point method: 250 µl of the sample were incubated with 25 µl of bioassay (STA-343, Cell

Biolabs) for 30 min in the dark. Its absorption was measured in a multi-well plate reader at $\lambda = 595$ nm and compared to the calibration curve made with H_2O_2 standards.

Experiments

To demonstrate the performance of the POSS, I study the kinetics of stress-related H_2O_2 released by *C. reinhardtii* in the static configuration. First, algae were exposed to 500 nM Cd^{2+}, which is highly toxic and known to induce oxidative stress [176]. Indeed, after 2 h of exposure, I measured a H_2O_2 concentration of $C_{H2O2} = 950\pm100$ nM in the Cd/algae suspension (Fig. 3.8a). Unexposed algae do not produce any H_2O_2 with the respective C_{H2O2} values being below the detection limit. Intracellular ROS levels increase in identical conditions, correlating well with our findings (Fig. 3.8b). To exclude a possible interference of cells, Cd^{2+} or ROS with the sensing element, I carefully extracted the supernatant from the sample by centrifugation. The obtained C_{H2O2} values of the supernatant (900±120 nM) are in excellent agreement with that in the Cd/algae suspension. Moreover, an alternative end-point bioassay confirmed the presence of H_2O_2 in the supernatant with $C_{H2O2} = (1.0\pm0.3$ μM). To further demonstrate that POSS indeed senses H_2O_2, I added 100 μM horseradish peroxidase (HRP) to the supernatant to selectively catalyse the decomposition of H_2O_2 into water. As a result, C_{H2O2} decreased to the background values of the negative controls (130±110 nM).

Next, I expose algae to 140 nM Qdots (Fig. 3.8c) and 10 mg/l TiO_2 nanoparticles (Fig. 3.8d). Qdots induce a rapid increase of C_{H2O2} already after 5 min that reaches a value of 700 nM at 1h. This indicates the oxidative stress, which was also observed for the same Qdots in smaller concentrations but for longer exposure times [226]. On the other hand, algae exposed to 10 mg/l TiO_2 nanoparticles produced 40 nM H_2O_2 after 1 h, proving that TiO_2 nanoparticles do not induce elevated ROS levels in algae at this concentration [227]. Control experiments with Qdots/nanoparticles suspended in PBS without algae did not show any effect on the redox state of cyt *c.*
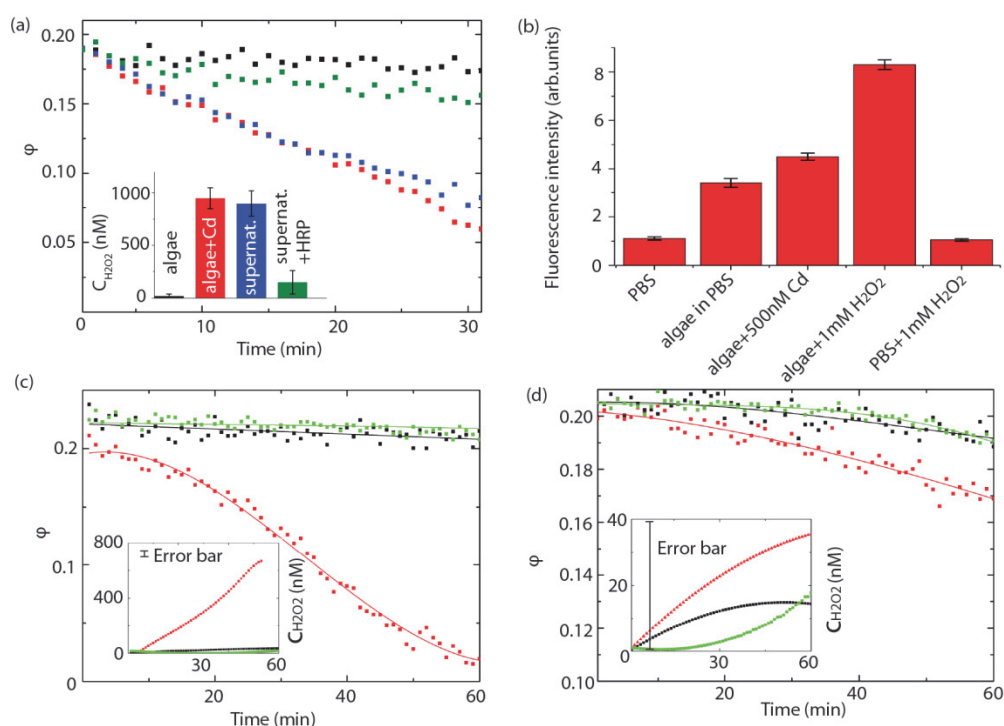
Figure 3.8. **POSS proof of concept.** (a) Time evolution of φ for algae (black), algae incubated in 500 nM Cd^{2+} for 2 h (red), supernatant extracted from it (dark blue) and a mixture of supernatant with 100 μM HRP (green). The corresponding inset shows the time average C_{H2O2} calculated using Eq. (3.7) (C_{H2O2} does not change significantly with time). (b) Intracellular ROS fluorescence intensity of 20 μM H$_2$DCFDA dye. Error bars represent the standard deviation over 3 measurements. Time evolution of φ for algae suspended in PBS solution (black) and algae exposed to (c) 140 nM of CdSe/ZnS Qdots and (d) 10 mg/l TiO$_2$ nanoparticles (red). Respective control curves of only Qdots and nanoparticles are shown in green. All curves are fitted with a polynomial function. Insets show the time evolution of C_{H2O2} calculated using Eq. (3.7).

3.4 Multiplexed platform for multianalyte detection

For the detection of lactate, respectively glucose, hybrid spot mixtures of cyt c with different amounts of the corresponding enzymes (lactate oxidase, respectively glucose oxidase) were deposited following the same procedure as cyt c spots (Fig. 3.9). I call these spots – hybrid spots.
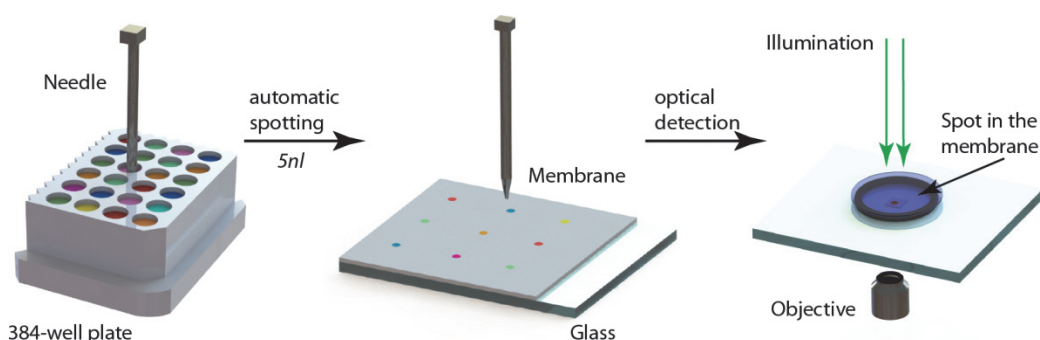
Figure 3.9. **Multianalyte spots printing.** Solutions containing cyt c + enzyme mixtures in microliter well-plates are automatically spotted onto a porous membrane using a microarray robot. The resulting crosslinked spots have a diameter of approx. 600 μm and are spectrally analysed in transmission.

3.4.1 Glucose and lactate detection

Control experiments with glucose and lactate revealed no interaction with cyt c. The redox state coefficient φ remains constant when a cyt c sensing spot (20 pmol) is placed into the chamber containing 440 μM of glucose (Fig. 3.10a). After addition of glucose oxidase (GOx, 500 U/ml), the glucose is catalytically converted into pyruvate and H_2O_2. The latter gradually oxidizes cyt c, decreasing the redox state coefficient φ. Further control experiments confirmed that GOx does not react with cyt c. Similarly to glucose, the presence of 24 μM of lactate does not induce any changes in the redox state of cyt c (Fig. 3.10d). However, the subsequent addition of 2.5 U/ml lactate oxidase (LOx) results in an oxidation of the cyt c in the spot. In contrast to GOx, LOx alone slightly oxidizes cyt c, changing φ from 0.25 to 0.16 within 30 min. (see the green curve in Fig. 2d).

Since the presence of enzymes in the solution can interfere with cyt c, I prepared hybrid spots containing cyt c and the corresponding enzyme. In such a configuration the H_2O_2 conversion and detection occur locally, which significantly reduces the amount of enzyme required. Additionally, since both cyt c and the corresponding enzyme are immobilized during crosslinking, such a configuration also eliminates the dynamic direct interaction between the two. In that case, 0.01 U of GOx, respectively 1.25×10^{-4} U of LOx, in the 5 nl printed sensing spot are sufficient to sensitively detect glucose respectively lactate (Fig. 3.10b and 3.10e). The calibration curves for these hybrid spots, which show the difference between the initial and the final redox state coefficients $\Delta\varphi = \varphi_{initial} - \varphi_{final}$ after 30 min, are shown in Fig. 3.10c and 3.10f. From these data I deduce a LOD of 9.6 μM for lactate and 1.1 μM for glucose for the above mentioned enzymes concentrations. The LOD decreases when one increases the amount of enzyme: the LOD for lactate is as small as 0.24 μM with 2.5×10^{-3} U of LOx, Fig. 2f; while the LOD for glucose is 0.11 μM with 0.1 U of GOx, Fig. 2c. To the best of my knowledge, these values are at least one order of magnitude lower than those reported in the recent literature [199].
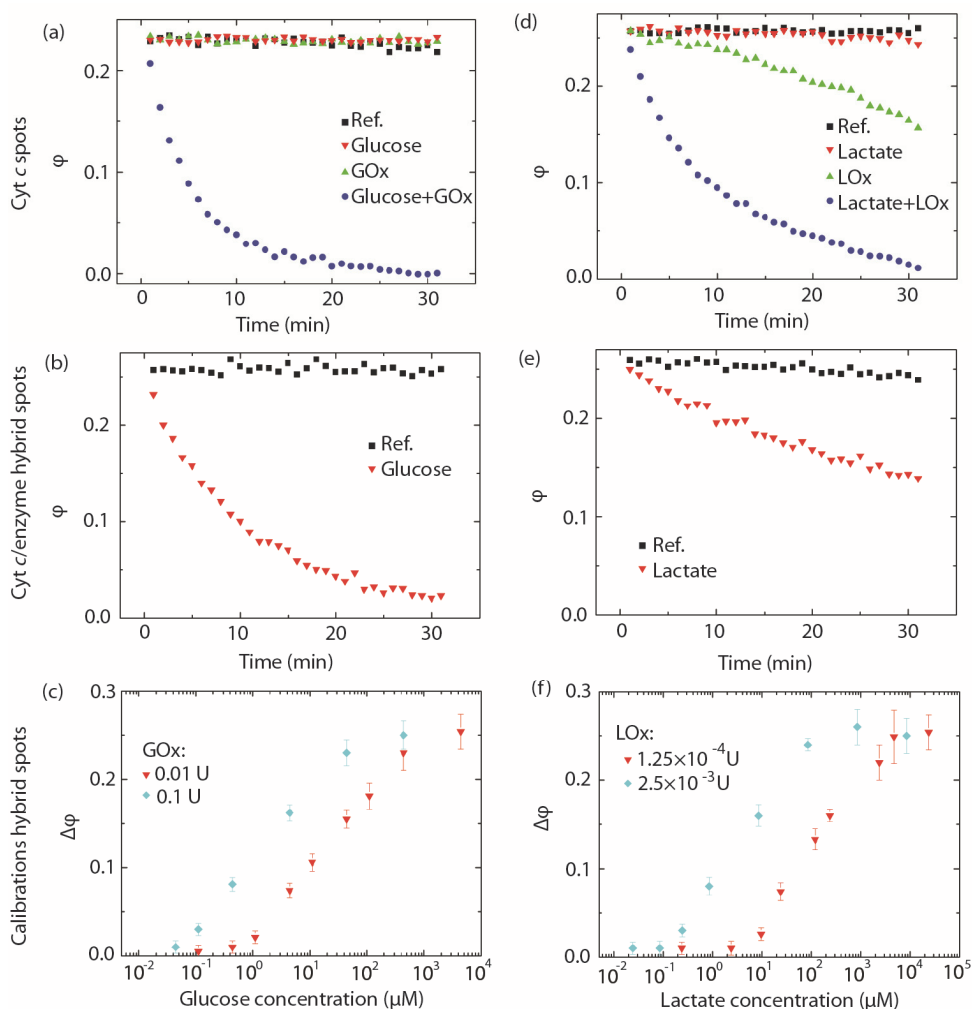
Figure 3.10. **Redox state coefficient φ for hybrid spots.** (a) Time evolution of the redox state coefficient $\varphi(t)$ for a 20 pmol cyt c sensing spot exposed to water (Ref.), to a 440 μM glucose solution in water (Glucose), to a 500 U/ml GOx solution in water (GOx), or to a solution with 440 μM glucose and 500 U/ml GOx in water (Glucose + GOx). (b) Time evolution of the redox state coefficient $\varphi(t)$ for a hybrid sensing spot containing 20 pmol cyt c and 0.01 U GOx exposed to water (Ref.) or to a 440 μM glucose solution in water (Glucose). (c) Calibration curve: response of the hybrid sensing spot in (b) after 30 min. as a function of the glucose concentration, for two different concentrations of GOx in the sensing spot: 0.1 U and 0.01 U. (d) Time evolution of the redox state coefficient $\varphi(t)$ for a 20 pmol cyt c sensing spot exposed to water (Ref.), to a 24 μM lactate solution in water (Lactate), to a 2.5 U/ml LOx solution in water (LOx), or to a solution with 440 μM glucose and 2.5 U/ml LOx in water (Lactate+LOx). (e) Time evolution of the redox state coefficient $\varphi(t)$ for a hybrid sensing spot containing 20 pmol cyt c and 1.25×10^{-4} U LOx exposed to water (Ref.) or to a 24 μM lactate solution in water (Lactate). (f) Calibration curve: response of the hybrid sensing spot in (e) after 30 min. as a function

of the lactate concentration, for two different concentrations of LOx in the sensing spot: 1.25×10^{-4} U and 2.5×10^{-3} U. The error bars in (c) and (e) represent the standard deviation over 3 measurements.

3.4.2 Multiplexing measurements

The possibility of multiplexed analysis allows simultaneous detection of several analytes and can also be used to reduce background contributions and obtain a more reliable statistics [228-231]. A multiplexed experiment is shown in the inset of Fig. 3.11d, where two sensing spots spaced 1 mm apart are visible in the measurement chamber; the spots can include cyt c or a mixture of cyt c and enzyme. In order to perform multiplexed measurements, absorption spectra from different sensing spots must be recorded simultaneously, which requires a precise alignment in the microscope, while additional markers on the membrane are used to identify the sensing spots (Fig. 3.11d inset).

Enzymatic reactions result in the production of H_2O_2 in the vicinity of the sensing spot and – by diffusion – in an increased concentration in the solution, which can interfere with neighboring sensing spots. To investigate such interferences, I loaded the experimental chamber with different combinations of pairs of sensing spots and exposed them to H_2O_2, glucose and lactate (Fig. 3.11a – c).

The sensing spots contain either 20 pmol cyt c (green in Fig. 3.11), or 20 pmol cyt c and 1.25×10^{-4} U LOx (blue in Fig. 3.11), or 20 pmol cyt c and 0.01 U GOx (red in Fig. 3.11) and are always exposed in pairs, which provides quantitative measurements for the crosstalk between them. In the first series of experiments, reported in Fig. 3.11a, I expose the three different possible combinations of sensing spots to 800 nM H_2O_2. Hybrid spots containing both cyt c and an enzyme exhibit a slightly lower response to H_2O_2 as compared to the spot containing only cyt c, probably because the presence of enzyme hinders the access of analytes to the cyt c. I then repeat these experiments, exposing the pairs of sensing spots to 440 μM glucose (Fig. 3.11b), or 90 μM lactate (Fig. 3.11c). As anticipated, when glucose reacts with the cyt c + GOx hybrid sensing spot, the enzymatically produced H_2O_2 also oxidizes the neighbouring cyt c sensing spot, which $\Delta\varphi$ increases from 0.038 to 0.042, Fig. 3b. This crosstalk is more pronounced when lactate reacts with the cyt c + LOx hybrid sensing spot; in that case, the $\Delta\varphi$ of the neighboring cyt c sensing spot increases to 0.014, as compared to 0.007 when no reaction happens in the hybrid spot, Fig. 3.11c.
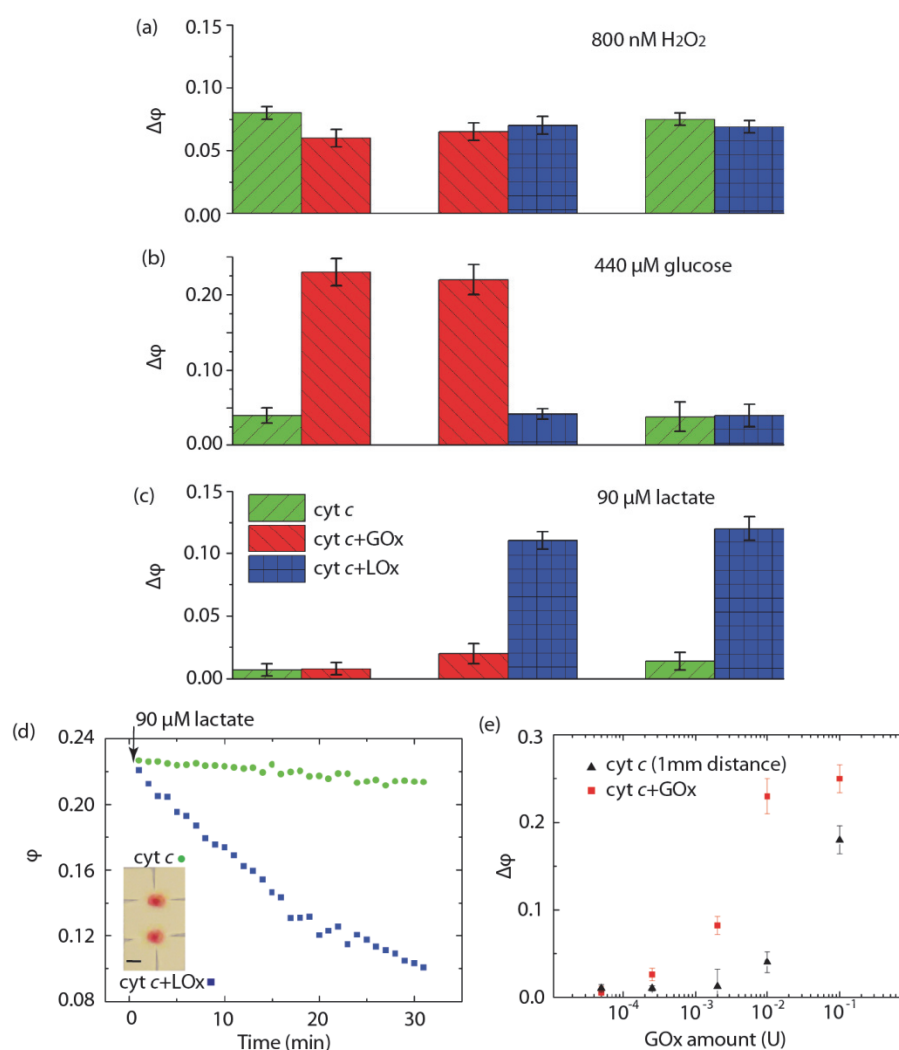
Figure 3.11. **Multiplexed measurements using different pairs of sensing spots** in the O-ring measurement chamber (photo in panel d, the distance between the spots is 1 mm and the scale bar is 0.5 mm): green, spot with 20 pmol cyt *c*; red: 20 pmol cyt *c*+0.01 U GOx; blue: 20 pmol cyt *c*+1.25×10^{-4} U LOx. Response after 30 min. of the three different pairs of sensing spots to (a) 800 nM H$_2$O$_2$, (b) 440 µM glucose and (c) 90 µM lactate. (d) Kinetics of the multiplexed redox state coefficient φ for a pair of spots (green and blue) exposed to 90 µM lactate. (e) Calibration curve: difference of the redox state coefficient after 30 min. $\Delta\varphi$ for different amounts of GOx in hybrid spots containing 20 pmol cyt *c*+GOx, after exposure to 440 µM of glucose; the response of a spot containing only 20 pmol cyt *c*, 1 mm away from the hybrid spot is also shown (crosstalk). The error bars represent the standard deviation over 3 measurements.

The sensitivity of such a hybrid spot depends on the conversion rate to H_2O_2, which in turn depends on the amount of enzyme. To investigate this, I have exposed hybrid sens-sensing spots containing different amounts of GOx to a constant glucose concentration of 440 µM. Figure 3.11e indicates that the difference $\Delta\varphi$ of redox state coefficient after 30 min. $\Delta\varphi$ increases with the GOx amount. Thus, adjusting the amount of GOx controls the sensitivity and dynamic of the sensor. Unfortunately, increasing the amount of enzymes also increases the enzymatically produced H_2O_2, which augments the crosstalk between neighboring sensing spots. A simple way to reduce crosstalk is to increase the distance between neighboring spots [231], or to use a hetero bilayer configuration [232].

3.4.3 Crosstalk suppression using microfluidic chip

A more drastic way to suppress interference effects is to integrate the sensing spots in a 2-layer microfluidic chip, which was fabricated in PDMS using a casting replication process with molds that were made with a standard photolithography technique (Fig. 3.12a and 3.12b). Briefly, the bottom PDMS layer (100 µm thickness) was deposited by spin-coating PDMS at 500 rpm for 40 s, followed by manual hole cutting to accommodate the sensing spots. This layer serves as planarization layer. The top layer (5 mm thickness) contained the microfluidic channels (0.3 mm×0.6 mm cross section) and a 3 mm wide chamber for experiments with cells, Fig. 3.12a and 3.12b. It was prepared by pouring the appropriate amount of PDMS onto the mold. The whole system was clamped in a metallic holder with the possibility of being disassembled to exchange the substrate with the sensing spots. Injecting and rinsing analytes was performed by applying a constant flow of 0.2 mm/sec using a liquid pump (Xcalibur, Tecan).

The sensing spots are introduced into the bottom layer and aligned with respect to the microfluidic channels in the top layer, one sensing spot per channel, so that enzymatically produced H_2O_2 remain within the channel and does not interfere with another sensing spot. In the following, I will perform experiments with algae and the microfluidic chip contains a 10 µl cell chamber, Fig 3.12a. Since the microfluidic channel has a very small volume (approx. 0.15 µl) the reaction of the analyte with the sensing spots could deplete the concentration of the former, interfering with the experiments [233]. The large cell chamber volume significantly increases the total volume of the system, so that diffusion effectively repletes H_2O_2 in the sensing channels [233].

As shown in Fig. 3.11, multiplexed experiments performed in the O-ring measurement chamber interfere; in contrast, this is not at all the case in the microfluidic chip. This is visible in Fig. 3.12c, where I compare measurements performed in the microfluidic chip with a 0.2 mm/sec flow (noted with an asterisk) with measurements in the O-ring measurement chamber. Even for the very high lactate concentration used here (almost 10x higher than the concentration used in Fig. 3.11d), the response of the pure cyt c sensing spot remains almost constant (blue inverted triangles in Fig. 3.12c), while lactate is well measured by the hybrid spot (green triangles in Fig. 3.12c). This absence of crosstalk in the microfluidic chip is also true in the static regime (no flow, data not

shown). Such a microfluidics approach could be used to detect a larger number of ana-analytes, by merely increasing the number of channels and sensing spots in the chip, Fig. 3.12b.
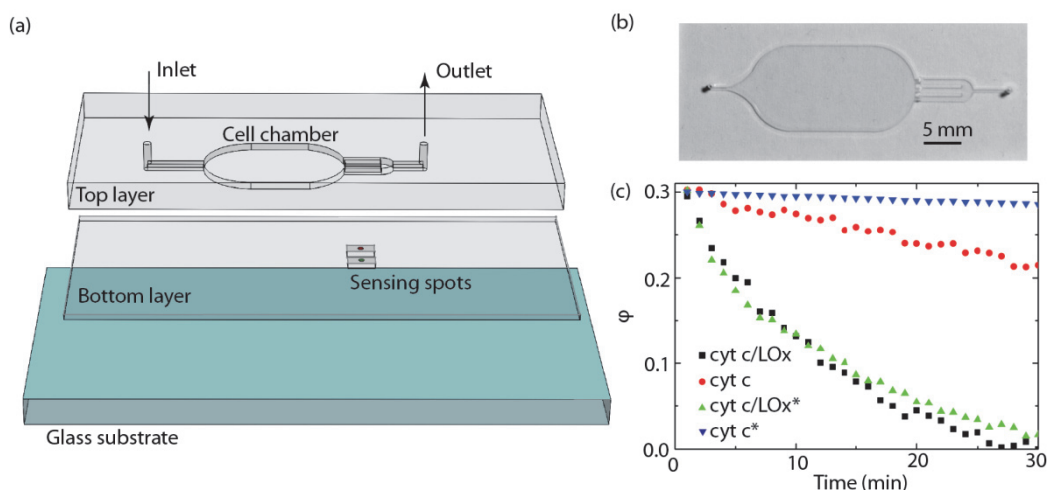
Figure 3.12. **Microfluidic chip suppresses cross-talk between spots.** (a) Schematic of the microfluidic chip consisting of a glass substrate, a bottom PDMS layer containing the sensing spots and a top PDMS layer with channels and cell chamber. (b) Picture of a top layer with three microfluidic channels coming out of the cell chamber. (c) Comparison of crosstalk between two sensing spots, one with 20 pmol cyt c and another one with 20 pmol cyt c+2.5×10^{-3} LOx exposed to 850 μM lactate. The asterisk denotes the experiment performed in the microfluidic chip with a 0.2 mm/sec flow; the other experiment is performed in the O-ring chamber.

3.4.4 Time-dependent rate determination

Till now, I have detected constant concentrations of analytes. However, in biological processes the release or uptake of biomarkers has a time-dependent rate. In this case, the concentration C_{H2O2} of H_2O_2 in the proximity of the sensing spot at a given time t can be determined using Eq. (3.7).

To link C_{H2O2} with the analyte (glucose or lactate) concentration $C_a(t)$, let us look into the reaction kinetics. In hybrid spots, the reaction of the analyte with the enzyme follows the Michaelis–Menten kinetics [234]. The resulting enzymatically-produced H_2O_2 partially reacts with cyt c, while the rest diffuses throughout the chamber. The consumed analyte creates a concentration gradient at the proximity of the sensing spot, where the analyte concentration can differ from $C_a(t)$. In general, an exact relation

between C_{H2O2} and $C_a(t)$ in this system can be very complex. However, since the measurements with hybrid spots for a constant analyte concentration (Fig. 3.10b,e) fit well with a single exponential function ($\varphi = e^{-C_{H2O2}kt}$, data not shown), C_{H2O2} remains constant in time. This indicates that the system quickly (in less than 1 min) reaches a steady state: enzymatically-produced H_2O_2 balances the diffused one. Therefore, at a given time t, C_{H2O2} only depends on C_a, not on the previous state of the system. We can write $C_{H2O2} = f(C_a)$ and, comparing the calibration curves $\Delta\varphi(C_a)$ of the hybrid spots with that of H_2O_2 taken from [233], I find that a second order polynomial expansion expresses the correlation $C_a = f^{-1}(C_{H2O2})$ very well:

$$C_a = f^{-1}(C_{H2O2}) = aC_{H2O2}^2 + bC_{H2O2} + d. \tag{3.10}$$

The resulting coefficients obtained from fitting the experimental data are summarized in Table 3.1, where both C_{H2O2} and C_a are expressed in micromolars. Higher order expansion terms are insignificant. Since Eqs. (3.7) and (3.10) establish a link between $\varphi(t)$ and $C_a(t)$, quantitative data for the analyte (lactose or glucose) concentration can now be obtained.

Let us emphasize that experiments performed with living organisms are often accompanied by an oxidative stress, leading to the production of H_2O_2 by the organisms under study. The multiplexed technique presented here becomes extremely handy in that case, as it makes possible isolating the oxidative stress-produced H_2O_2 from that produced enzymatically. Using a pair of sensing spots that measure: analyte + H_2O_2 (spot 1) or H_2O_2 (spot 2), I first use Eq. (3.7) to extract C_{H2O2} for both spots. Next, I subtract $C_{H2O2}(2)$ of the second spot from that of the first spot $C_{H2O2}(1)$. Finally, C_a can be calculated from Eq. (3.10) using the obtained difference $C_{H2O2}(1-2)$. This will be utilized in the next section to determine glucose uptake in aquatic microorganisms.

Table 3.1. Fitting coefficients for Eq. (3.10) of hybrid spots (only valid in the 0.1–1000 μM analyte range).

	0.1 U GOx	0.01 U GOx	2.5×10^{-3} U LOx	1.25×10^{-4} U LOx
a	-0.16	-1.13	-0.63	-1.66
b	2.24	2.55	2.43	2.51
d	-0.31	0.83	0.03	1.62

3.4.5 Uptake of exogenously supplied glucose

To study the uptake of glucose on the green alga *C. reinhardtii*, I inject a mixture of glucose and algae into the microfluidic chip. Once this mixture reaches the cell chamber, the flow is stopped for the time of the experiment. The multiplexed measurements are performed with two spots: a cyt *c* spot to detect the stress-related H_2O_2 and a hybrid spot (cyt *c* + GOx), which is sensitive to both glucose and H_2O_2. During the experiments, no H_2O_2 was detected (Fig. 3.13b and 3.13d), meaning that, first, algae are not stressed by the presence of glucose and, second, only glucose

oxidizes the hybrid spot. Using the approach developed in the previous section and the data in Table 3.1, the concentrations C_a in the solution for glucose (Fig. 3.13c) and for H_2O_2 can be obtained (Fig. 3.13d). Due to the uptake by algae, the glucose concentration drops from $8\,\mu M$ to $5\,\mu M$ within 1 h (Fig. 3.13c). Control experiments without algae revealed a stable glucose concentration in the cell chamber (green data in Fig. 3.13c). Comparing the external volume of the chamber $(10\,\mu l)$ with the internal volume of all algae in the experiment (approx. $0.07\,\mu l$), we obtain a 150:1 volume ratio. Therefore, *C. reinhardtii* internalize the equivalent of $450\,\mu M$ of glucose within 1 h. Since the latter concentration is much higher than the concentration in the solution, two possible scenarios can take place: (1) algae use active mechanism to uptake glucose; (2) once uptaken glucose is converted into CO_2, which reduces the glucose concentration in the algae. Most likely, both scenarios occur simultaneously. Actually, the measured glucose uptake is similar to blue algae *Aphanocapsa 6714* that can uptake as much as $500\,\mu M$ of glucose within one hour by converting it into CO_2 [212]. Overall, these experiments demonstrate the possibility of sensitive, multiplexed and continuous measurements, which can be further applied to more sophisticated mechanistic studies of cellular processes.
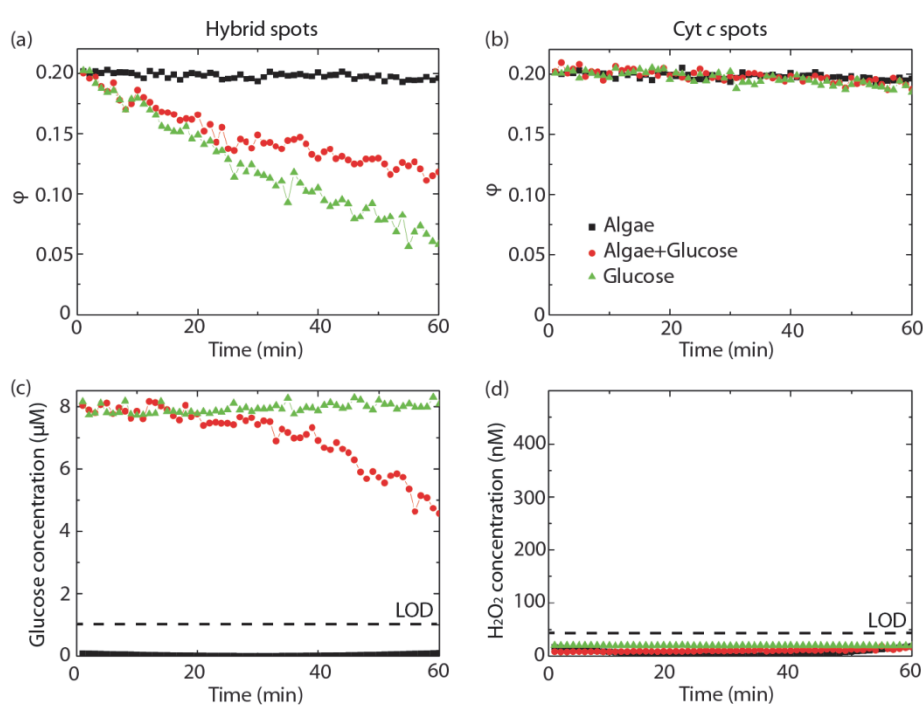
Figure 3.13. **Continuous multiplexed measurements of glucose and H_2O_2.** Glucose uptake $(8\,\mu M)$ and H_2O_2 release by *C. reinhardtii* $(2\times10^6$ cells/ml). Multiplexed measurements in microfluidics using (a) a hybrid spot with 20 pmol cyt c + 0.01 U GOx and (b) a spot with 20 pmol cyt c. Calculated concentrations of (c) glucose and (d) H_2O_2 using Eqs. (3.7) and (3.10). The same symbols are used for all panels.

3.5   Summary

A new portable device for the continuous measurement of the kinetics of oxidative stress was presented. By printing 20 pmol cyt c spots in a porous membrane containing 220 nm pores, the optical absorbance of cyt c is increased by a factor of 4.6 thanks to the elongation of the optical path. This configuration reaches a LOD of 40 nM for H_2O_2. The spots can be stored up to 10 days without losing their functionality. Moreover, they can be re-reduced and reused for at least 5 measurements. The POSS is easy to handle and shows a high reproducibility, which makes it a very well suited tool for the detection of H_2O_2 in the context of a broad variety of biological systems. Experimental results and numerical simulations show that the diffusion rate of H_2O_2 is faster than the chemical reaction rate between cyt c and H_2O_2. Additionally, by careful considerations on the reaction kinetics, I have derived an expression allowing the determination of H_2O_2 for time-dependent biological processes, whose validity was demonstrated by exposing *C. reinhardtii* cells to 180 nM Qdots and to 50 mg/l TiO_2 nanoparticles. Oxidative stress occurred in Qdots with continuously increasing H_2O_2 release (14 nM/min), starting after 5 min of exposure, while this was not observed in the case of TiO_2. Hence, POSS has the potential to shed new light on specific environmental questions in the field as well as in the laboratory [43].

I have further presented a new sensitive approach for the detection and the continuous monitoring of glucose and lactate. These two analytes are enzymatically converted into H_2O_2, which is, in turn, detected via the oxidation of cyt c. Such conversions take place locally thanks to the corresponding enzymes, which are incorporated in the sensing spot and fabricated by contact spotting technique in a very reliable and reproducible fashion. Extremely low LODs of 240 and 110 nM have been achieved for glucose and lactate, respectively. By integrating such sensing elements into a microfluidic chip, I was able to efficiently suppress crosstalk between different sensing spots. As demonstrated by the study of glucose uptake in such algae, the proposed method provides a non-invasive, label-free way to measure simultaneously in real-time the by-products of several cellular processes. Furthermore, such a biosensor is fast, cheap and easy to fabricate and could become a promising candidate for medical diagnostics and healthcare monitoring.

Chapter 4 Multi-layered microfluidic chip for ecotoxical studies on aquatic microorganisms

In this chapter, I introduce a multi-layered microfluidic chip with an integrated optical sensor for continuous sensitive detection of extracellular H_2O_2. This platform includes hydraulically controlled microvalves and microsieves, which enable the precise control of toxicants and allow complex exposure sequences. In particular, I use this platform to study the dynamics of toxicant-induced ROS generation in the green alga *Chlamydomonas reinhardtii* during short-term exposures, recovery periods and subsequent exposures. Two Cd-based toxicants with distinct internalization mechanisms are used as stress-inducers: CdSe/ZnS quantum dots (Qdots) and ionic Cd^{2+}. These results show quantitative dynamics of ROS, the recovery of cell homeostasis after stress events and the cumulative nature of two consecutive exposures to very low concentrations of toxicants. The dissolution of quantum dots and its possible influence on toxicity mechanisms and H_2O_2 depletion is discussed. The obtained insights are highly relevant from ecotoxicological, physiological and immunological perspectives.

4.1 Introduction

ROS are chemically reactive molecules containing activated oxygen. In the state of cellular homeostasis they are in a fragile equilibrium with antioxidants (AOX). ROS control different physiological processes including stress-responses, signalling and pathogen defense [2, 9, 10]. We can potentially advance physiological and medical research with a better understanding of ROS biology, their functions and dynamics [3, 12].

In this chapter, I concentrate on stress-response dynamics of ROS in aquatic microorganisms, which – besides its fundamental biological interest – is also highly relevant from ecotoxicological perspectives [34, 179]. Toxicants (e.g. trace metal ions and inorganic nanoparticles) and abiotic factors (e.g. variations in temperature, salinity, UV irradiation) may directly damage the cell or induce ROS generation, disrupting the cellular homeostasis [2, 3, 14]. As a consequence, imbalanced ROS (called oxidative stress) may lead to organelle and DNA damages and to cell death [179, 235]. Thus, the level of ROS provides information about the cell state, while the ROS production rate can predict further fate of the cell [3].

To date, common ROS-detecting techniques identify oxidative stress events, but are end-point and qualitative [223]. Rate and amount of ROS generation with respect to particular toxicants or abiotic factors remain unknown [43]. New insights have been obtained by recent works on continuous H_2O_2 sensing, which is one of the most stable ROS and can be quantified extracellularly [176, 177, 223]. For instance, algae exposed to ionic cadmium (Cd^{2+}) showed three distinct periods with different H_2O_2 production rates, demonstrating the complexity of cell response [176]. A major factor hindering further progress lies in the difficulty to perform continuous measurements with precisely dosed stress agents. This is especially problematic for aquatic microorganisms that cannot be anchored on a surface [236].

Microfluidic chips provide an elegant solution to this challenge. Indeed, besides precise control, other advantages of microfluidics include rapid analysis, miniaturization and high throughput – all highly relevant parameters for biological studies [237-244]. Platforms based on microfluidics have efficiently been used to manipulate living cells, as well as for cell culturing, spatially selective reagent delivery into cells, cell metabolism studies, drug screening and tissue engineering [245-250].

In this chapter, I develop a multi-layered microfluidic chip, including hydraulically controlled microvalves and sieves, to gain precise control over exposure of cells to toxicant. The combination of this chip with an integrated optical biosensor allows quantifying the dynamics and amounts of extracellular H_2O_2. In addition, the microfluidic chip allows running complex exposure sequences, which is, to my best knowledge, carried out for the first time in the context of ROS studies. In the performed experiments the green microalga *Chlamydomonas reinhardtii* served as a model microorganism. It is a native microorganism that grows in soil and fresh water environments around the globe [209, 251]. I studied the ecotoxicological effects on this alga of two Cd-based pollutants at low concentrations: CdSe/ZnS core-shell quantum dots (Qdots), which are widely used as fluorescent labels [210], and Cd^{2+}, which is highly toxic and known to induce oxidative stress in microalgae [235]. Qdots and Cd^{2+} have different sizes, different mechanisms of internalization and can induce different gene regulations [252, 253]. Thus, I expect distinct mechanisms and dynamics of ROS generation. I specifically choose appropriate Qdots and Cd^{2+} concentrations to stimulate the production of comparable amounts of ROS. Furthermore, intracellular ROS and membrane permeability levels supplement the extracellular measurements. This chapter provides new insights into ROS generation dynamics, toxicity potential and cell regeneration.

4.2   Methods

4.2.1   Chemicals

All solutions, including Cd^{2+} (Sigma Aldrich), Zn^{2+} (Sigma Aldrich), CdSe/ZnS Qdots (Life Technologies) or trypan blue 0.4% (Life Technologies) were freshly prepared from stocks with distilled water prior every experiment. Leached Qdots, used to investigate the effects of ionic dissolution, were prepared from the intermediate stock, which was

obtained by storing 40 nM Qdots in water for 2 days at 4°C. All experiments were per-performed in distilled water.

4.2.2 End-point procedures

Algae were prepared as described in the Chapter 3. Intracellular ROS evaluations are based on the intensity of the fluorescent signal stemming from intracellularly de-esterified CM-H$_2$DFCDA (chloromethyl dihydrodichlorofluorescein diacetate) reacting locally with generated ROS. Intracellular ROS measurements were carried out using cell samples (cell density of ca. 2×10^6 cells/ml) incubated with 20 μM CM-H$_2$DCFDA dye (Sigma Aldrich) for 30 min in the dark. Their fluorescent intensity was measured in a multi-well plate reader (Safire2, Tecan) at $\lambda = 525$ nm using an excitation wavelength at $\lambda = 495$ nm.

To assess the membrane permeability the samples were incubated with 12 μM Propidium Iodide dye (Sigma Aldrich) for 30 min in the dark. The fluorescent intensity at $\lambda = 617$ nm was measured using an excitation wavelength at $\lambda = 536$ nm. Positive controls were run by exposing the algae for 30 minutes to 10 mM H$_2$O$_2$ prior to the incubation with dyes.

To determine the amount of dissolved Cd^{2+} and Zn^{2+}, 3 ml of Qdots suspension (5 nM) were put in dialysis bags (1kDa Uptima H1-18-10, CelluSep) and immersed in 3 ml of distilled water.

ICP-MS was used for the quantitative differentiation between extracellular and cell-associated (i.e. the sum of intracellular amount and material sticking to the cell membrane) amounts of metallic elements. To determine the cell-associated Cd and Zn amounts, 10 ml of algae were rinsed and digested until the solution became colourless (0.2 ml of HNO$_3$ at 85 °C) prior to the ICP-MS analysis. Measured ICP-MS amounts were converted to concentrations.

4.2.3 Fabrication of microfluidics

All microfluidic layers (Fig 4.1a) were prepared from polydimethylsiloxane (PDMS) (10:1 ratio of PDMS/curing agent, if not stated otherwise) using casting technique. The corresponding molds were fabricated by standard photolithography in SU-8 photoresist (except the flow layer where AZ9260 photoresist was used). A spot layer (100 μm thickness) was deposited by spin-coating PDMS at 500 rpm for 40 s, followed by manual hole cutting to accommodate the sensing spot. The cell layer consisted of two layers of 40 μm and 1 mm thickness. The thick cell layer (1 mm thick with 300 μm thick channels) containing input channel (300 μm wide) and cell compartment (2 mm wide) was prepared by pouring the appropriate amount of PDMS onto the mold. The thin cell layer (40 μm thick with 10 μm thick channels) contains the same base-pattern with additional microsieve (5 μm period) and was deposited by spin-coating PDMS at 8000 rpm for 5 min (Fig. 4.1h,i). The flow (20:1 ratio) and control layer (5:1 ratio) had a thickness of 40 μm (spin-coating at 5000 rpm for 5 min) and 1 mm (pouring),

respectively. Both of these layers had 10 µm thick and 100 µm wide channels (Fig. 4.1d,e). After pouring the PDMS onto the molds all layers were prebaked for 30 min at 80 °C. The thick cell and control layers were tailored and separated from the molds. Subsequently, the thick cell layer was carefully aligned and placed onto the thin cell and the control layer – onto the flow layer and baked at 80 °C overnight. After the prebaking step the PDMS is not entirely cross-linked and, consequently, the subsequent full baking process strongly joins the layers lying on each other. After baking an additional thin PDMS layer was added on top of the cell layer (spin-coating at 5000 rpm for 3 min). The cell compartment was manually carved through both, thick and thin cell layers. The attached control and flow layers were aligned with respect to the cell layer and baked at 80 °C for 2 h with the freshly spin-coated PDMS layer serving as bonding material. Finally, the spot layer was placed on the microscope slide and baked at 80 °C overnight. Prior to the measurements a sensing spot was inserted into the opening in the spot layer. Then, the microfluidic chip was placed on top and the center of the channel, where the measurements take place, was carefully aligned with respect to the spot. At last, the entire system was clamped between two metallic plates with appropriate openings enabling the optical measurements.

4.2.4   Injecting and rinsing

All microfluidic operations were performed using a liquid pump (Xcalibur, Tecan) and controlled via Labview software. Prior to use, the microfluidic chip was rinsed with distilled water at a constant flow rate (2 mm/s). The integrated microfluidic valves operate according to the following principle: an increase of the channel pressure in the control layer (by applying a gentle flow of 0.1 mm/sec for 10 s) expands the channel, closing the corresponding cross-sections in the flow layer (Fig. 4.1b-i). The valves were held in the closed state while the algae suspension was carefully injected into the cell layer (0.5 mm/s) until they reached the cell compartment. Then, the flow in the cell layer was stopped.

In a preparatory step the analyte was introduced into the flow layer with the valve in the closed state (2 mm/s). Then, the valve was opened and the analyte was gently injected from the flow layer into the cell layer by applying the flow at both ends of the flow layer channels (0.1 mm/s for 3 s). After a time lapse of 50 s, to allow diffusion, the valve was closed and a new injection cycle started. Since the channels in the flow layer have a much smaller volume than the cell chamber, in order to efficiently inject analyte, I proceeded in the following manner: the injection cycle was repeated five times, the first three times by injecting an analyte concentrations 10x higher than the final concentration, followed by twice injections with the final analyte concentration.

To remove the analyte from the cell layer, the microfluidic valve was closed and a gentle flow of distilled water (0.2 mm/s, 1 min) was applied. Subsequently, a backward flow (0.2 mm/s, 3 s) was applied to help the cells spread out again into the cell compartment.

To exchange the sensing spots between two consecutive series of measurements, the algae were removed from the cell layer, the microfluidic chip was opened, the sensing

spot exchanged, the microfluidic chip closed and the algae were re-introduced. This procedure takes approximately 3 min.
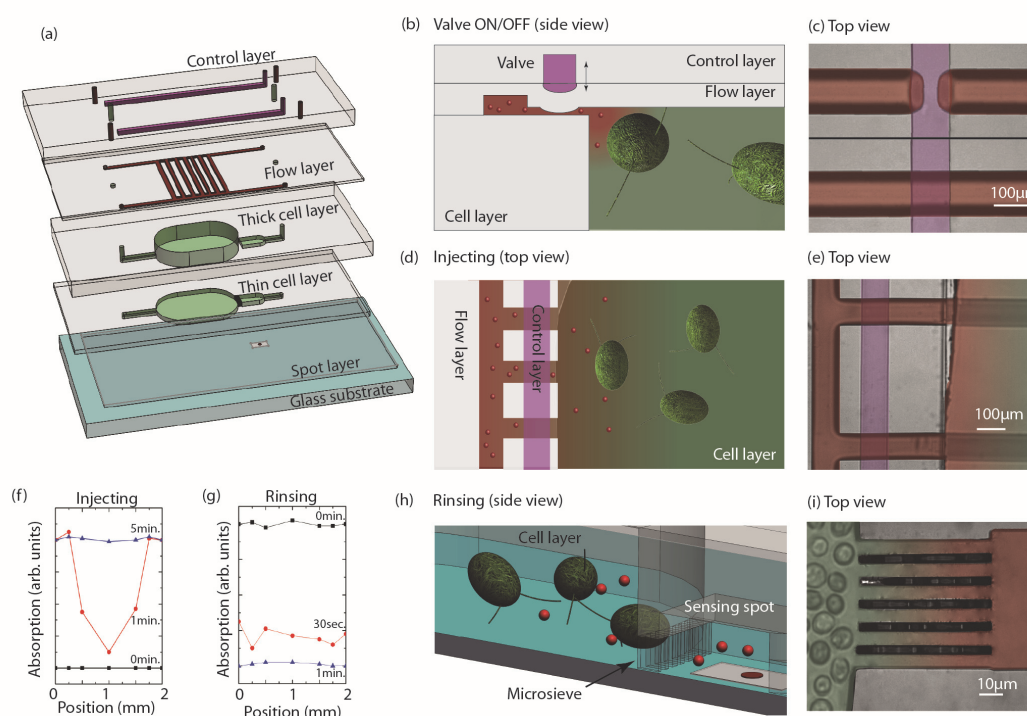
Figure 4.1. **Multi-layered microfluidic chip.** Schematic drawings (a,b,d,h) and microscope pictures (c,e,i) of the multi-layered microfluidic chip: (a) full chip configuration; (b,c) valve operation to manage the connection between the flow and cell layers; (d,e) injecting mode when toxicant enters into the cell layer; (h,i) rinsing mode when toxicant leaves the cell layer through the microsieve. Colours in the microscope images are artificial. The red spheres represent the toxicant and green ellipsoids the algae. Time evolution of trypan blue absorption (4 µM concentration in the flow layer) across the cell layer for (f) injecting and (g) rinsing.

4.3 Interaction between toxicants and algae

4.3.1 Microfluidic system

To gain precise control over the exposure of algae to toxicants, I designed and fabricated a microfluidic chip, which consists of five layers (Fig. 4.1a). The spot layer accommodates the sensing spot and guarantees optimal integration with the rest of the chip. The sensing spot lies in the proximity of the cell layer, so that H_2O_2 reaches the

spot sufficiently fast by diffusion, but is well-separated from the algae to exclude optical interference. The cell layer serves as a cell compartment during measurements (thick part) and contains a microsieve (thin layer), which retains the algae during rinsing (Fig. 4.1h,i). The toxicant enters the chip through the flow layer, which is connected to the cell layer (Fig. 4.1d,e). This connection is managed by microfluidic valves in the control layer (Fig. 4.1b,c).

To visualize the diffusion of the injection process in the cell layer, I injected $4\,\mu M$ of trypan blue dye into the flow layer according to the procedure described in the previous section. Absorption measurements indicate that the dye uniformly spreads across the cell layer within 5 min (Fig. 4.1f). Similarly, after 1 min rinsing, the dye is completely removed (Fig. 4.1g).

I further demonstrated efficient injection mechanisms by observing similar H_2O_2 responses from algae exposed to 500 nM Cd^{2+} through the injection in the microfluidic system and algae exposed to 500 nM Cd^{2+} prior to their introduction into the cell layer (Fig. 4.2a). Furthermore, algae exposed to 100 nM Cd^{2+}, which was washed away immediately after injection, showed no generation of H_2O_2, demonstrating the effectiveness of the rinsing procedure (Fig. 4.2b).
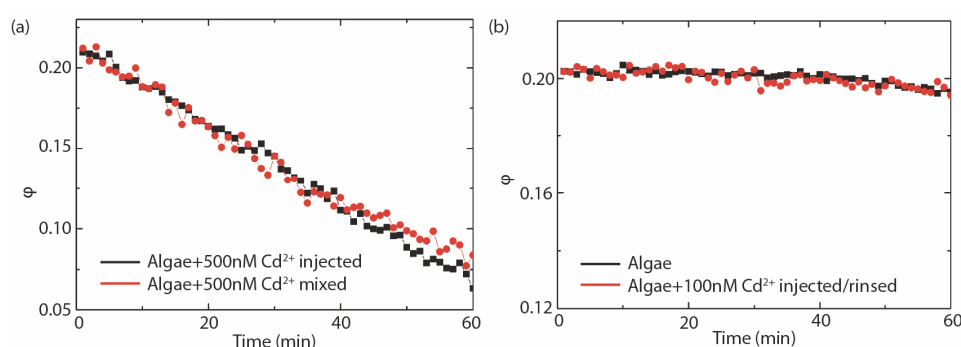
Figure 4.2. **Injection/rinsing experiments.** (a) Redox state coefficient φ for: algae mixed with 500 nM Cd^{2+} prior to their injection into the cell layer (red); and algae injected into the cell layer with 500 nM Cd^{2+} sequentially introduced (black). (b) Redox state coefficient φ for untreated algae and algae with 100 nM Cd^{2+} injected and rinsed immediately.

4.3.2   Exposure to Cd^{2+}

The microfluidic chip was used to control algae exposure to Cd^{2+}. Two different Cd^{2+} exposure levels were investigated: 100 nM and 500 nM. In parallel, extracellular H_2O_2 released from exposed algae was continuously measured using the sensing spot that

monitors the cyt c redox state as discussed in the previous chapter [176, 233]. Control experiments with unexposed algae did not show any H_2O_2 generation. Furthermore, differential measurements eliminate interference effects between Cd^{2+} and the cyt c sensing spot (Fig. 4.3).
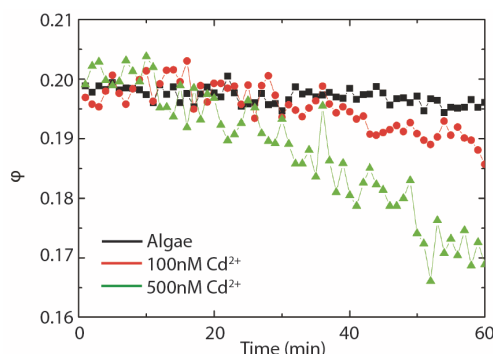
Figure 4.3. **Sensing spot interference with Cd^{2+}.** Redox state coefficient φ for untreated algae and Cd^{2+} showing a slight interference of Cd^{2+} with the sensing element.

When exposed to 500 nM of Cd^{2+}, algae rapidly produced H_2O_2: immediately after the injection I detected $C_{H2O2} = 80$ nM, which then increased to 150 nM after 60 min (1.2 nM/min), to 220 nM after 120 min (1.2 nM/min) and to 380 nM after 160 min (4.5 nM/min) (Fig. 4.4a,c, Table 4.1). The H_2O_2 production rates are estimated with linear fits. Injection procedure duration – in the order of 5 min – explains the non-zero C_{H2O2} at the beginning of the experiment. C_{H2O2} dropped to 100 nM when, after 60 min, the cell layer was rinsed to remove both, the produced H_2O_2 and injected Cd^{2+}. This level remained constant during the following 100 min. I refer to this type of experiment as post-stress experiments. When, after 60 min of post-stress, algae were re-exposed to 500 nM of Cd^{2+}, C_{H2O2} increased from 100 nM to 300 nM within 40 min (5.0 nM/min). Due to the strong oxidation of the cyt c sensing spots were exchanged after every hour of measurement. During the last 20 min of the experiment, φ nearly reached zero and couldn't be used for a reliable C_{H2O2} extraction; hence data stopped at $t = 160$ min in Figs. 4.4c and d. Finally, end-point intracellular ROS levels measured by fluorescence match the trends of extracellular H_2O_2 well (Fig. 4.4e).

When exposing algae to 100 nM of Cd^{2+}, C_{H2O2} slowly increased, reaching 70 nM after 60 min (1.1 nM/min), 130 nM after 120 min (1.0 nM/min) and 200 nM after 160 min (1.6 nM/min) (Fig. 4.4b,d). When algae were rinsed after 60 min, C_{H2O2} dropped to 40 nM and further decreased to zero within the following 60 min. When, after 60 min, algae were re-exposed with 100 nM of Cd^{2+}, C_{H2O2} increased from 20 nM to 110 nM within the next 40 min (2.3 nM/min). Changes in intracellular ROS levels became statistically significant only after an exposure over 3 h and show similar values for both,

post-stress and continuous exposures (Fig. 4.4f). Complementary membrane permea-permeability measurements revealed that the algae remained alive after 3 h of Cd^{2+} exposure (see Appendix F).
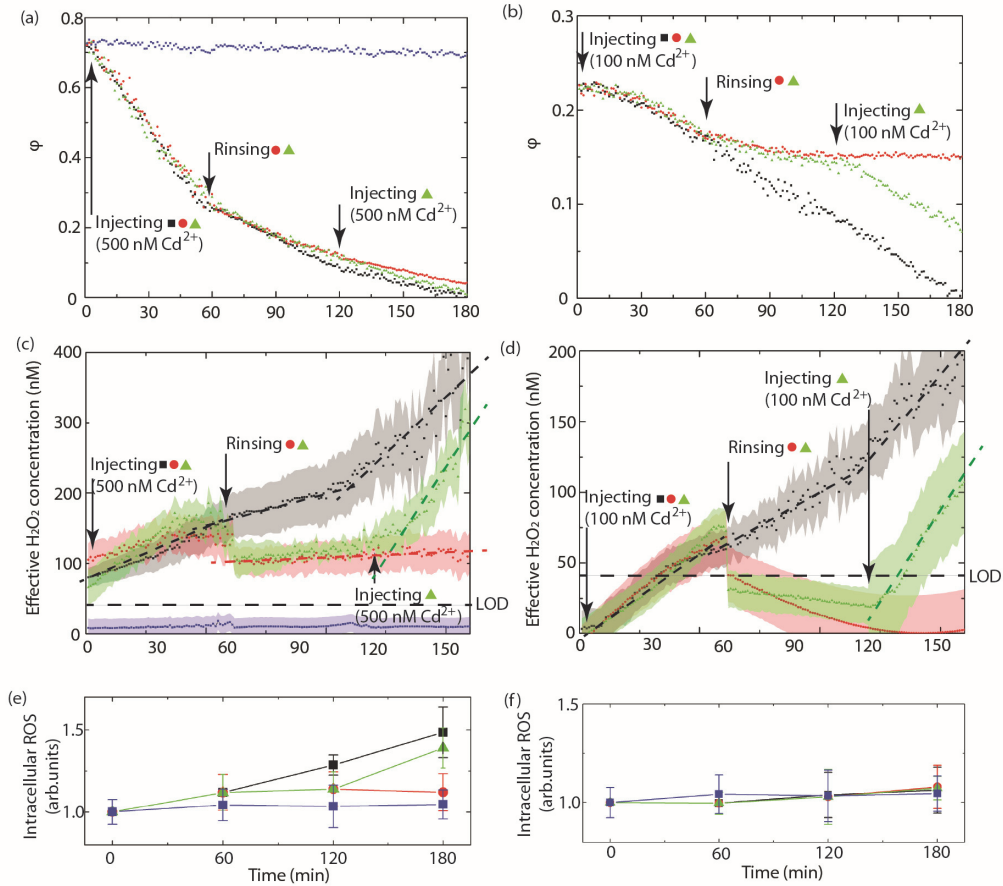
Figure 4.4. **Algae exposure to Cd^{2+}.** Time dependencies of redox state coefficient φ for: (a) 500 nM and (b) 100 nM exposure cycles. (c,d) Extracellular H_2O_2 concentration C_{H2O2} converted using Eq. (3.7). The shaded areas represent the standard deviation over 3 samples. The dashed curves are linear fits. Intracellular ROS for 500 nM (e) and 100 nM (f) Cd^{2+} exposures in identical cycles as in (a) and (b) (the same colors as in (a) are used, blue corresponds to unexposed algae). Error bars represent standard deviation over 9 samples. Tukey multiple comparisons of means are available in Appendix F.

4.3.3 Exposure to Qdots

Similarly to Cd^{2+}, I exposed algae to CdSe/ZnS Qdots using the microfluidic chip for continuous measurements of the production of extracellular H_2O_2. Control experiments with 5 and 20 nM of Qdots showed no interaction with the cyt c sensing spot (Fig. 4.5a). Algae exposed to 5 nM, respectively 20 nM, Qdots generated H_2O_2 concentrations com-comparable to Cd^{2+}, reaching C_{H2O2} = 75 nM, respectively 100 nM, after 60 min exposure time (Fig. 4.5a,b). In contrast to the Cd^{2+} exposures, I observed an induction period (10 min, respectively 30 min, for 20 nM, respectively 5 nM, of Qdots). When exposed to 5 nM of leached Qdots, algae generate H_2O_2 at faster rate reaching C_{H2O2} = 150 nM within 1 h and shorter induction period (approx. 20 min) as compared to an exposure to 5 nM of fresh Qdots. To explain the difference between the experiments performed with fresh and leached Qdots, I measured the total (27.5 µM of Cd and 13.8 µM of Zn, corresponding to 5 nM of Qdots) and the dissolved amounts of Cd^{2+} and Zn^{2+} in the dispersion by ICP-MS. In the absence of the algae, only minute quantities of Cd^{2+} and Zn^{2+} (10 nM and 150 nM, respectively) are present in the 3 h-old Qdot dispersion (Fig. 4.5g). In contrast, the 2 day-old Qdots release 20 nM of Cd^{2+} and 13 µM of Zn^{2+}, indicating the total dissolution of the ZnS-shell, while the CdSe-core remains mostly intact. Additional experiments were performed, exposing algae to 13 µM of Zn^{2+} leading to a production by the algae of 60 nM H_2O_2 within 1 h; on the other hand, exposure to 1 µM Zn^{2+} did not induce any measurable response (Figs. 4.5c and d).

A different behaviour was observed for longer exposure times. For instance, exposing the algae for 120 min to 5 nM Qdots, C_{H2O2} started to decrease after 90 min and, finally, dropped to the limit of detection (green curves in Figs. 4.5e and f). In the post-stress case, the C_{H2O2} values were below the detection limit (black curves in Figs. 4.5e and f). ICP-MS measurements of the cell-associated elements revealed 300 nM Cd^{2+} and 1.15 µM Zn^{2+}, after 2 h exposure to 5 nM Qdots (Fig. 4.5h). On the other end, the corresponding intracellular ROS levels increased with time, including in the post-stress case (Fig. 4.5i).

4.4 ROS dynamics

4.4.1 Intracellular ROS and extracellular H_2O_2

Under steady state conditions, AOX scavenge ROS in biological systems [2]. If cell homeostasis is disturbed, for example in this chapter by the presence of Cd^{2+}, unbalanced ROS spread around the cell, damaging nucleic acids, oxidizing proteins and causing lipid peroxidation [254]. Due to their short lifetime (in the order of microseconds), ROS also can transform into their most stable representative, which is H_2O_2 [177]. Unbalanced H_2O_2 is excreted through the cell membrane. Thus, the concentration of extracellular H_2O_2 depends on the concentration of overproduced ROS. Indeed, during the exposure to Cd^{2+}, H_2O_2 was found outside algae, indicating a stress event [233]. As a result, continuous extracellular H_2O_2 measurements complement end-point intracellular ROS levels, measuring the overproduced ROS.
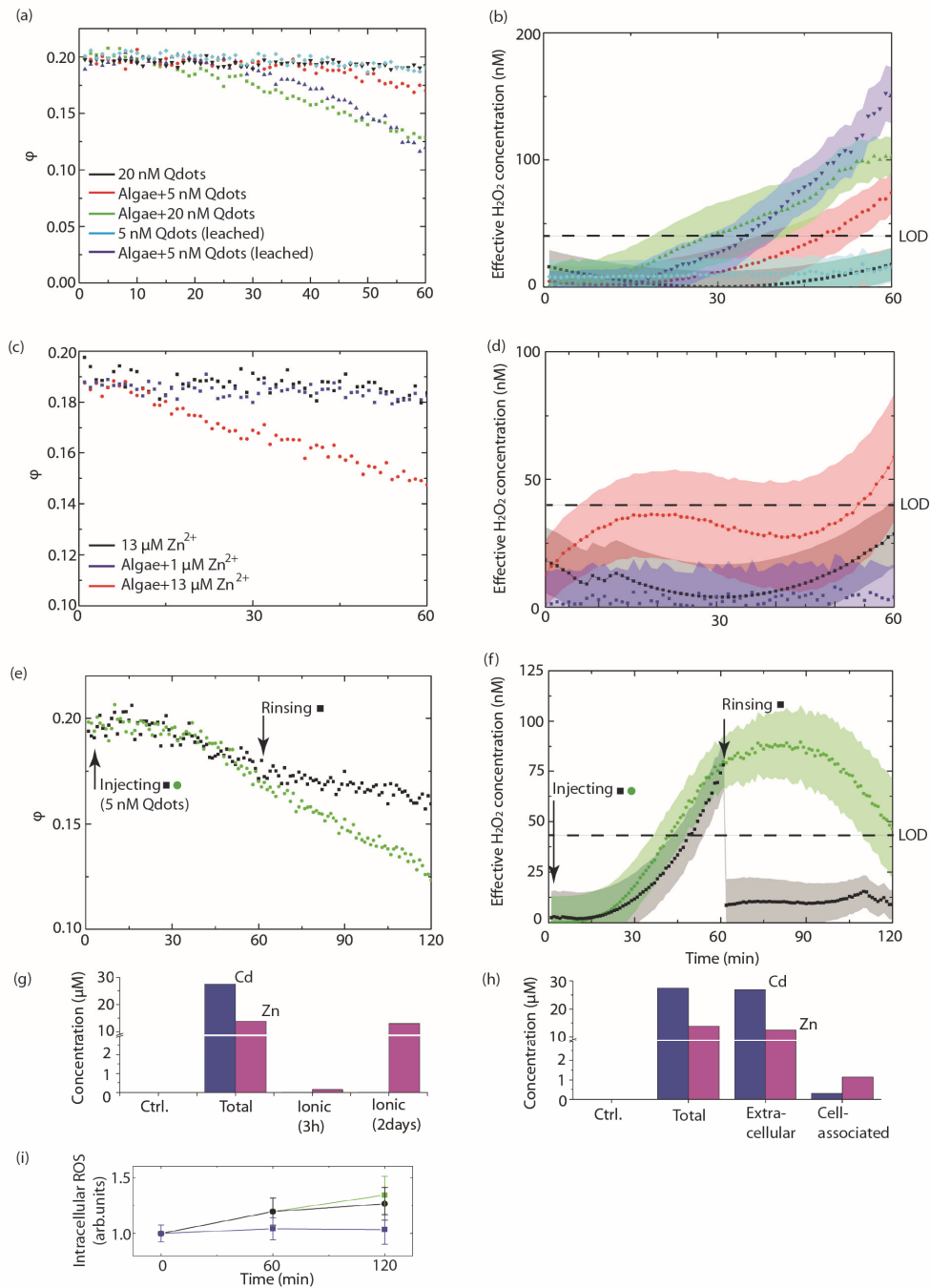
Figure 4.5. **Algae exposure to Qdots.** (a) Time dependencies of redox state coefficient φ when exposed to 5 nM, 20 nM and 5 nM leached Qdots in the presence and absence of algae. (b) Extracellular H_2O_2 concentration C_{H2O2} converted using Eq.(3.7). (c,d)

Exposure to Zn^{2+}. (e,f) Exposure to 5 nM Qdots. The shaded areas represent the standard deviation over 3 samples. (g) ICP-MS measurements for total and dissolved Cd and Zn of 5 nM of Qdots. (h) ICP-MS measurements of extracellular and cell-associated Cd and Zn after a 2 h-exposure of algae to 5 nM Qdots. (i) Intracellular ROS of 5 nM Qdots exposures for identical cycles as in (e) (the same colors as in (a) are used, blue corresponds to unexposed algae). The error bars represent the standard deviation over 9 samples. Tukey multiple comparisons of means are available in Appendix F.

4.4.2 H_2O_2 excretion

I found that the exposure of algae to Cd^{2+} induces continuous H_2O_2 release during 1 h (black curves in Fig. 4.4c,d). Due to both active uptake and concentration gradient, i.e. diffusion, Cd^{2+} penetrates into the algae within minutes and stimulates ROS generation [255]. Consequently, the concentration of ROS exceeds that of AOX and oxidative stress sets in [255, 256]. This is reflected by elevated intracellular ROS (Fig 4.4e) and extracellular H_2O_2 levels (Fig. 4.4c) when the algae are exposed to 500 nM of Cd^{2+}. At a lower concentration of Cd^{2+} (100 nM) intracellular ROS levels do not rise (Fig. 4.4f), even though algae excrete H_2O_2 (Fig. 4.4d). This indicates that excretion of intracellular ROS in the form of H_2O_2 represents a pathway for maintaining stable intracellular ROS levels. However, the capability of such excretion has to be limited. Indeed, at elevated stress (exposure to 500 nM of Cd^{2+} in this chapter), the algae probably cannot efficiently excrete all overproduced intracellular ROS, which is reflected by elevated intracellular ROS levels.

Table 4.1. Extracellular C_{H2O2} rates (in nM/min) for Cd^{2+} exposures to algae.

Exposure	Hour	500 nM Cd^{2+}	100 nM Cd^{2+}
1st	1st	1.2	1.1
	2nd	1.2	1.0
	3rd	4.0	1.6
2nd	1st	5.0	2.3

There are several hierarchical levels of oxidative stress [19]. During the first 2 h of Cd^{2+} exposure, C_{H2O2} increases with a similar rate, but longer exposure results in an increased release rate (Fig. 4.4c and Table 4.1). At this point, algae probably enter in a new phase of oxidative stress with inflammation mechanisms taking over the antioxidants defence [19].

In order to measure the post-stress behaviour, both extracellular Cd^{2+} and H_2O_2 were removed after 1 h from the microfluidic chip as described above. Thus, when the microfluidic chip – containing algae treated with 100 nM Cd^{2+} – is rinsed, the extracellular C_{H2O2} drops below the detection limit (red curve in Fig. 4.4d). In the case of

500 nM Cd^{2+} exposure, I observed a drop in C_{H2O2} to 100 nM (red curve in Fig. 4.4c). These non-zero values of C_{H2O2} are associated with elevated intracellular ROS levels: the algae continue to excrete H_2O_2 during the washing period (~5 min) (Fig. 4.4c-f). This indicates that the H_2O_2 concentration gradient over the cell wall – created during the rinsing step – sustains the excretion. After a rapid jump during the rinsing step, both extracellular H_2O_2 and intracellular ROS concentrations remain stable. These results suggest that algae have the ability to re-establish rapidly the ROS/AOX balance.

A consecutive exposure to the same concentration of Cd^{2+} shows higher C_{H2O2} generation rates (green curves in Fig. 4.4c,d) with respect to the first exposure (Table 4.1). Thus, I observed that the rate and extent of ROS generation depend, even at low Cd^{2+} concentrations, not only on the given toxicant exposure but also on previous events. This effect can be associated with bioaccumulation of intracellular Cd^{2+} [253]. Once inside the algae, Cd^{2+} can substitute other ions like Ca^{2+}, Cu^{2+} and Zn^{2+}, disrupting cellular functions [176, 257].

4.4.3 Qdots-induced oxidative stress

Both intracellular ROS and extracellular C_{H2O2} levels increase within the first hour of CdSe/ZnS Qdots exposure to algae as displayed in Fig. 4.5b and f. The increase of ROS can be attributed to cell-associated Cd and Zn (Fig. 4.5h). However, ICP-MS measurements detect the total amount of Cd and Zn present in a sample and, therefore, this technique does not discriminate between dissolved ionic and metallic elements in the form of Qdots. I attempted imaging experiments in order to detect the fluorescent Qdots inside the algae, but obtained no conclusive results because the fluorescence of algae overlaps with that of Qdots (data not shown). As indicated by ICP-MS, pristine Qdots have a 2:1 concentration ratio of Cd and Zn (Fig. 4.5g). Since only 300 nM of cell-associated Cd was detected, the upper limit of 150 nM for Zn in the form of Qdots can be estimated and, in turn, more than 1 µM must be in the ionic form (Fig. 4.5h). This corresponds to a 6-fold higher amount of dissolved Zn^{2+} in the presence of algae as compared to pure water, which was earlier attributed to the change of the pH level in the vicinity of algae [252, 253, 258, 259]. Control experiments with such quantities of Zn^{2+} did not induce any extracellular H_2O_2 (Fig. 4.5d). Therefore, elevated ROS and C_{H2O2} levels – observed in Qdots exposure – are mediated via cell-associated Qdots/Cd^{2+}.

If the Qdots exposure to algae is extended, C_{H2O2} stops to increase during the second hour and even decreases towards the end of the experiment (green curve in Fig. 4.5f). The latter effect might be connected with CdSe/ZnS Qdots converting H_2O_2 into water [260-263]. Moreover, this conversion can be much more efficient after dissolution of the ZnS shell. Indeed, one of the functions of Zn-shell in Qdots is to remove electron-hole traps at the surface of the Cd-core [264] and to confine the excited electrons in the core of Qdots [210]. However, as discussed above, cell-associated Qdots are characterized by enhanced dissolution. Keeping this in mind, I proposed the following scenario: once the ZnS shell forfeits its sealing capability, Cd^{2+} leaches into the algae and triggers oxidative stress, leading to an increase of intracellular ROS levels (Fig. 4.5i). The presence of the induction time (Fig. 4.5f), which was not observed in the Cd^{2+} experiments, further

supports this toxicity mechanism. Concurrently, after the CdSe core is stripped, an en-enhanced depletion of H_2O_2 sets in as discussed above. Comparing 500 nM Cd^{2+} and Qdots exposures, they both stimulate increased intracellular ROS. However, in contrast to 500 nM Cd^{2+}, C_{H2O2} is well below the detection limit (black curve in Fig. 4.5f) in the post-stress after Qdots exposure. This further strengthens the presumption that Qdots deplete H_2O_2. As a result, measured H_2O_2 concentrations in Qdots experiments are underestimated since H_2O_2 is partly destroyed.

4.5　　Summary

I have presented a multi-layered microfluidic chip combined with an integrated optical biosensor for sensitive and continuous detection of extracellular H_2O_2. The microfluidic chip includes microfluidic valves and microsieves to design complex exposure sequences. Furthermore, continuous measurements give access to the dynamics of biological processes, which represents a very significant advantage compared with frequently used end-point assays. With this setup, I measured the H_2O_2 response of the green algae *Chlamydomonas reinhardtii* exposed to Cd^{2+} and CdSe/ZnS Qdots. In addition, intracellular ROS levels were measured and the dissolution of the Qdots was quantified by ICP-MS.

Using the proposed microfluidic configuration, I found that algae are able to recover their homeostasis after 60 min oxidative stress induced by Cd^{2+}. Furthermore, consecutive exposures induce enhanced H_2O_2 generation. CdSe/ZnS Qdots induce ROS generation in algae mainly due to the cell-associated Cd, whereas the effect of Zn is negligible. It is not entirely clear in which state (ionic or particulate) the Cd reacts with algae, but I confirmed an enhanced dissolution of Cd and Zn from Qdots in the presence of algae. Furthermore, in case of Qdots exposure, I observed an induction time for the H_2O_2 release as compared to the Cd^{2+} experiments, leading to the presumption of Qdot dissolution prior to H_2O_2 generation. Finally, a decrease in extracellular H_2O_2 concentration was observed after 90 min exposure to 5 nM of Qdots, which I explained as H_2O_2 depletion through electron traps available on the surface of the Qdots with deteriorated shells. Overall, to my best knowledge, experiments with such complex exposure patterns at such low concentrations of toxicants are presented for the first time. Of course, further investigations are necessary to elucidate the impact of Cd^{2+} and core/shell Qdots on living organisms. However, I demonstrated that this microfluidic platform opens the door for a completely new type of experiments, leading to a better understanding of ROS biology as well as for ecotoxicological studies.

Chapter 5   Conclusion and outlook

P er aspera ad astra – a Latin phrase that translates as "through hardships to the stars" – best describes this thesis in several ways: it gives the feeling about the tremendous importance of the topic discussed here; it shows the extensive distance between the start and the finish; and it describes the bumpy road that I have undertaken to reach the thesis objectives. For instance, the thesis starts with Fig. 2.1, which describes the basic principle of multiscattering, a phenomenon proposed to use to create new optical probes. The story goes on through physics, engineering and finally reaching biology in Fig. 4.5, where the actual extracellular H_2O_2 concentration is measured in biological systems using the developed optical probe. Although, the latter result constitutes the main objective of the thesis and unites all chapters, every chapter is self-consistent having its own motivation and novel developments.

5.1   Achieved results

The first achievement of this thesis is multiscattering enhanced absorption spectroscopy (MEAS). Based on light propagation in random media, I have developed a simple yet effective extension of the standard absorption spectroscopy. Without any additional equipment, MEAS provides an enhancement of limit of detection for a variety of analytes, including commercially available H_2O_2 bioassays as well as 10 nm gold nanoparticles acting as colorimetric probes. Besides experiments, I have also implemented a numerical model that fits well with the obtained results and provides an additional handle to engineer OPL enhancement according to the application at hand. Due to its simplicity, MEAS is a promising new alternative to absorption spectroscopy to detect analytes in small concentrations.

Next, I demonstrated that the absorbed light energy in the medium has a non-monotonic dependence in the presence of random media with various filling factors: a random medium with a critical filling factor can increase the absorbed energy by 2.4. If an open photonic cavity is added, even a larger enhancement is obtained (23-fold). Historically, the presence of scatterers in conventional cavities was viewed as a drawback, decreasing the quality factor of the latter. However, 3D open photonic cavity and random medium can act symbiotically: for certain configurations the performances of this hybrid system can be better as the cavity or the random medium alone. To demonstrate the potential of maximal absorption, I numerically showed that such a hybrid system can improve the performance of light trapping for solar cell applications. Overall, Chapter 2 opens new perspectives for sensing and energy harvesting applications using random media.

The next significant innovation is the portable oxidative stress sensor (POSS): I used a multiscattering-enhanced approach to improve the capabilities of the optical detection for biosensing applications and assembled from scratch a portable setup to accommodate the developed multiscattering-enhanced optical probes. Out of three different techniques, microarray spotting proved to be the best approach to spot nanoliters of cyt c in the porous membrane. Such optical probes demonstrate excellent repeatability and reproducibility, while the multiscattering enhancement scheme permits a 40 nM LOD for H_2O_2 – low enough to trace processes at cellular level. These multiscattering-enhanced optical probes were further developed to continuously detect glucose and lactate, achieving 110 and 240 nM limits of detection, respectively, which are at least one order of magnitude lower than the current state of the art. In summary, Chapter 3 documents the development and proof of concept experiments for multiscattering-enhanced optical probes, which represents an extremely appealing alternative for continuous extracellular H_2O_2 measurements.

The last chapter introduces a novel multi-layered microfluidic chip with an integrated multiscattering-enhanced optical probe. This sophisticated system also includes hydraulically controlled microvalves and microsieves to design complex exposure sequences of toxicants to aquatic microorganisms. In particular, I found that *Chlamydomonas reinhardtii* exposed to ionic Cd can excrete H_2O_2 without increasing the intracellular ROS levels. Additionally, I have observed that algae have the ability to recover their homeostasis after Cd^{2+} exposure. Consecutive exposures show enhanced H_2O_2 generation rate, indicating cellular damages. This study represents only the first example in the field unveils the tremendous possibilities and complicated toxicant sequences, which can be applied using the developed microfluidic chip. In conclusion, this system opens the door for new insights in ROS dynamics and its function in cells, as well as for assessing the toxicity mechanisms of nanomaterials.

5.2   Future developments

5.2.1 Multiscattering-enhanced optical probes in an open photonic cavity

The numerically demonstrated maximal absorption in a random medium can be utilized for sensitive probes. In particular, multiscattering-enhanced optical probes could be improved using an open cavity (Fig. 5.1). Sensing in random media relies on collecting transmitted light with elongated optical paths. As was demonstrated in Chapter 2, in such a configuration most of light is lost: high OPL amplification factors come at the cost of low output intensity, which in turn often requires expensive light sources and detectors [83]. In this context, an open cavity with one opening represents an interesting alternative, since almost all the escaping light can be collected. Furthermore, I have demonstrated that up to 99% of energy can be absorbed in the hybrid system of an open cavity with a random medium. Therefore, such a configuration represents a promising platform for biosensing.

5.2.2 Porous substrates with higher refractive indices

In this thesis, I have used commercially available porous membranes with two different pore sizes. This approach can be further extended: refractive index and pore size are two possible parameters to be optimized. Preliminary results with ZrO_2 (n=2.3) and TiO_2 (n=2.6) porous films (fabricated in EMPA, Dübendorf) have demonstrated enhancement factors f of 8 and 16, respectively (recall that for the porous membranes in Chapter 3, f is 4.6). There are, however, several difficulties that must be addressed to use these materials, especially in terms of membrane robustness and wetting, so that the sensing spot can penetrate into the material.

5.2.3 Other sensing molecules

The demonstrated multianalyte detection scheme can be further extended to numerous other enzymes (for example, cholesterol oxidase, glycerol-3-phosphate oxidase and uricase [196]) that convert different substrates into H_2O_2. Furthermore, the sensing molecule cyt c can be substituted with other molecules. In particular, porphyrins – the general class of compounds to which the heme group of cyt c belongs– are of special interest because, for many of them, their absorption spectrum changes with their redox state, like for cyt c (for example, hemoglobin [265]). Similarly, ion-ligand complexes can be used for the sensitive detection of different ions [266].
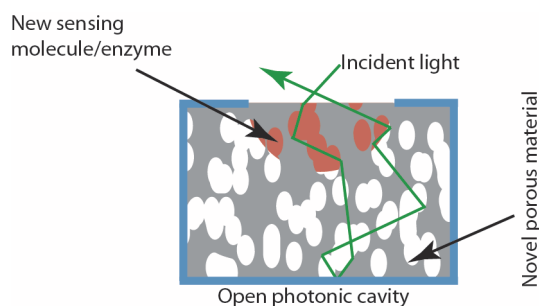
Figure 5.1. **Multiscattering-optical probe** made of a new sensing molecule/enzyme combination in an open cavity filled with novel porous materials. This picture summarizes the developments suggested in Sec. 5.2.1-5.2.3.

5.2.4 Spatial H_2O_2 measurements

Besides temporal H_2O_2 measurements, the developed platform can be directly extended for performing spatial measurements, where several optical probes detect H_2O_2 in different places simultaneously. Furthermore, preliminary experiments indicate that spatial measurements can be performed even within one single sensing spot (Fig. 5.2).

This opens the possibility to study biological processes not only in time, but also with a high spatial resolution.
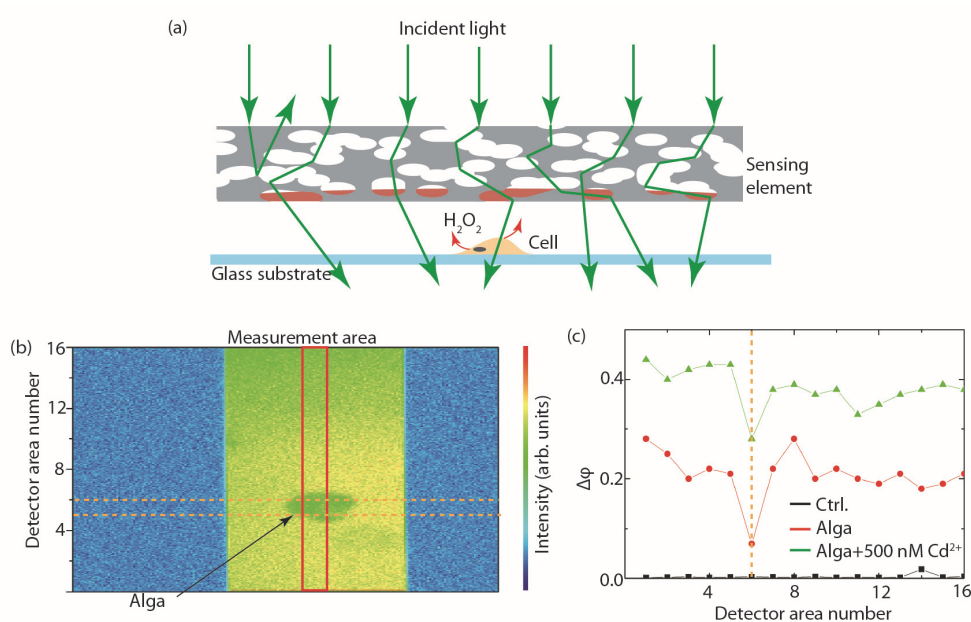
Figure 5.2. **Spatial H$_2$O$_2$ sensing.** (a) Schematic of the measurement configuration: the sensing spot is placed in the proximity of a cell. The generated H$_2$O$_2$ mostly reacts with the closest area of the spot. The optical signal is then collected from different areas on the spot. (b) Imaging a single alga on the CCD as in Chapter 3. The red box represents the measurement area, which is divided into 16 equal areas. The dashed orange lines indicate the 6th detector area where most of the alga is located. For spectral measurements the setup is refocused on the sensing element instead of the alga. The alga was immobilized on the surface using vacuum grease. (c) Change of the redox coefficient $\Delta\varphi$ after 1 h for control measurements in water, alga and alga in the presence of 500 nM Cd^{2+}. The dashed orange line indicates the detector area where most of the alga is located for both measurements.

5.3   Potential impact for ROS biology

5.3.1   Mechanisms

The exact mechanisms that trigger ROS generation as well as how the magnitude and the duration of ROS production determine their specific functions remain unclear [3]. In this context, the multiscattering-enhanced optical probes for continuous H$_2$O$_2$ measurements that I have developed enable dynamic measurements, which can

provide new mechanistic information. Although I have concentrated on stress-induced ROS in aquatic microorganisms in this thesis, the developed biosensors can be used for other types of biological entities, including various cell lines and living organisms.

5.3.2 Medical advances

Many drugs partly work by generating ROS, by inducing intracellular ROS generation, by diminishing cellular ROS production or by increasing catabolism of ROS [8, 267-269]. For example, many antibiotics kill bacteria by inducing them to generate ROS [8, 270]. A better understanding of how antibiotics lead to ROS production as part of their action mechanism could help revitalize antibiotic research and discovery. Moreover, some anticancer agents such as adriamycin [271] and bleomycin [272] produce ROS directly. Therefore, advances in ROS biology have potential to develop completely different treatments for many diseases, including cancer. Finally, ageing is determined by cellular metabolism, which in turn can be controlled through harnessing ROS levels [14].

5.3.3 Impact on nanotoxicology

The rapid growth of nanotechnology is increasing the likelihood of ENMs coming into contact with humans or the environment [33]. The organic and synthetic worlds merge into a new science concerned with the safe use of nanotechnology [43]. In this thesis, I have presented a multi-layered microfluidic chip that allows studying the interaction between ENMs and living entities. Complex exposure sequences of toxicants in conjunction with continuous ROS measurements will lead to a better understanding of the 'nano-bio' interface in general and the stress-related ROS dynamics in particular. Overall, this platform can be used for food, water and air quality controls in relation with ENMs. For example, novel monitoring methods could be based on measuring the ROS generation in microorganisms dispersed in different environments throughout a country.

A. Abbreviations

Table A.1. Table of used abbreviations.

Abbreviation	Full name
AA	Ascorbic acid
AOX	Antioxidants
CM-H$_2$DCFDA	Chloromethyl dihydrodichlorofluorescein diacetate
Cyt c	Cytochrome c
DMEM	Dulbecco's modified Eagle's medium
ENM	Engineered nanomaterial
GOx	Glucose oxidase
HRP	Horseradish peroxidase
H$_2$O$_2$	Hydrogen peroxide
ICP-MS	Inductively coupled plasma mass spectrometry
LOD	Limit of detection
LOx	Lactate oxidase
MEAS	Multiscattering-enhanced absorption spectroscopy
NA	Numerical aperture
OPL	Optical path of light
PBS	Phosphate buffered saline
PI	Propidium Iodide
POSS	Portable oxidative stress sensor
PS	Polystyrene
Qdots	Quantum dots
ROS	Reactive oxygen species
TAP	Tris-acetate phosphate

B. Raw spectra examples for MEAS measurements
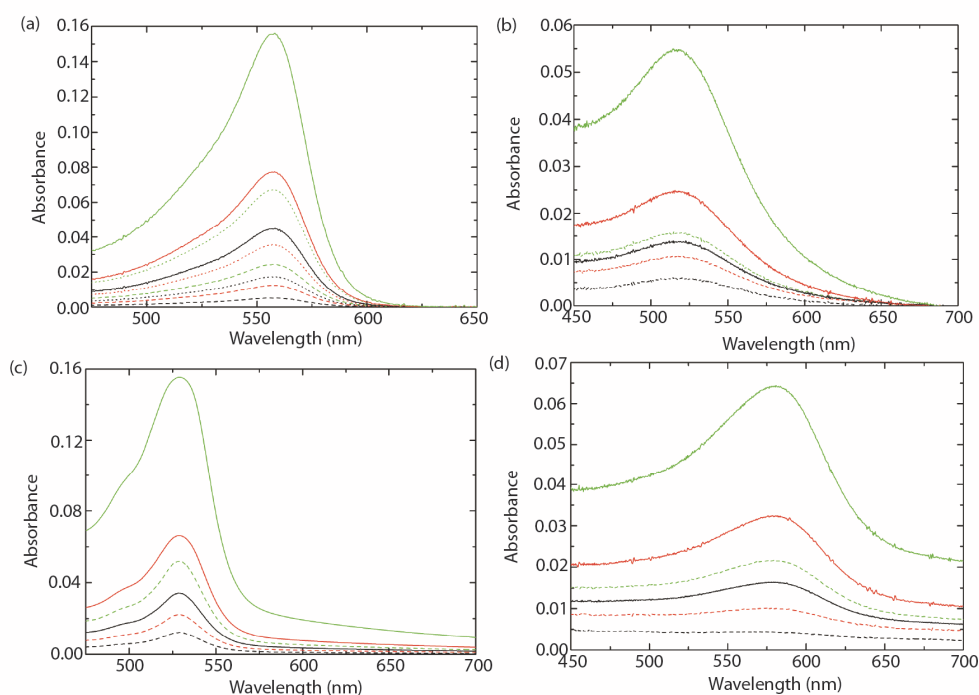
Figure B.1. **Absorbance measurements** for: (a) phenol red (black curves – 0.1 μM, red 0.2 μM and green 0.4 μM) in water (dashed lines) and in water/PS beads mixtures (dots for C_1^{PS} and full lines for C_2^{PS}). The same measurement configuration as in Fig. 2.3a is used. (b) 10 nm gold nanoparticles (black curves – 7.3 μM, red 14.6 μM and green 29.2 μM) in water (dashed lines) and in water/PS beads. The same measurement configuration as in Fig. 2.3b is used. (c) Envy green (black curves – 25 mg/l, red 50 mg/l and green 100 mg/l) in water (dashed lines) and in water/PS beads. The same measurement configuration as in Fig. 2.3c is used. (d) Bioassay (black curves – 4 μM, red 10 μM and green 20 μM) in water (dashed curves) and in water/PS beads. The same measurement configuration as in Fig. 2.4b is used.
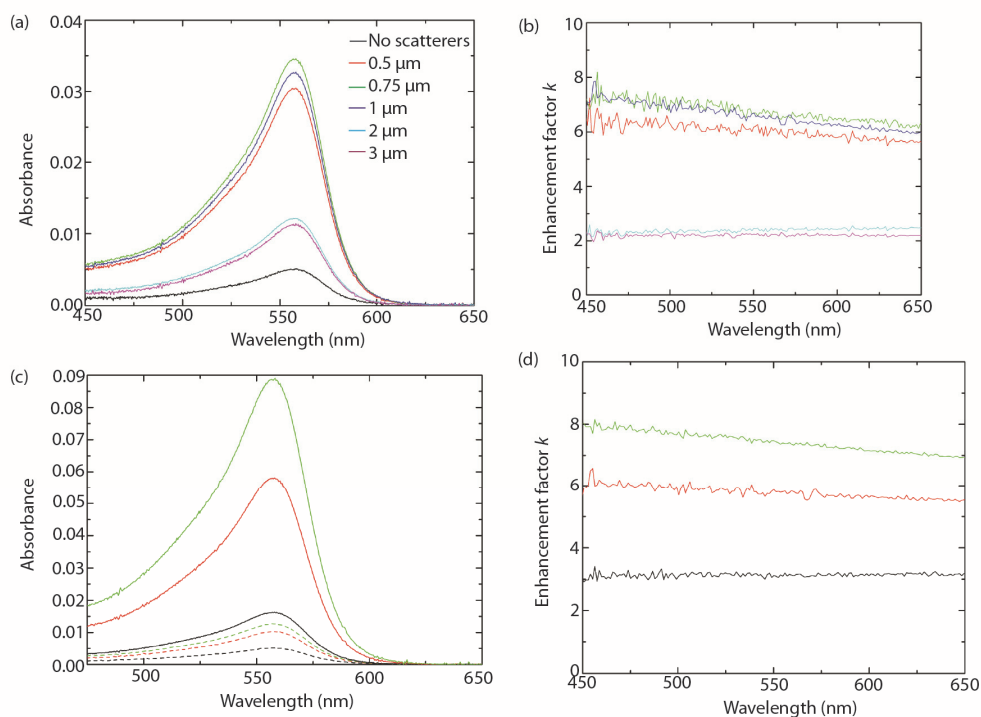
Figure B.2. **Spectral dependence of MEAS.** (a) Absorption measurements of phenol red in water and in water/PS beads of different diameters. The same measurement configuration as in Fig. 2.6b is used. (b) Spectral dependence of the enhancement factor k for (a). (c) Absorption measurements of phenol red in water (dashed curves) and in water/PS beads for different thicknesses L (black curves – 4 mm, red 8 mm and green 10 mm). The same measurement configuration as in Fig. 2.6c is used. (d) Spectral dependence of the enhancement factor k for (c).

C. Control software for microfluidic pump

Figure C.1. **Software interface** to control the microfluidic pump (see Chapter 3) implemented in Labview. The user has to select the number of cycles and set different parameters, such as speed, input/output ports of the pump and amount of injected liquid.

Figure C.2. **Block diagram** of the code presented in Fig. C.1, which contains function "1", which sends multiple commands to the microfluidic pump via RS-232 interface.
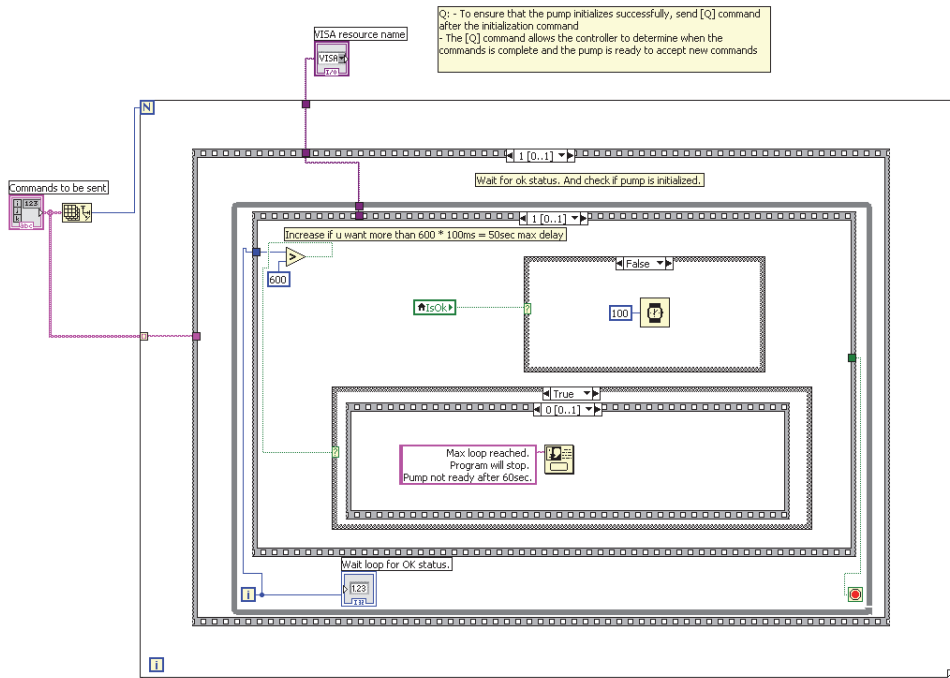
Figure C.3. **True-true cycle of the block diagram** for function "1" as described in Fig. C.2.
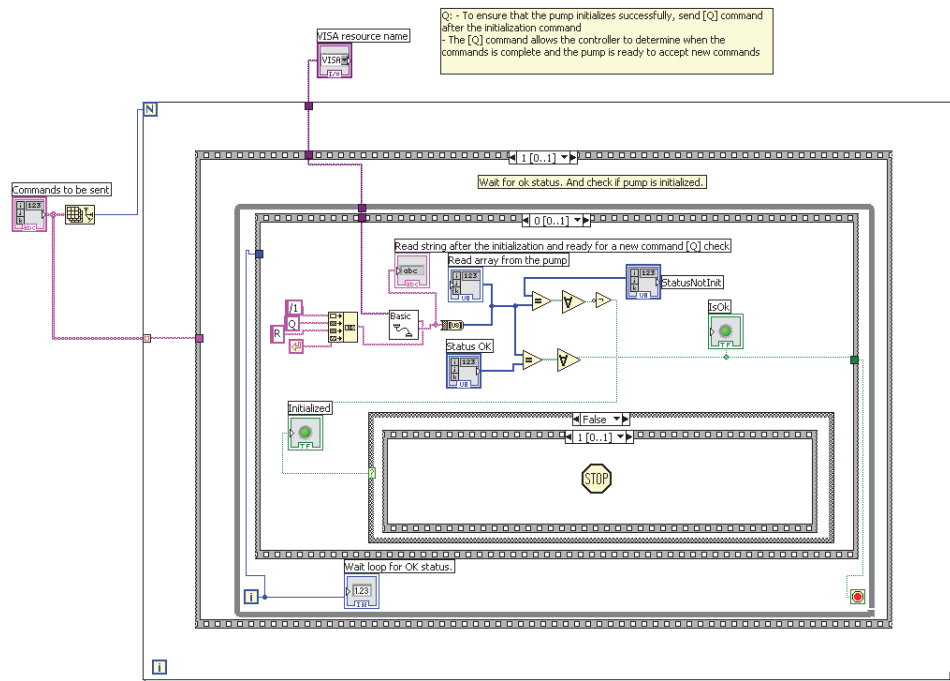
Figure C.4. **True-false cycle of the block diagram** of function "1" as described in Fig. C.2.
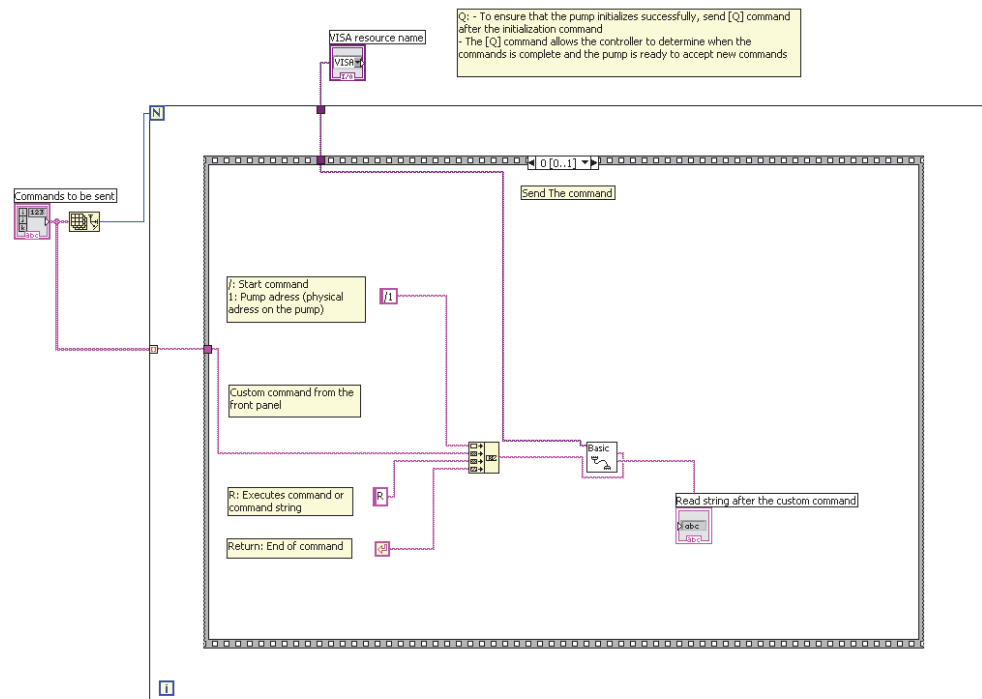
Figure C.5. **False cycle of the block diagram** of function "1" as described in Fig. C.2.

D. Code to calculate normalized redox coefficient

The Matlab code to calculate normalized redox coefficient used in Chapters 3 and 4:

```matlab
clear all;
clc
path='C:\backup\ROS detection\14_12_16\';
addpath(path);

no_data_m=[8];
acqui_m=[61];
time_step_m=[1];
no_lamp=[9];                    %indicate lamp for every data

col_m=['r','b']
shape_m=['o' 'o']
t=0;
t_m=[];coeffplot_m=[];coeffplot2_m=[];coeffplot3_m=[];

for oo=1:length(no_data_m)
    oo
    clear data_tmp2 spec_expt spec_expt_norm;
    no=no_data_m(oo);
    acqui=acqui_m(oo);
    data_tmp2=dlmread(['Data',num2str(no),'Datad',num2str(no),'.dat']);
    [len,wid]=size(data_tmp2)
    nq=no_lamp(oo);
    data_tmp=dlmread(['Data',num2str(nq),'Datad',num2str(nq),'.dat']);
    lam_m=data_tmp(:,1);
     spec_lamp=data_tmp(:,2);

    for ii=1:acqui
        spec_expt(:,ii)=data_tmp2(:,ii*2);
    end;

    for pp=1:acqui
        spec_expt_norm(:,pp)=spec_expt(:,pp)./spec_lamp;
  spec_expt_norm(:,pp)=spec_expt_norm(:,pp)./ (sum(spec_expt_norm(831:1:835,pp))/5
        t=t+time_step_m(oo);
        t_m=[t_m t];

        I1=sum(spec_expt_norm(486:1:490,pp))/5;
        I2=sum(spec_expt_norm(543:1:547,pp))/5;
        a1=9.9;          %542 nm
        a2=7.9;          %556 nm

    min=1000;
    pos=0;
    for i=1:1000
    k(i)=0.3+0.7*0.001*i;
    x(i)=abs( log((I1-(1-k(i)))/k(i))/log((I2-(1-k(i)))/k(i)) - (a1/a2) );
```

```
    if x(i)<min
        min=x(i);
        pos=k(i);
    end;
    end;

        kk=1*1+0*pos
        spec_expt_norm(:,pp)=(spec_expt_norm(:,pp)-(1-kk))./kk;
    end;
    figure(1)
    plot(lam_m,spec_expt_norm,'-o','MarkerSize',2)
    hold on;
    coeffplot=log( sum(spec_expt_norm(511:1:515,:))/5 ) ./ log(
sum(spec_expt_norm(486:1:490,:))/5 );

    coeffplot=(coeffplot-9.1/9.9)/(27.6/9.9-9.1/9.9);
coeffplot_m=[coeffplot_m coeffplot];
end
    figure(2)
b=transpose (coeffplot);
    plot(t_m,coeffplot_m,'o-','MarkerSize',3)
    hold on;
    xlabel('t (min)')
    ylabel('\phi (a.u.)')
```

E. Code for Monte Carlo simulations of light propagation in a random medium

The Matlab Monte Carlo code for light propagation in a random medium used in Chapter 2:

```
clc
clear;

%write file
file=['aaameasurement2.txt'];
dlmwrite(file,'');
     for cout=1:14
       cc=[1e-4,5e-4,1e-3,0.003,0.005,0.01,0.05,0.1,0.5,1,2,5,7,10];

C=500;                    %concentration of cytC
fr=0.5;                     %fraction of reduced cytC

%geometry of the individual particle
a=500e-9/2;                  %radius of PS beads, default=500/2 nm
th=0e-9;                     %thickness of the outer cytC layer, default=153nm
b=a+th;
nouter=1.3;              %outer refractive index of surrounding media,default=1

%concentration
NN=cc(cout)*3.64*1e11/1e-6; %number of PS beads from Polysciences
FF=NN*4/3*pi*b^3;           %fraction volume of scatterers

nstep=180;                            %number of angle steps
dteta=1/nstep;      %cos teta step
dteta0=180/nstep;    %angle step
for step=1:100000
    DisEv(step)=0;
    RefEv(step)=0;
    sum9(step)=0;
    sumRef9(step)=0;
end;

%geometry of the PS/cytc drop
Lx=500e-6;
Ly=500e-6;          %photons launched at Lx/2,Ly/2,0.  for 100 drops 640x640x21 um
Lz=500e-6;          %1000x1000x1000 um box
a0=100e-6;           %opening size in the top and bottom

%calculation of mie scattering. uses miecoated function
for i=550:1:550
    lam=i*1e-9;
    m1 = 2.60/nouter;  %data for polystyrene beads from polysciences, default=1.60
```

```
    lamq=lam*1e6;
    m2 = sqrt( epsCc(lamq, C, fr) )/nouter;     %lam in microns, concentration,
fraction
    alpha2=4*pi*imag(m2)/lam;
    x=2*pi*a/lam;
    y=2*pi*b/lam;
    if a==0
        result=mie2(m2^2,1,y);
    elseif th==0
        result=mie2(m1^2,1,x);
    else
        result=miecoated(m1,m2,x,y,u);
    end;
    qsca=result(1,2);                                 %scattering q
    asy=result(1,5);                                  %average cos theta
    lfree=4*b/((1-asy)*3*FF*qsca);           %mean free path

end;
%% energy box
Etotal=1;          %total energy is 1W*1sec

StartWav=400;      %start wav in nm
EndWav=600;        %end wav in nm
StepWav=0.5;       %step in nm
Steps=(EndWav-StartWav)/StepWav;
Ewav=Etotal/Steps;       %energy per 1 wavelength
Packets=1e4;                     %number of packets
Ewav0=Ewav/Packets;             %energy of 1 packet
StopEnergyFactor=1e12;      %after which energy to stop the beam (default=1e12),NA
any more

for lam=550:1:550


    lam

    %% propagation box

    sum0=0;
    sumRef=0;

    sum2=0;
    sumRef2=0;
    sum3=0;
    sumRef3=0;
    sum4=0;
    sumRef4=0;
    sum5=0;
    sumRef5=0;

    sumb0=0;
    sumbRef=0;

    sumb2=0;
    sumbRef2=0;
    sumb3=0;
    sumbRef3=0;
    sumb4=0;
    sumbRef4=0;
    sumb5=0;
    sumbRef5=0;

    ltot=0;
    Ndetect=0;
```

```matlab
    for i=1:Packets
        i/Packets*100
        j=1;

        x=Lx/2;
        y=Ly/2;
        z=1e-10;
        E=Ewav0;            %energy of the packet
        Eref=Ewav0;
        scat=0;
        refl=0;

%         while (E>(Ewav0/StopEnergyFactor))&(x>0)&(x<Lx)&(y>0)&(y<Ly)&(z>=0)&(z<Lz)
          while (x>0)&(x<Lx)&(y>0)&(y<Ly)&(z>0)&(z<Lz)
            if j~=1 scat=scat+1; end;
            fi=2*pi*rand;           %azimuth angle 0..2pi

            if j==1             %first direction is into the box
                theta=0*pi/10;       %dark-field configuration with pi/4=45deg.
incident angle
%               fi=0;
            else
                theta0=acos(1/(2*asy)*(1+asy^2-((1-asy^2)/(1+asy*(2*rand-1)))^2));
                theta=acos(cos(theta)*cos(theta0)+sin(theta)*sin(theta0)*cos(fi));
            end;

                p=-lfree*log(rand);
%                 L(i)=L(i)+p;
                cor=10;

                %reflection
                while cor>0
                cor=10;
                thetaold=theta;
                fiold=fi;
                Rmin=100;

                %side reflections
                R(1)=-x/(sin(thetaold)*cos(fiold));
                if (R(1)<p)&(R(1)>0)&(R(1)<Rmin) Rmin=R(1); cor=1; fi=pi-fiold;
theta=thetaold; end;
                R(2)=(Lx-x)/(sin(thetaold)*cos(fiold));
                if (R(2)<p)&(R(2)>0)&(R(2)<Rmin) Rmin=R(2); cor=2;  fi=pi-fiold;
theta=thetaold; end;
                R(3)=-y/(sin(thetaold)*sin(fiold));
                if (R(3)<p)&(R(3)>0)&(R(3)<Rmin) Rmin=R(3); cor=3; fi=2*pi-fiold;
theta=thetaold; end;
                R(4)=(Ly-y)/(sin(thetaold)*sin(fiold));
                if (R(4)<p)&(R(4)>0)&(R(4)<Rmin) Rmin=R(4); cor=4; fi=2*pi-fiold;
theta=thetaold; end;

                %top bottom reflection with openings
                R(5)=-z/cos(thetaold);
                if (R(5)<p)&(R(5)>0)&(R(5)<Rmin) Rmin=R(5); cor=5; theta=pi-
thetaold; fi=fiold; end;
                R(6)=(Lz-z)/cos(thetaold);
                if (R(6)<p)&(R(6)>0)&(R(6)<Rmin) Rmin=R(6); cor=6; theta=pi-
thetaold; fi=fiold; end;


                if cor<10
                x=x+R(cor)*sin(thetaold)*cos(fiold);
                y=y+R(cor)*sin(thetaold)*sin(fiold);
                z=z+R(cor)*cos(thetaold);
                E=E*exp(-alpha2*R(cor));
```

```matlab
                p=p-R(cor);
                j=j+1;
                refl=refl+1;

                if cor==1 x=0; end;
                if cor==2 x=Lx; end;
                if cor==3 y=0; end;
                if cor==4 y=Ly; end;
                 if cor==5 z=0; end;
                if cor==6 z=Lz; end;

                %1hole conditoin!!!
    if (cor>4)&(x>((Lx-a0)/2))&(x<((Lx+a0)/2))&(y>((Ly-a0)/2))&(y<((Ly+a0)/2))
%                if cor>0
                theta=thetaold;
                fi=fiold;
                cor=0;
                p=0;
                end;

                else cor=0;
                end;
                end;

                x=x+p*sin(theta)*cos(fi);
                y=y+p*sin(theta)*sin(fi);
                z=z+p*cos(theta);
                E=E*exp(-alpha2*p);
                j=j+1;


        end;



        if (theta<(pi/10))       %!!!DETECTION CONDITION: only light which is
transmitted through and angle pi/10=18deg.
            Ndetect=Ndetect+1;
            sum0=sum0+E*exp(+alpha2*(z-Lz)/cos(theta));
            sumRef=sumRef+Eref;



        end;



        if (theta<(pi/5))        %!!!DETECTION CONDITION: only light which is
transmitted through and angle pi/10=18deg.
            sum2=sum2+E*exp(+alpha2*(z-Lz)/cos(theta));
            sumRef2=sumRef2+Eref;

        end;

        if (theta<(pi/4))        %!!!DETECTION CONDITION: only light which is
transmitted through and angle pi/10=18deg.
            sum3=sum3+E*exp(+alpha2*(z-Lz)/cos(theta));
            sumRef3=sumRef3+Eref;

        end;

        if (theta<(pi/3))        %!!!DETECTION CONDITION: only light which is
transmitted through and angle pi/10=18deg.
            sum4=sum4+E*exp(+alpha2*(z-Lz)/cos(theta));
            sumRef4=sumRef4+Eref;
```

```matlab
        end;

        if (theta<(pi/2))       %!!!DETECTION CONDITION: only light which is
transmitted through and angle pi/10=18deg.
            sum5=sum5+E;
            sumRef5=sumRef5+Eref;

        end;

% backreflection
    if (theta>(9*pi/10))       %!!!DETECTION CONDITION: only light which is
transmitted through and angle pi/10=18deg.

            sumb0=sumb0+E*exp(+alpha2*(z-0)/cos(theta));
            sumbRef=sumbRef+Eref;
    end;

        if (theta>(4*pi/5))       %!!!DETECTION CONDITION: only light which is
transmitted through and angle pi/10=18deg.
            sumb2=sumb2+E*exp(+alpha2*(z-0)/cos(theta));
            sumbRef2=sumbRef2+Eref;

        end;

        if (theta>(3*pi/4))        %!!!DETECTION CONDITION: only light which is
transmitted through and angle pi/10=18deg.
            sumb3=sumb3+E*exp(+alpha2*(z-0)/cos(theta));
            sumbRef3=sumbRef3+Eref;

        end;

        if (theta>(2*pi/3))        %!!!DETECTION CONDITION: only light which is
transmitted through and angle pi/10=18deg.
            sumb4=sumb4+E*exp(+alpha2*(z-0)/cos(theta));
            sumbRef4=sumbRef4+Eref;

        end;

        if (theta>(pi/2))        %!!!DETECTION CONDITION: only light which is
transmitted through and angle pi/10=18deg.
            sumb5=sumb5+E;
            sumbRef5=sumbRef5+Eref;

        end;
%end of backreflection
    end;

    lave0=-log(sum0/sumRef)/alpha2; %length of light path

    lave5=-log(sum5/sumRef5)/alpha2;


    dlmwrite(file,[num2str(cc(cout)),' ',num2str(sumRef5),' ',num2str(sum5),'
',num2str(lave5)],'-append','delimiter','');

    laveb5=-log(sumb5/sumbRef5)/alpha2;

    dlmwrite(file,[num2str(cc(cout)),' ',num2str(sumbRef5),' ',num2str(sumb5),'
',num2str(laveb5)],'-append','delimiter','');
end;
    end;
```

F. Statistical analysis of intracellular ROS and membrane permeability levels
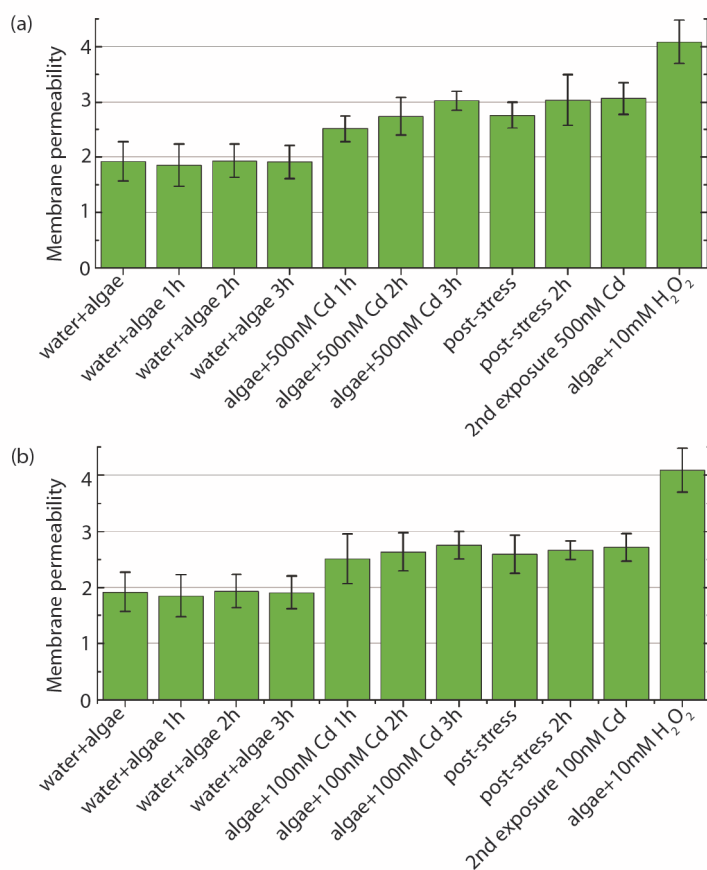
Figure F.1. **Membrane permeability levels** for (a) 500 nM and (b) 100 nM Cd^{2+} exposures as in Figure 4.4. Tukey multiple comparisons of means are available in Tables F.4 and F.5.
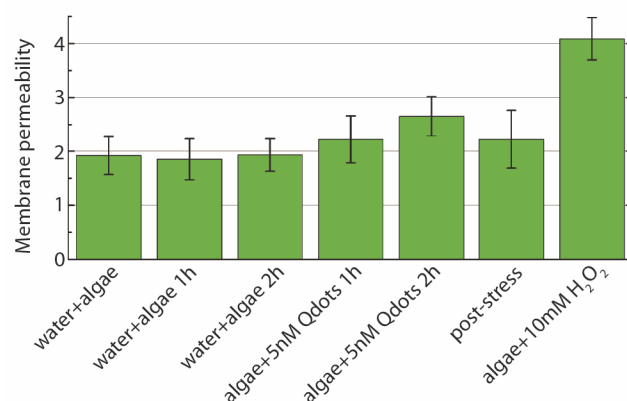
Figure F.2. **Membrane permeability levels** for 5 nM Qdots exposures as in Figure 4.5. Tukey multiple comparisons of means are available in Table F.6.

Tukey multiple comparisons of means

Significant codes *** p<0.01, ** p<0.05, * p<0.1, ~ p>0.1. For all tables data represents the average over 9 measurements.

Table F.1. Intracellular ROS levels (500 nM Cd^{2+} exposure).

	1	2	3	4	5	6	7	8	9	10	11
1) algae+water		*	~	*	***	***	***	***	***	***	***
2) algae+water (1h)			~	~	**	***	***	***	**	***	***
3) algae+water (2h)				~	***	***	***	***	**	***	***
4) algae+water (3h)					**	***	***	***	**	***	***
5) algae+500 nM Cd^{2+} (1h)						***	***	~	~	***	***
6) algae+500 nM Cd^{2+} (2h)							***	~	~	***	***
7) algae+500 nM Cd^{2+} (3h)								~	~	~	***
8) post-stress									~	***	***
9) post-stress 2h										***	***
10) 2nd exposure 500 Cd^{2+}											***
11) algae+10 mM H_2O_2											

96

Table F.2. Intracellular ROS levels (100 nM Cd^{2+} exposure).

	1	2	3	4	5	6	7	8	9	10	11
1) algae+water		*	~	*	~	~	*	~	**	***	***
2) algae+water (1h)			~	~	~	~	~	~	~	*	***
3) algae+water (2h)				~	~	~	~	~	~	**	***
4) algae+water (3h)					~	~	~	~	~	*	***
5) algae+100 nM Cd^{2+} (1h)						~	**	~	**	***	***
6) algae+100 nM Cd^{2+} (2h)							~	~	~	**	***
7) algae+100 nM Cd^{2+} (3h)								~	~	~	***
8) post-stress									*	**	***
9) post-stress 2h										~	***
10) 2nd exposure 100 Cd^{2+}											***
11) algae+10 mM H_2O_2											

Table F.3. Intracellular ROS levels (5 nM Qdots exposures).

	1	2	3	4	5	6	7
1)algae+water		*	~	***	***	***	***
2) algae+water (1h)			~	***	***	***	***
3) algae+water (2h)				***	***	***	***
4) algae+5nM Qdots 1h					***	*	***
5) algae+5nM Qdots 2h						~	***
6) post stress							***
7) algae+10mM H_2O_2							

Table F.4. Membrane permeability levels (500 nM Cd^{2+} exposures).

	1	2	3	4	5	6	7	8	9	10	11
1) algae+water		~	~	~	***	***	***	***	***	***	***
2) algae+water (1h)			~	~	***	***	***	***	***	***	***
3) algae+water (2h)				~	***	***	***	***	***	***	***
4) algae+water (3h)					***	***	***	***	***	***	***
5) algae+500 nM Cd^{2+} (1h)						**	***	***	***	***	***
6) algae+500 nM Cd^{2+} (2h)							***	~	**	***	***
7) algae+500 nM Cd^{2+} (3h)								~	~	~	***
8) post-stress									**	***	***
9) post-stress 2h										~	***
10) 2nd exposure 500 Cd^{2+}											***
11) algae+10 mM H_2O_2											

Table F.5. Membrane permeability levels (100 nM Cd^{2+} exposures).

	1	2	3	4	5	6	7	8	9	10	11
1) algae+water		~	~	~	***	***	***	***	***	***	***
2) algae+water (1h)			~	~	***	***	***	***	***	***	***
3) algae+water (2h)				~	***	***	***	***	***	***	***
4) algae+water (3h)					***	***	***	***	***	***	***
5) algae+100 nM Cd^{2+} (1h)						~	***	~	***	***	***
6) algae+100 nM Cd^{2+} (2h)							*	~	~	~	***
7) algae+100 nM Cd^{2+} (3h)								~	~	~	***
8) post-stress									~	*	***
9) post-stress 2h										~	***
10) 2nd exposure 100 Cd^{2+}											***
11) algae+10 mM H_2O_2											

Table F.6. Membrane permeability levels (5 nM Qdots exposures).

	1	2	3	4	5	6	7
1)algae+water		~	~	**	***	**	***
2) algae+water (1h)			~	***	***	**	***
3) algae+water (2h)				**	**	*	***
4) algae+5nM Qdots 1h					***	~	***
5) algae+5nM Qdots 2h						~	***
6) post stress							***
7) algae+10mM H_2O_2							

Bibliography

1.   B. Halliwell, "Reactive Species and Antioxidants. Redox Biology Is a Fundamental Theme of Aerobic Life," Plant Physiology **141**, 312-322 (2006).
2.   S. S. Gill and N. Tuteja, "Reactive oxygen species and antioxidant machinery in abiotic stress tolerance in crop plants," Plant Physiology and Biochemistry **48**, 909-930 (2010).
3.   C. Nathan and A. Cunningham-Bussel, "Beyond oxidative stress: an immunologist's guide to reactive oxygen species," Nature Review Immunollogy **13**, 349-361 (2013).
4.   L. A. del Río, L. M. Sandalio, F. J. Corpas, J. M. Palma, and J. B. Barroso, "Reactive Oxygen Species and Reactive Nitrogen Species in Peroxisomes. Production, Scavenging, and Role in Cell Signaling," Plant Physiology **141**, 330-335 (2006).
5.   N. Navrot, N. Rouhier, E. Gelhaye, and J.-P. Jacquot, "Reactive oxygen species generation and antioxidant systems in plant mitochondria," Physiologia Plantarum **129**, 185-195 (2007).
6.   O. Warburg, "Beobachtungen uber die Oxydationsprozesse im Seeigelei," Journal Physiological Chemistry **57**, 1-16 (1908).
7.   C. A. Foerder, S. J. Klebanoff, and B. M. Shapiro, "Hydrogen peroxide production, chemiluminescence, and the respiratory burst of fertilization: Interrelated events in early sea urchin development," Proceedings of the National Academy of Sciences **75**, 3183-3187 (1978).
8.   M. A. Kohanski, D. J. Dwyer, B. Hayete, C. A. Lawrence, and J. J. Collins, "A Common Mechanism of Cellular Death Induced by Bactericidal Antibiotics," Cell **130**, 797-810 (2007).
9.   K. Apel and H. Hirt, "Reactive oxygen species: Metabolism, Oxidative Stress, and Signal Transduction," Annual Review of Plant Biology **55**, 373-399 (2004).
10.   B. P. Yu, "Cellular defenses against damage from reactive oxygen species,", **74**, 139-162 (1994).
11.   H. Sies, "Oxidative stress: oxidants and antioxidants," Experimental Physiology **82**, 291-295 (1997).
12.   C. Gorrini, I. S. Harris, and T. W. Mak, "Modulation of oxidative stress as an anticancer strategy," Nature Review Drug Discovery **12**, 931-947 (2013).
13.   J. D. Lambeth, "NOX enzymes and the biology of reactive oxygen," Nature Review Immunollogy **4**, 181-189 (2004).
14.   T. Finkel and N. J. Holbrook, "Oxidants, oxidative stress and the biology of ageing," Nature **408**, 239-247 (2000).
15.   O. H. Petersen, A. Spät, and A. Verkhratsky, "Introduction: reactive oxygen species in health and disease," **360**, 2197-2199 (2005).
16.   A. A. Alfadda and R. M. Sallam, "Reactive Oxygen Species in Health and Disease," Journal of Biomedicine and Biotechnology **212**, 14 (2012).

17. M. Fransen, M. Nordgren, B. Wang, and O. Apanasets, "Role of peroxisomes in ROS/RNS-metabolism: Implications for human disease," Biochimica et Biophysica Acta (BBA) - Molecular Basis of Disease **1822**, 1363-1373 (2012).

18. W. Gwinner and H. J. Gröne, "Role of reactive oxygen species in glomerulonephritis," Nephrology Dialysis Transplantation **15**, 1127-1132 (2000).

19. A. Nel, T. Xia, L. Mädler, and N. Li, "Toxic Potential of Materials at the Nanolevel," Science **311**, 622-627 (2006).

20. M. R. Wiesner, G. V. Lowry, P. Alvarez, D. Dionysiou, and P. Biswas, "Assessing the Risks of Manufactured Nanomaterials," Environmental Science & Technology **40**, 4336-4345 (2006).

21. N. M. Franklin, N. J. Rogers, S. C. Apte, G. E. Batley, G. E. Gadd, and P. S. Casey, "Comparative Toxicity of Nanoparticulate ZnO, Bulk ZnO, and ZnCl2 to a Freshwater Microalga (Pseudokirchneriella subcapitata): The Importance of Particle Solubility," Environmental Science & Technology **41**, 8484-8490 (2007).

22. A. Baun, N. B. Hartmann, K. Grieger, and K. O. Kusk, "Ecotoxicity of engineered nanoparticles to aquatic invertebrates: a brief review and recommendations for future toxicity testing," Ecotoxicology **17**, 387-395 (2008).

23. V. Stone, B. Nowack, A. Baun, N. van den Brink, F. von der Kammer, M. Dusinska, R. Handy, S. Hankin, M. Hassellöv, E. Joner, and T. F. Fernandes, "Nanomaterials for environmental studies: Classification, reference material issues, and strategies for physico-chemical characterisation," Science of The Total Environment **408**, 1745-1754 (2010).

24. S. J. Klaine, P. J. J. Alvarez, G. E. Batley, T. F. Fernandes, R. D. Handy, D. Y. Lyon, S. Mahendra, M. J. McLaughlin, and J. R. Lead, "Nanomaterials in the environment: Behavior, fate, bioavailability, and effects," Environmental Toxicology and Chemistry **27**, 1825-1851 (2008).

25. R. Handy, F. von der Kammer, J. Lead, M. Hassellöv, R. Owen, and M. Crane, "The ecotoxicology and chemistry of manufactured nanoparticles," Ecotoxicology **17**, 287-314 (2008).

26. M. Auffan, J. Rose, J.-Y. Bottero, G. V. Lowry, J.-P. Jolivet, and M. R. Wiesner, "Towards a definition of inorganic nanoparticles from an environmental, health and safety perspective," Nature Nanotechnology **4**, 634-641 (2009).

27. G. Oberdörster, E. Oberdörster, and J. Oberdörster, "Nanotoxicology: An Emerging Discipline Evolving from Studies of Ultrafine Particles," Environmental Health Perspectives **113**, 823-839 (2005).

28. A. A. Shvedova, E. R. Kisin, R. Mercer, A. R. Murray, V. J. Johnson, A. I. Potapovich, Y. Y. Tyurina, O. Gorelik, S. Arepalli, D. Schwegler-Berry, A. F. Hubbs, J. Antonini, D. E. Evans, B.-K. Ku, D. Ramsey, A. Maynard, V. E. Kagan, V. Castranova, and P. Baron, "Unusual inflammatory and fibrogenic pulmonary responses to single-walled carbon nanotubes in mice," **289**, L698-L708 (2005).

29. R. Fears, P. Gehr, and E. Anklam, "Nanosafety: How to allay fears over nanomaterials," Nature **488**, 281-281 (2012).

30. M. D. Clift, P. Gehr, and B. Rothen-Rutishauser, "Nanotoxicology: a perspective and discussion of whether or not in vitro testing is a valid alternative," Archives of Toxicology **85**, 723-731 (2011).

31. C. Brandenberger, M. Clift, D. Vanhecke, C. Muhlfeld, V. Stone, P. Gehr, and B. Rothen-Rutishauser, "Intracellular imaging of nanoparticles: Is it an elemental mistake to believe what you see?," Particle and Fibre Toxicology **7**, 15 (2010).

32. H. Bouwmeester, I. Lynch, H. J. P. marvin, K. A. Dawson, M. Berges, D. Braguer, H. J. Byrne, A. Casey, G. Chambers, M. J. D. Clift, G. Elia, T. F. Fernandes, L. B. Fjellsbø, P. Hatto, L. Juillerat, C. Klein, W. G. Kreyling, C. Nickel, M. Riediker,

and V. Stone, "Minimal analytical characterization of engineered nanomaterials needed for hazard assessment in biological matrices," Nanotoxicology **5**, 1-11 (2011).

33. A. E. Nel, L. Madler, D. Velegol, T. Xia, E. M. V. Hoek, P. Somasundaran, F. Klaessig, V. Castranova, and M. Thompson, "Understanding biophysicochemical interactions at the nano-bio interface," Nature Materials **8**, 543-557 (2009).

34. N. von Moos, P. Bowen, and V. I. Slaveykova, "Bioavailability of inorganic nanoparticles to planktonic bacteria and aquatic microalgae in freshwater," Environmental Science: Nano **1**, 214-232 (2014).

35. M. Cap, V. Libuse, and Z. Palková, "Reactive Oxygen Species in the Signaling and Adaptation of Multicellular Microbial Communities," Oxidative Medicine and Cellular Longevity **2012**, 13 (2012).

36. T. Xia, M. Kovochich, J. Brant, M. Hotze, J. Sempf, T. Oberley, C. Sioutas, J. I. Yeh, M. R. Wiesner, and A. E. Nel, "Comparison of the Abilities of Ambient and Manufactured Nanoparticles To Induce Cellular Toxicity According to an Oxidative Stress Paradigm," Nano Letters **6**, 1794-1807 (2006).

37. H. Sies, "Biochemistry of Oxidative Stress," Angewandte Chemie International Edition in English **25**, 1058-1071 (1986).

38. N. Mallick and F. H. Mohn, "Reactive oxygen species: response of algal cells," Journal of Plant Physiology **157**, 183-193 (2000).

39. A. Nel, "Air Pollution-Related Illness: Effects of Particles," Science **308**, 804-806 (2005).

40. G. G. Xiao, M. Wang, N. Li, J. A. Loo, and A. E. Nel, "Use of Proteomics to Demonstrate a Hierarchical Oxidative Stress Response to Diesel Exhaust Particle Chemicals in a Macrophage Cell Line," Journal of Biological Chemistry **278**, 50781-50790 (2003).

41. L. Müller, M. Riediker, P. Wick, M. Mohr, P. Gehr, and B. Rothen-Rutishauser, "Oxidative stress and inflammation response after nanoparticle exposure: differences between human lung cell monocultures and an advanced three-dimensional model of the human epithelial airways," Journal of The Royal Society Interface (2009).

42. K. Apel and H. Hirt, "Reactive oxygen species: metabolism, oxidative stress, and signal transduction," Annual Review Plant Biology **55**, 373-399 (2004).

43. A. D. Maynard, R. J. Aitken, T. Butz, V. Colvin, K. Donaldson, G. Oberdorster, M. A. Philbert, J. Ryan, A. Seaton, V. Stone, S. S. Tinkle, L. Tran, N. J. Walker, and D. B. Warheit, "Safe handling of nanotechnology," Nature **444**, 267-269 (2006).

44. M. S. Cooke, M. D. Evans, M. Dizdarglu, and J. Lunec, "Oxidative DNA damage: mechanisms, mutation, and disease," The FASEB Journal **17**, 1195-1214 (2003).

45. M. Gasser, M. Riediker, L. Mueller, A. Perrenoud, F. Blank, P. Gehr, and B. Rothen-Rutishauser, "Toxic effects of brake wear particles on epithelial lung cells in vitro," Particle and Fibre Toxicology **6**, 30 (2009).

46. L. G. G. Henyey, J. L., "Diffuse radiation in the Galaxy," Astrophysical Journal **93**, 70-83 (1941).

47. S. Feng, C. Kane, P. A. Lee, and A. D. Stone, "Correlations and Fluctuations of Coherent Wave Transmission through Disordered Media," Physical Review Letters **61**, 834-837 (1988).

48. J. Gross, "Connective Tissue Fine Structure and Some Methods for Its Analysis," Journal of Gerontology **5**, 343-360 (1950).

49. P. W. Anderson, "Absence of Diffusion in Certain Random Lattices," Physical Review **109**, 1492-1505 (1958).

50. S. John, "Electromagnetic Absorption in a Disordered Medium near a Photon Mobility Edge," Physical Review Letters **53**, 2169-2172 (1984).

51. D. S. Wiersma, P. Bartolini, A. Lagendijk, and R. Righini, "Localization of light in a disordered medium," Nature **390**, 671-673 (1997).

52. M. Störzer, P. Gross, C. M. Aegerter, and G. Maret, "Observation of the Critical Regime Near Anderson Localization of Light," Physical Review Letters **96**, 063904 (2006).

53. M. Segev, Y. Silberberg, and D. N. Christodoulides, "Anderson localization of light," Nature Photonics **7**, 197-204 (2013).

54. L. Levi, Y. Krivolapov, S. Fishman, and M. Segev, "Hyper-transport of light and stochastic acceleration by evolving disorder," Nature Physics **8**, 912-917 (2012).

55. T. Strudley, T. Zehender, C. Blejean, E. P. A. M. Bakkers, and O. L. Muskens, "Mesoscopic light transport by very strong collective multiple scattering in nanowire mats," Nature Photonics **7**, 413-418 (2013).

56. S. S. Paolo, L. M. Otto, and L. Ad, "Weak localization of photon noise," New Journal of Physics **15**, 105009 (2013).

57. T. Strudley, D. Akbulut, W. L. Vos, A. Lagendijk, A. P. Mosk, and O. L. Muskens, "Observation of intensity statistics of light transmitted through 3D random media," Optics Letters **39**, 6347-6350 (2014).

58. O. L. Muskens, T. van der Beek, and A. Lagendijk, "Angle dependence of the frequency correlation in random photonic media: Diffusive regime and its breakdown near localization," Physical Review B **84**, 035106 (2011).

59. O. L. Muskens and A. Lagendijk, "Method for broadband spectroscopy of light transport through opaque scattering media," Optics Letters **34**, 395-397 (2009).

60. M. P. V. Albada and A. Lagendijk, "Observation of Weak Localization of Light in a Random Medium," Physical Review Letters **55**, 2692-2695 (1985).

61. G. Strangi, S. Ferjani, V. Barna, A. De Luca, C. Versace, N. Scaramuzza, and R. Bartolino, "Random lasing and weak localization of light indye-doped nematic liquid crystals," Optics Express **14**, 7737-7744 (2006).

62. Z. Yaqoob, D. Psaltis, M. S. Feld, and C. Yang, "Optical phase conjugation for turbidity suppression in biological samples," Nature Photonics **2**, 110-115 (2008).

63. S. M. Popoff, G. Lerosey, R. Carminati, M. Fink, A. C. Boccara, and S. Gigan, "Measuring the Transmission Matrix in Optics: An Approach to the Study and Control of Light Propagation in Disordered Media," Physical Review Letters **104**, 100601 (2010).

64. Y. D. Chong and A. D. Stone, "Hidden Black: Coherent Enhancement of Absorption in Strongly Scattering Media," Physical Review Letters **107**, 163901 (2011).

65. M. Kim, Y. Choi, C. Yoon, W. Choi, J. Kim, Q. H. Park, and W. Choi, "Maximal energy transport through disordered media with the implementation of transmission eigenchannels," Nature Photonics **6**, 581-585 (2012).

66. Y. Choi, T. R. Hillman, W. Choi, N. Lue, R. R. Dasari, P. T. C. So, W. Choi, and Z. Yaqoob, "Measurement of the Time-Resolved Reflection Matrix for Enhancing Light Energy Delivery into a Scattering Medium," Physical Review Letters **111**, 243901 (2013).

67. I. M. Vellekoop, A. Lagendijk, and A. P. Mosk, "Exploiting disorder for perfect focusing," Nature Photonics **4**, 320-322 (2010).

68. H. Cao, Y. G. Zhao, S. T. Ho, E. W. Seelig, Q. H. Wang, and R. P. H. Chang, "Random Laser Action in Semiconductor Powder," Physical Review Letters **82**, 2278-2281 (1999).

69. H. Cao, "Lasing in random media," Waves in Random Media **13**, R1-R39 (2003).

70.   D. S. Wiersma and A. Lagendijk, "Light diffusion with gain and random lasers," Physical Review E **54**, 4256-4265 (1996).

71.   D. S. Wiersma, "The physics and applications of random lasers," Nature Physics **4**, 359-367 (2008).

72.   R. G. S. El-Dardiry, A. P. Mosk, O. L. Muskens, and A. Lagendijk, "Experimental studies on the mode structure of random lasers," Physical Review A **81**, 043830 (2010).

73.   R. Nossal, R. F. Bonner, and G. H. Weiss, "Influence of path length on remote optical sensing of properties of biological tissue," Applied Optics **28**, 2238-2244 (1989).

74.   A. Lev, Z. Kotler, and B. G. Sfez, "Ultrasound tagged light imaging in turbid media in a reflectance geometry," Optics Letters **25**, 378-380 (2000).

75.   S. Popoff, G. Lerosey, M. Fink, A. C. Boccara, and S. Gigan, "Image transmission through an opaque material," Nature Communication **1**, 81 (2010).

76.   J. Bertolotti, E. G. van Putten, C. Blum, A. Lagendijk, W. L. Vos, and A. P. Mosk, "Non-invasive imaging through opaque scattering layers," Nature **491**, 232-234 (2012).

77.   X. Xu, H. Liu, and L. V. Wang, "Time-reversed ultrasonically encoded optical focusing into scattering media," Nature Photonics **5**, 154-157 (2011).

78.   F. Pratesi, M. Burresi, F. Riboli, K. Vynck, and D. S. Wiersma, "Disordered photonic structures for light harvesting in solar cells," Optics Express **21**, A460-A468 (2013).

79.   K. Vynck, M. Burresi, F. Riboli, and D. S. Wiersma, "Photon management in two-dimensional disordered media," Nature Materials **11**, 1017-1022 (2012).

80.   O. L. Muskens, J. G. Rivas, R. E. Algra, E. P. A. M. Bakkers, and A. Lagendijk, "Design of Light Scattering in Nanowire Materials for Photovoltaic Applications," Nano Letters **8**, 2638-2642 (2008).

81.   J. Gomez Rivas, R. Spirk, L. D. Noordam, C. W. Rella and A. Lagendijk, "Static and dynamic transport of light close to the Anderson localization transition", Physical Review E, **63**, 046613 (2001).

82.   O. L. Muskens, S. L. Diedenhofen, B. C. Kaas, R. E. Algra, E. P. A. M. Bakkers, J. Gómez Rivas, and A. Lagendijk, "Large Photonic Strength of Highly Tunable Resonant Nanowire Materials," Nano Letters **9**, 930-934 (2009).

83.   T. Svensson, E. Adolfsson, M. Lewander, C. T. Xu, and S. Svanberg, "Disordered, Strongly Scattering Porous Materials as Miniature Multipass Gas Cells," Physical Review Letters **107**, 143901 (2011).

84.   C.-M. Pradier, M. Salmain, L. Zheng, and G. Jaouen, "Specific binding of avidin to biotin immobilised on modified gold surfaces: Fourier transform infrared reflection absorption spectroscopy analysis," Surface Science **502–503**, 193-202 (2002).

85.   Y. Zubavichus, A. Shaporenko, V. Korolkov, M. Grunze, and M. Zharnikov, "X-ray Absorption Spectroscopy of the Nucleotide Bases at the Carbon, Nitrogen, and Oxygen K-Edges," The Journal of Physical Chemistry B **112**, 13711-13716 (2008).

86.   A. L. Roe, D. J. Schneider, R. J. Mayer, J. W. Pyrz, J. Widom, and L. Que, "X-ray absorption spectroscopy of iron-tyrosinate proteins," Journal of the American Chemical Society **106**, 1676-1681 (1984).

87.   K. Namjou, C. B. Roller, T. E. Reich, J. D. Jeffers, G. L. McMillen, P. J. McCann, and M. A. Camp, "Determination of exhaled nitric oxide distributions in a diverse sample population using tunable diode laser absorption spectroscopy," Applied Physics B **85**, 427-435 (2006).

88. Z. Shervani, H. Etori, K. Taga, T. Yoshida, and H. Okabayashi, "Aggregation of polyene antibiotics as studied by electronic absorption and circular dichroism spectroscopies," Colloids and Surfaces B: Biointerfaces **7**, 31-38 (1996).

89. K. Kaznacheyev, A. Osanna, C. Jacobsen, O. Plashkevych, O. Vahtras, Ågren, V. Carravetta, and A. P. Hitchcock, "Innershell Absorption Spectroscopy of Amino Acids," The Journal of Physical Chemistry A **106**, 3153-3168 (2002).

90. E. P. Maris, W. C. Ketchie, V. Oleshko, and R. J. Davis, "Metal Particle Growth during Glucose Hydrogenation over Ru/SiO2 Evaluated by X-ray Absorption Spectroscopy and Electron Microscopy," The Journal of Physical Chemistry B **110**, 7869-7876 (2006).

91. T. Wang, S. Walden, and R. Egan, "Development and validation of a general non-digestive method for the determination of palladium in bulk pharmaceutical chemicals and their synthetic intermediates by graphite furnace atomic absorption spectroscopy," Journal of Pharmaceutical and Biomedical Analysis **15**, 593-599 (1997).

92. H. Anawar, A. Garcia-Sanchez, M. Hossain, and S. Akter, "Evaluation of Health Risk and Arsenic Levels in Vegetables Sold in Markets of Dhaka (Bangladesh) and Salamanca (Spain) by Hydride Generation Atomic Absorption Spectroscopy," Bulletin of Environmental Contamination and Toxicology **89**, 620-625 (2012).

93. C. M. Riley, L. A. Sternson, and A. J. Repta, "Assessment of cisplatin reactivity with peptides and proteins using reverse-phase high-performance liquid chromatography and flameless atomic absorption spectroscopy," Analytical Biochemistry **124**, 167-179 (1982).

94. R. Li, H.-P. Loock, and R. D. Oleschuk, "Capillary Electrophoresis Absorption Detection Using Fiber-Loop Ring-Down Spectroscopy," Analytical Chemistry **78**, 5685-5692 (2006).

95. W.-Y. Chen, L.-Y. Chen, C.-M. Ou, C.-C. Huang, S.-C. Wei, and H.-T. Chang, "Synthesis of Fluorescent Gold Nanodot–Liposome Hybrids for Detection of Phospholipase C and Its Inhibitor," Analytical Chemistry **85**, 8834-8840 (2013).

96. Y. Dou, X. Yang, Z. Liu, and S. Zhu, "Homocysteine-functionalized silver nanoparticles for selective sensing of Cu2+ ions and Lidocaine hydrochloride," Colloids and Surfaces A: Physicochemical and Engineering Aspects **423**, 20-26 (2013).

97. S. Tong, B. Ren, Z. Zheng, H. Shen, and G. Bao, "Tiny Grains Give Huge Gains: Nanocrystal-Based Signal Amplification for Biomolecule Detection," ACS Nano **7**, 5142-5150 (2013).

98. Y. Zhang, C. Pilapong, Y. Guo, Z. Ling, O. Cespedes, P. Quirke, and D. Zhou, "Sensitive, Simultaneous Quantitation of Two Unlabeled DNA Targets Using a Magnetic Nanoparticle–Enzyme Sandwich Assay," Analytical Chemistry **85**, 9238-9244 (2013).

99. A. Shevchenko, M. Wilm, O. Vorm, and M. Mann, "Mass Spectrometric Sequencing of Proteins from Silver-Stained Polyacrylamide Gels," Analytical Chemistry **68**, 850-858 (1996).

100. F. A. Armstrong, H. A. O. Hill, and N. J. Walton, "Direct electrochemistry of redox proteins," Accounts of Chemical Research **21**, 407-413 (1988).

101. M. M. Rauhut, "Chemiluminescence from concerted peroxide decomposition reactions," Accounts of Chemical Research **2**, 80-87 (1969).

102. B. Valeur and M. r. N. Berberan-Santos, "A Brief History of Fluorescence and Phosphorescence before the Emergence of Quantum Theory," Journal of Chemical Education **88**, 731-738 (2011).

103. C. F. Bohren and D. R. Huffman, "Electromagnetic Theory," in *Absorption and Scattering of Light by Small Particles* (Wiley-VCH Verlag GmbH, 2007), pp. 12-56.

104. M. Gupta and A. O'Keefe, "Cavity-enhanced liquid absorption spectroscopy," US 6839140 B1 (2002).

105. A. B. Dahlin, J. O. Tegenfeldt, and F. Höök, "Improving the Instrumental Resolution of Sensors Based on Localized Surface Plasmon Resonance," Analytical Chemistry **78**, 4416-4423 (2006).

106. S. Nie and S. R. Emory, "Probing Single Molecules and Single Nanoparticles by Surface-Enhanced Raman Scattering," Science **275**, 1102-1106 (1997).

107. Y. H. Wong, R. L. Thomas, and G. F. Hawkins, "Surface and subsurface structure of solids by laser photoacoustic spectroscopy," Applied Physics Letters **32**, 538-539 (1978).

108. M. Franko and C. D. Tran, "Thermal lens effect in electrolyte and surfactant media," The Journal of Physical Chemistry **95**, 6688-6696 (1991).

109. K.-I. Tsunoda, A. Nomura, J. Yamada, and S. Nishi, "The Possibility of Signal Enhancement in Liquid Absorption Spectrometry with a Long Capillary Cell Utilizing Successive Total Reflection at the Outer Cell Surface," Applied Spectroscopy **43**, 49-55 (1989).

110. A. O'Keefe and D. A. G. Deacon, "Cavity ring-down optical spectrometer for absorption measurements using pulsed laser sources," Review of Scientific Instruments **59**, 2544-2551 (1988).

111. J. Hodgkinson, D. Masiyano, and R. P. Tatam, "Using integrating spheres as absorption cells: path-length distribution and application of Beer's law," Applied Optics **48**, 5748-5758 (2009).

112. J. Greener, B. Abbasi, and E. Kumacheva, "Attenuated total reflection Fourier transform infrared spectroscopy for on-chip monitoring of solute concentrations," Lab on a Chip **10**, 1561-1566 (2010).

113. A. D. Kim, "Transport theory for light propagation in biological tissue," Journal of the Optical Society of America A **21**, 820-827 (2004).

114. S. Mujumdar, R. Torre, H. Ramachandran, and D. Wiersma, "Monte Carlo calculations of spectral features in random lasing," Journal of Nanophotonics **4**, 041550-041513 (2010).

115. R. Uppu, A. K. Tiwari, and S. Mujumdar, "Coherent random lasing in diffusive resonant media," AIP Conference Proceedings **1398**, 103-105 (2011).

116. D. Toublanc, "Henyey-Greenstein and Mie phase functions in Monte Carlo radiative transfer computations," Applied Optics **35**, 3270-3274 (1996).

117. O. Mengual, G. Meunier, I. Cayré, K. Puech, and P. Snabre, "TURBISCAN MA 2000: multiple light scattering measurement for concentrated emulsion and suspension instability analysis," Talanta **50**, 445-456 (1999).

118. R. Uppu and S. Mujumdar, "Persistent coherent random lasing using resonant scatterers," Optics Express **19**, 23523-23531 (2011).

119. E. Hecht and A. Zajac, "Optics" Addison-Wesley, 301-305 (1974).

120. S. F. Liew, J. Forster, H. Noh, C. F. Schreck, V. Saranathan, X. Lu, L. Yang, R. O. Prum, C. S. O'Hern, E. R. Dufresne, and H. Cao, "Short-range order and near-field effects on optical scattering and structural coloration," Optics Express **19**, 8208-8217 (2011).

121. V. Gusak, L.-P. Heiniger, V. P. Zhdanov, M. Gratzel, B. Kasemo, and C. Langhammer, "Diffusion and adsorption of dye molecules in mesoporous TiO2 photoelectrodes studied by indirect nanoplasmonic sensing," Energy & Environmental Science **6**, 3627-3636 (2013).

122. Y. Berthois, J. A. Katzenellenbogen, and B. S. Katzenellenbogen, "Phenol red in tissue culture media is a weak estrogen: implications concerning the study of estrogen-responsive cells in culture," Proceedings of the National Academy of Sciences **83**, 2496-2500 (1986).

123. X. Liu, M. Atwater, J. Wang, and Q. Huo, "Extinction coefficient of gold nanoparticles with different sizes and different capping ligands," Colloids and Surfaces B: Biointerfaces **58**, 3-7 (2007).

124. O. L. Muskens, P. Billaud, M. Broyer, N. Del Fatti, and F. Vallée, "Optical extinction spectrum of a single metal nanoparticle: Quantitative characterization of a particle and of its local environment," Physical Review B **78**, 205410 (2008).

125. O. L. Muskens, G. Bachelier, N. D. Fatti, F. Vallée, A. Brioude, X. Jiang, and M.-P. Pileni, "Quantitative Absorption Spectroscopy of a Single Gold Nanorod," The Journal of Physical Chemistry C **112**, 8917-8921 (2008).

126. A. Arbouet, D. Christofilos, N. Del Fatti, F. Vallée, J. R. Huntzinger, L. Arnaud, P. Billaud, and M. Broyer, "Direct Measurement of the Single-Metal-Cluster Optical Absorption," Physical Review Letters **93**, 127401 (2004).

127. D. Boyer, P. Tamarat, A. Maali, B. Lounis, and M. Orrit, "Photothermal Imaging of Nanometer-Sized Metal Particles Among Scatterers," Science **297**, 1160-1163 (2002).

128. A. Mitra, B. Deutsch, F. Ignatovich, C. Dykes, and L. Novotny, "Nano-optofluidic Detection of Single Viruses and Nanoparticles," ACS Nano **4**, 1305-1312 (2010).

129. W.-Y. Chen, L.-Y. Chen, C.-M. Ou, C.-C. Huang, S.-C. Wei, and H.-T. Chang, "Synthesis of Fluorescent Gold Nanodot–Liposome Hybrids for Detection of Phospholipase C and Its Inhibitor," Analytical Chemistry **85**, 8834-8840(2013).

130. Y. Zhang, C. Pilapong, Y. Guo, Z. Ling, O. Cespedes, P. Quirke, and D. Zhou, "Sensitive, Simultaneous Quantitation of Two Unlabeled DNA Targets Using a Magnetic Nanoparticle–Enzyme Sandwich Assay," Analytical Chemistry **85**, 9238-9244 (2013).

131. G. J. Lee, P. Attri, E. H. Choi, Y.-W. Kwon, I. Krasnikov, and A. Seteikin, "Optical and Structural Properties of Nanobiomaterials," Journal of Nanoscience and Nanotechnology **14**, 221-249 (2014).

132. K. J. Davies, "Oxidative stress: the paradox of aerobic life," Biochemical Symposium **61**, 1-31 (1995).

133. Y. Song, N. Driessens, M. Costa, X. De Deken, V. Detours, B. Corvilain, C. Maenhaut, F. Miot, J. Van Sande, M.-C. Many, and J. E. Dumont, "Roles of Hydrogen Peroxide in Thyroid Physiology and Disease," Journal of Clinical Endocrinology & Metabolism **92**, 3764-3773 (2007).

134. W. L. Daniel, M. S. Han, J.-S. Lee, and C. A. Mirkin, "Colorimetric Nitrite and Nitrate Detection with Gold Nanoparticle Probes and Kinetic End Points," Journal of the American Chemical Society **131**, 6362-6363 (2009).

135. D. J. Pine, D. A. Weitz, P. M. Chaikin, and E. Herbolzheimer, "Diffusing wave spectroscopy," Physical Review Letters **60**, 1134-1137 (1988).

136. F. A. L. Dullien, *Porous Media. Fluid Transport and Pore Structure* (Academic Press Inc., 1992).

137. C. F. Bohren and D. R. Huffman, "Absorption and Scattering by a Sphere," in *Absorption and Scattering of Light by Small Particles* (Wiley-VCH Verlag GmbH, 2007), pp. 82-129.

138. R. Rammal and B. Doucot, "Invariant imbedding approach to localization. I. General framework and basic equations," Journal Physics France **48**, 509-526 (1987).

139. V. Freilikher, M. Pustilnik, and I. Yurkevich, "Effect of Absorption on the Wave Transport in the Strong Localization Regime," Physical Review Letters **73**, 810-813 (1994).
140. Z.-Q. Zhang, "Light amplification and localization in randomly layered media with gain," Physical Review B **52**, 7960-7964 (1995).
141. P. Pradhan and N. Kumar, "Localization of light in coherently amplifying random media," Physical Review B **50**, 9644-9647 (1994).
142. C. W. J. Beenakker, J. C. J. Paasschens, and P. W. Brouwer, "Probability of Reflection by a Random Laser," Physical Review Letters **76**, 1368-1371 (1996).
143. J. C. J. Paasschens, T. S. Misirpashaev, and C. W. J. Beenakker, "Localization of light: Dual symmetry between absorption and amplification," Physical Review B **54**, 11887-11890 (1996).
144. J. Heinrichs, "Light amplification and absorption in a random medium," Physical Review B **56**, 8674-8682 (1997).
145. A. K. Gupta and A. M. Jayannavar, "Electron wave transport in coherently absorptive random media," Physical Review B **52**, 4156-4161 (1995).
146. S. K. Joshi and A. M. Jayannavar, "Transmission and reflection from a disordered lasing medium," Physical Review B **56**, 12038-12041 (1997).
147. P. K. Datta, "Transmission and reflection in a perfectly amplifying and absorbing medium," Physical Review B **59**, 10980-10984 (1999).
148. X. Jiang and C. M. Soukoulis, "Transmission and reflection studies of periodic and random systems with gain," Physical Review B **59**, 6159-6166 (1999).
149. A. Y. Zyuzin, "Transmission fluctuations and spectral rigidity of lasing states in a random amplifying medium," Physical Review E **51**, 5274-5278 (1995).
150. A. Y. Zyuzin, "Weak Localization in Backscattering from an Amplifying Medium," Europhysics Letters **26**, 517 (1994).
151. P. Snabre and A. Arhaliass, "Anisotropic scattering of light in random media: incoherent backscattered spotlight," Applied Optics **37**, 4017-4026 (1998).
152. S. F. Liew, S. M. Popoff, A. P. Mosk, W. L. Vos, and H. Cao, "Transmission channels for light in absorbing random media: From diffusive to ballistic-like transport," Physical Review B **89**, 224202 (2014).
153. Y. Hamakawa, *Thin-film solar cells: next generation photovoltaics and its applications* (Springer Science & Business Media, 2004), Vol. 13.
154. A. Polman and H. A. Atwater, "Photonic design principles for ultrahigh-efficiency photovoltaics," Nature Materials **11**, 174-177 (2012).
155. K. Tvingstedt, S. Dal Zilio, O. Inganäs, and M. Tormen, "Trapping light with micro lenses in thin film organic photovoltaic cells," Optics Express **16**, 21608-21615 (2008).
156. S. D. Zilio, K. Tvingstedt, O. Inganäs, and M. Tormen, "Fabrication of a light trapping system for organic solar cells," Microelectronic Engineering **86**, 1150-1154 (2009).
157. S.-B. Rim, S. Zhao, S. R. Scully, M. D. McGehee, and P. Peumans, "An effective light trapping configuration for thin-film solar cells," Applied Physics Letters **91**, 243501 (2007).
158. Y. Zhou, F. Zhang, K. Tvingstedt, W. Tian, and O. Inganäs, "Multifolded polymer solar cells on flexible substrates," Applied Physics Letters **93**, 033302 (2008).
159. L. Song and A. Uddin, "Design of high efficiency organic solar cell with light trapping," Optics Express **20**, A606-A621 (2012).
160. H. A. Atwater and A. Polman, "Plasmonics for improved photovoltaic devices," Nature Materials **9**, 205-213 (2010).
161. K. R. Catchpole and A. Polman, "Plasmonic solar cells," Optics Express **16**, 21793-21800 (2008).

162. V. E. Ferry, J. N. Munday, and H. A. Atwater, "Design Considerations for Plasmonic Photovoltaics," Advanced Materials **22**, 4794-4808 (2010).

163. C. Cocoyer, L. Rocha, L. Sicot, B. Geffroy, R. de Bettignies, C. Sentein, C. Fiorini-Debuisschert, and P. Raimond, "Implementation of submicrometric periodic surface structures toward improvement of organic-solar-cell performances," Applied Physics Letters **88**, 133108 (2006).

164. J. B. Kim, P. Kim, N. C. Pegard, S. J. Oh, C. R. Kagan, J. W. Fleischer, H. A. Stone, and Y.-L. Loo, "Wrinkles and deep folds as photonic structures in photovoltaics," Nature Photonics **6**, 327-332 (2012).

165. Y. Yao, J. Yao, V. K. Narasimhan, Z. Ruan, C. Xie, S. Fan, and Y. Cui, "Broadband light management using low-Q whispering gallery modes in spherical nanoshells," Nature Communication **3**, 664 (2012).

166. P. Spinelli, M. A. Verschuuren, and A. Polman, "Broadband omnidirectional antireflection coating based on subwavelength surface Mie resonators," Nature Communication **3**, 692 (2012).

167. Z. Tang, W. Tress, and O. Inganäs, "Light trapping in thin film organic solar cells," Materials Today **3**, 150 (2011).

168. C. Battaglia, J. Escarre, K. Soderstrom, M. Charriere, M. Despeisse, F.-J. Haug, and C. Ballif, "Nanomoulding of transparent zinc oxide electrodes for efficient light trapping in solar cells," Nature Photonics **5**, 535-538 (2011).

169. S. Basu Mallick, M. Agrawal, A. Wangperawong, E. S. Barnard, K. K. Singh, R. J. Visser, M. L. Brongersma, and P. Peumans, "Ultrathin crystalline-silicon solar cells with embedded photonic crystals," Applied Physics Letters **100**, 053113 (2012).

170. D. Madzharov, R. Dewan, and D. Knipp, "Influence of front and back grating on light trapping in microcrystalline thin-film silicon solar cells," Optics Express **19**, A95-A107 (2011).

171. C. Rockstuhl, S. Fahr, K. Bittkau, T. Beckers, R. Carius, F. J. Haug, T. Söderström, C. Ballif, and F. Lederer, "Comparison and optimization of randomly textured surfaces in thin-film solar cells," Optics Express **18**, A335-A341 (2010).

172. V. E. Ferry, M. A. Verschuuren, M. C. v. Lare, R. E. I. Schropp, H. A. Atwater, and A. Polman, "Optimized Spatial Correlations for Broadband Light Trapping Nanopatterns in High Efficiency Ultrathin Film a-Si:H Solar Cells," Nano Letters **11**, 4239-4245 (2011).

173. J. H. Karp, E. J. Tremblay, and J. E. Ford, "Planar micro-optic solar concentrator," Optics Express **18**, 1122-1133 (2010).

174. B. Kalyanaraman, V. Darley-Usmar, K. J. A. Davies, P. A. Dennery, H. J. Forman, M. B. Grisham, G. E. Mann, K. Moore, L. J. Roberts Ii, and H. Ischiropoulos, "Measuring reactive oxygen and nitrogen species with fluorescent probes: challenges and limitations," Free Radical Biology and Medicine **52**, 1-6 (2012).

175. U. Resch-Genger, M. Grabolle, S. Cavaliere-Jaricot, R. Nitschke, and T. Nann, "Quantum dots versus organic dyes as fluorescent labels," Nature Methods **5**, 763-775 (2008).

176. G. Suarez, C. Santschi, V. I. Slaveykova, and O. J. F. Martin, "Sensing the dynamics of oxidative stress using enhanced absorption in protein-loaded random media," Scientific Reports **3**(2013).

177. H. Jin, D. A. Heller, M. Kalbacova, J.-H. Kim, J. Zhang, A. A. Boghossian, N. Maheshri, and M. S. Strano, "Detection of single-molecule H_2O_2 signalling from epidermal growth factor receptor using fluorescent single-walled carbon nanotubes," Nature Nanotechnology **5**, 302-309 (2010).

178. W. Dröge, "Free Radicals in the Physiological Control of Cell Function," Physiological Reviews **82**, 47-95 (2002).

179. N. von Moos and V. I. Slaveykova, "Oxidative stress induced by inorganic nanoparticles in bacteria and aquatic microalgae – state of the art and knowledge gaps," Nanotoxicology **8**, 605-630 (2014).

180. J. Zhang, R. E. Campbell, A. Y. Ting, and R. Y. Tsien, "Creating new fluorescent probes for cell biology," Nature Review Molecular Cell Biology **3**, 906-918 (2002).

181. T. A. Pearson, G. A. Mensah, R. W. Alexander, J. L. Anderson, R. O. Cannon, M. Criqui, Y. Y. Fadl, S. P. Fortmann, Y. Hong, G. L. Myers, N. Rifai, S. C. Smith, K. Taubert, R. P. Tracy, and F. Vinicor, "Markers of Inflammation and Cardiovascular Disease: Application to Clinical and Public Health Practice: A Statement for Healthcare Professionals From the Centers for Disease Control and Prevention and the American Heart Association," Circulation **107**, 499-511 (2003).

182. E. A. McGlynn, S. M. Asch, J. Adams, J. Keesey, J. Hicks, A. DeCristofaro, and E. A. Kerr, "The Quality of Health Care Delivered to Adults in the United States," New England Journal of Medicine **348**, 2635-2645 (2003).

183. S. Granick and S. I. Beale, "Hemes, Chlorophylls, and Related Compounds: Biosynthesis and Metabolic Regulation," in *Advances in Enzymology and Related Areas of Molecular Biology* (John Wiley & Sons, Inc., 2006), pp. 33-203.

184. C. M. Masimirembwa, R. Thompson, and T. B. Andersson, "In Vitro High Throughput Screening of Compounds for Favorable Metabolic Properties in Drug Discovery," Combinatorial Chemistry & High Throughput Screening **4**, 245-263 (2001).

185. B. Ahrén and H. Larsson, "Quantification of Insulin Secretion in Relation to Insulin Sensitivity in Nondiabetic Postmenopausal Women," Diabetes **51**, S202-S211 (2002).

186. B. A. Gregg and A. Heller, "Cross-linked redox gels containing glucose oxidase for amperometric biosensor applications," Analytical Chemistry **62**, 258-263 (1990).

187. Y. Lin, F. Lu, Y. Tu, and Z. Ren, "Glucose Biosensors Based on Carbon Nanotube Nanoelectrode Ensembles," Nano Letters **4**, 191-195 (2003).

188. J. Tuomilehto, J. Lindström, J. G. Eriksson, T. T. Valle, H. Hämäläinen, P. Ilanne-Parikka, S. Keinänen-Kiukaanniemi, M. Laakso, A. Louheranta, M. Rastas, V. Salminen, S. Aunola, Z. Cepaitis, V. Moltchanov, M. Hakumäki, M. Mannelin, V. Martikkala, J. Sundvall, and M. Uusitupa, "Prevention of Type 2 Diabetes Mellitus by Changes in Lifestyle among Subjects with Impaired Glucose Tolerance," New England Journal of Medicine **344**, 1343-1350 (2001).

189. O. Lev, Z. Wu, S. Bharathi, V. Glezer, A. Modestov, J. Gun, L. Rabinovich, and S. Sampath, "Sol–Gel Materials in Electrochemistry," Chemistry of Materials **9**, 2354-2375 (1997).

190. G. Strom, "The Influence of Anoxia on Lactate Utilization in Man after Prolonged Muscnlar Work," Acta Physiologica Scandinavica **17**, 440-451 (1949).

191. W. E. Huckabee, "Relationships of pyruvate and lactate during anaerobic metabolism. I. Effects of infusion of pyruvate or glucose and of hyperventilation," The Journal of Clinical Investigation **37**, 244-254 (1958).

192. M. H. Weil and A. A. Afifi, "Experimental and Clinical Studies on Lactate and Pyruvate as Indicators of the Severity of Acute Circulatory Failure (Shock)," Circulation **41**, 989-1001 (1970).

193. M. R. Liebowitz, A. J. Fyer, J. M. Gorman, and et al., "Lactate provocation of panic attacks: I. clinical and behavioral findings," Archives of General Psychiatry **41**, 764-770 (1984).

194.   L. B. Gladden, "Lactate metabolism: a new paradigm for the third millennium," The Journal of Physiology **558**, 5-30 (2004).

195.   B. Kubera, C. Hubold, S. Otte, A. S. Lindenberg, I. Zeiß, R. Krause, M. Steinkamp, J. Klement, S. Entringer, L. Pellerin, and A. Peters, "Rise in Plasma Lactate Concentrations with Psychosocial Stress: A Possible Sign of Cerebral Energy Demand," Obesity Facts **5**, 384-392 (2012).

196.   L. Li, Y. Wang, L. Pan, Y. Shi, W. Cheng, Y. Shi, and G. Yu, "A Nanostructured Conductive Hydrogels-Based Biosensor Platform for Human Metabolite Detection," Nano Letters **15**, 1146-1151 (2015).

197.   R. M. Wightman, "Probing Cellular Chemistry in Biological Systems with Microelectrodes," Science **311**, 1570-1574 (2006).

198.   G. Suárez, C. Santschi, O. J. F. Martin, and V. I. Slaveykova, "Biosensor based on chemically-designed anchorable cytochrome c for the detection of H_2O_2 released by aquaticcells," Biosensors and Bioelectronics **42**, 385-390 (2013).

199.   C. Boero, S. Carrara, G. Del Vecchio, L. Calza, and G. De Micheli, "Highly Sensitive Carbon Nanotube-Based Sensing for Lactate and Glucose Monitoring in Cell Culture," NanoBioscience, IEEE Transactions on **10**, 59-67 (2011).

200.   R. Garjonyte, Y. Yigzaw, R. Meskys, A. Malinauskas, and L. Gorton, "Prussian Blue- and lactate oxidase-based amperometric biosensor for lactic acid," Sensors and Actuators B: Chemical **79**, 33-38 (2001).

201.   G. Kenausis, Q. Chen, and A. Heller, "Electrochemical Glucose and Lactate Sensors Based on "Wired" Thermostable Soybean Peroxidase Operating Continuously and Stably at 37 °C," Analytical Chemistry **69**, 1054-1060 (1997).

202.   K. Sirkar, A. Revzin, and M. V. Pishko, "Glucose and Lactate Biosensors Based on Redox Polymer/Oxidoreductase Nanocomposite Thin Films," Analytical Chemistry **72**, 2930-2936 (2000).

203.   W. Putzbach and N. Ronkainen, "Immobilization Techniques in the Fabrication of Nanomaterial-Based Electrochemical Biosensors: A Review," Sensors **13**, 4811-4840 (2013).

204.   E. Miller, A. Albers, A. Pralle, E. Isacoff, and C. Chang, "Boronate-based fluorescent probes for imaging cellular hydrogen peroxide," Journal of the American Chemical Society **127**, 16652-16659 (2005).

205.   H. Chen, R. Li, L. Lin, G. Guo, and J.-M. Lin, "Determination of l-ascorbic acid in human serum by chemiluminescence based on hydrogen peroxide–sodium hydrogen carbonate–CdSe/CdS quantum dots system," Talanta **81**, 1688-1696 (2010).

206.   W. Chen, L. Hong, A.-L. Liu, J.-Q. Liu, X.-H. Lin, and X.-H. Xia, "Enhanced chemiluminescence of the luminol-hydrogen peroxide system by colloidal cupric oxide nanoparticles as peroxidase mimic," Talanta **99**, 643-648 (2012).

207.   Y.-S. Li, X. Ju, X.-F. Gao, and W. Yang, "A Novel Immobilization Enzyme Lactate Fluorescence Capillary Biosensor," Chinese Journal of Analytical Chemistry **37**, 637-642 (2009).

208.   D. C. Klonoff, "Overview of Fluorescence Glucose Sensing: A Technology with a Bright Future," Journal of Diabetes Science and Technology **6**, 1242-1250 (2012).

209.   A. Grossman, "In the Grip of Algal Genomics," in *Transgenic Microalgae as Green Cell Factories*, R. León, A. Galván, and E. Fernández, eds. (Springer New York, 2007), pp. 54-76.

210.   B. O. Dabbousi, J. Rodriguez-Viejo, F. V. Mikulec, J. R. Heine, H. Mattoussi, R. Ober, K. F. Jensen, and M. G. Bawendi, "(CdSe)ZnS Core–Shell Quantum Dots: Synthesis and Characterization of a Size Series of Highly Luminescent Nanocrystallites," The Journal of Physical Chemistry B **101**, 9463-9475 (1997).

211. E.-J. Park, J. Yi, K.-H. Chung, D.-Y. Ryu, J. Choi, and K. Park, "Oxidative stress and apoptosis induced by titanium dioxide nanoparticles in cultured BEAS-2B cells," Toxicology Letters **180**, 222-229 (2008).

212. R. A. Pelroy, R. Rippka, and R. Y. Stanier, "Metabolism of glucose by unicellular blue-green algae," Archiv für Mikrobiologie **87**, 303-322 (1972).

213. E. A. Drew, "Uptake and metabolism of exogenously supplied sugards by brown algae," New Phytologist **68**, 35-43 (1969).

214. P. Xie, I. Fujii, J. Zhao, en, M. Shinohara, and M. Matsukura, "A Novel Polysaccharide Compound Derived from Algae Extracts Protects Retinal Pigment Epithelial Cells from High Glucose-Induced Oxidative Damage in Vitro," Biological and Pharmaceutical Bulletin **35**, 1447-1453 (2012).

215. W. D. Butt and D. Keilin, "Absorption Spectra and Some Other Properties of Cytochrome c and of Its Compounds with Ligands," Proceedings of the Royal Society of London. Series B, Biological Sciences **156**, 429-458 (1962).

216. Y.-L. P. Ow, D. R. Green, Z. Hao, and T. W. Mak, "Cytochrome c: functions beyond respiration," Nature Review Molecular Cell Biology **9**, 532-542 (2008).

217. E. Margoliash and N. Frohwirt, "Spectrum of horse-heart cytochrome c," Biochemistry Journal **71**, 570-572 (1959).

218. P. L. Vandewalle and N. O. Petersen, "Oxidation of reduced cytochrome c by hydrogen peroxide. Implications for superoxide assays," **210**, 195-198 (1987).

219. V. J. Cadarso, G. Smolik, V. Auzelyte, L. Jacot-Descombes, and J. Brugger, "Heterogeneous material micro-transfer by ink-jet print assisted mould filling," Microelectronic Engineering **98**, 619-622 (2012).

220. A. Tuteja, W. Choi, M. Ma, J. M. Mabry, S. A. Mazzella, G. C. Rutledge, G. H. McKinley, and R. E. Cohen, "Designing Superoleophobic Surfaces," Science **318**, 1618-1622 (2007).

221. V. Koman, G. Suárez, C. Santschi, V. J. Cadarso, J. Brugger, N. von Moos, V. I. Slaveykova, and O. J. F. Martin, "A portable microfluidic-based biophotonic sensor for extracellular H_2O_2 measurements," Proceedings SPIE **8572**, 857218 (2013).

222. J. A. Findlay and R. Dillard, "Appropriate calibration curve fitting in ligand binding assays," American Association Pharmaceutical Science Journal **9**, E260-E267 (2007).

223. G. Kim, Y.-E. Lee, and R. Kopelman, "Hydrogen Peroxide (H_2O_2) Detection with Nanoprobes for Biological Applications: A Mini-review," in *Oxidative Stress and Nanotechnology*, D. Armstrong and D. J. Bharali, eds. (Humana Press, 2013), pp. 101-114.

224. F. Haber and J. Weiss, "Über die Katalyse des Hydroperoxydes," Naturwissenschaften **20**, 948-950 (1932).

225. J. K. Gregory and D. C. Clary, "Calculations of the tunneling splittings in water dimer and trimer using diffusion Monte Carlo," The Journal of Chemical Physics **102**, 7817-7829 (1995).

226. C. Kirchner, T. Liedl, S. Kudera, T. Pellegrino, A. Muñoz Javier, H. E. Gaub, S. Stölzle, N. Fertig, and W. J. Parak, "Cytotoxicity of Colloidal CdSe and CdSe/ZnS Nanoparticles," Nano Letters **5**, 331-338 (2004).

227. L. Clément, C. Hurel, and N. Marmier, "Toxicity of TiO_2 nanoparticles to cladocerans, algae, rotifers and plants – Effects of size and crystalline structure," Chemosphere **90**, 1083-1090 (2013).

228. S. A. Gerber, C. R. Scott, F. Turecek, and M. H. Gelb, "Analysis of Rates of Multiple Enzymes in Cell Lysates by Electrospray Ionization Mass Spectrometry," Journal of the American Chemical Society **121**, 1102-1103 (1999).

229. J. Homola, H. B. Lu, G. G. Nenninger, J. Dostálek, and S. S. Yee, "A novel multichannel surface plasmon resonance biosensor," Sensors and Actuators B: Chemical **76**, 403-410 (2001).

230. A. Liesener and U. Karst, "Monitoring enzymatic conversions by mass spectrometry: a critical review," Analytical and Bioanalytical Chemistry **382**, 1451-1464 (2005).

231. C. G. Pheeney, A. R. Arnold, M. A. Grodick, and J. K. Barton, "Multiplexed Electrochemistry of DNA-Bound Metalloproteins," Journal of the American Chemical Society **135**, 11869-11878 (2013).

232. M.-C. Shin, H. C. Yoon, and H.-S. Kim, "In situ biochemical reduction of interference in an amperometric biosensor with a novel heterobilayer configuration of polypyrrole/glucose oxidase/horseradish peroxidase," Analytica Chimica Acta **329**, 223-230 (1996).

233. V. B. Koman, C. Santschi, N. R. von Moos, V. I. Slaveykova, and O. J. F. Martin, "Portable oxidative stress sensor: Dynamic and non-invasive measurements of extracellular H_2O_2 released by algae," Biosensors and Bioelectronics **68**, 245-252 (2015).

234. K. A. Johnson and R. S. Goody, "The Original Michaelis Constant: Translation of the 1913 Michaelis–Menten Paper," Biochemistry **50**, 8264-8269 (2011).

235. B. Messner, C. Ploner, G. Laufer, and D. Bernhard, "Cadmium activates a programmed, lysosomal membrane permeabilization-dependent necrosis pathway," Toxicology Letters **212**, 268-275 (2012).

236. K. C. Leptos, J. S. Guasto, J. P. Gollub, A. I. Pesci, and R. E. Goldstein, "Dynamics of Enhanced Tracer Diffusion in Suspensions of Swimming Eukaryotic Microorganisms," Physical Review Letters **103**, 198103 (2009).

237. J. El-Ali, P. K. Sorger, and K. F. Jensen, "Cells on chips," Nature **442**, 403-411 (2006).

238. S. N. Bhatia and D. E. Ingber, "Microfluidic organs-on-chips," Nature Biotechnology **32**, 760-772 (2014).

239. T. Thorsen, S. J. Maerkl, and S. R. Quake, "Microfluidic Large-Scale Integration," Science **298**, 580-584 (2002).

240. Q. Ramadan and M. M. Gijs, "Microfluidic applications of functionalized magnetic particles for environmental analysis: focus on waterborne pathogen detection," Microfluidics and Nanofluidics **13**, 529-542 (2012).

241. C. Huang, Q. Ramadan, J. B. Wacker, H. C. Tekin, C. Ruffert, G. Vergeres, P. Silacci, and M. A. M. Gijs, "Microfluidic chip for monitoring Ca2+ transport through a confluent layer of intestinal cells," RSC Advances **4**, 52887-52891 (2014).

242. V. K. Parashar, J. B. Wacker, D. Necula, and M. A. M. Gijs, "A microfluidic process for on-chip formation of assemblies of oxide nanoparticles," Royal Society of Chemistry Advances **4**, 36725-36728 (2014).

243. V. Sivagnanam and M. A. M. Gijs, "Exploring Living Multicellular Organisms, Organs, and Tissues Using Microfluidic Systems," Chemical Reviews **113**, 3214-3247 (2013).

244. T. C. Hausherr, H. Majd, D. Joss, A. Müller, D. P. Pioletti, M. A. M. Gijs, and C. Yamahata, "Capillary-valve-based platform towards cell-on-chip mechanotransduction assays," Sensors and Actuators B: Chemical **188**, 1019-1025 (2013).

245. J. Wu, Q. Chen, W. Liu, Y. Zhang, and J.-M. Lin, "Cytotoxicity of quantum dots assay on a microfluidic 3D-culture device based on modeling diffusion process between blood vessels and tissues," Lab on a Chip **12**, 3474-3480 (2012).

246.   K. Zhang, C.-K. Chou, X. Xia, M.-C. Hung, and L. Qin, "Block-Cell-Printing for live single-cell printing," Proceedings of the National Academy of Sciences **111**, 2948-2953 (2014).

247.   Y. Liu, W. B. Butler, and D. Pappas, "Spatially selective reagent delivery into cancer cells using a two-layer microfluidic culture system," Analytica Chimica Acta **743**, 125-130 (2012).

248.   M. Tehranirokh, A. Z. Kouzani, P. S. Francis, and J. R. Kanwar, "Microfluidic devices for cell cultivation and proliferation," Biomicrofluidics **7**, 150 (2013).

249.   S. Dar-Bin, H. Chia-Chun, H. Song-Bin, and L. Gwo-Bin, "A microfluidic-based cell culture platform for cellular and subcellular imaging," in *Nano/Micro Engineered and Molecular Systems, 2009. NEMS 2009. 4th IEEE International Conference on*, 2009), 223-226.

250.   J. L. Garcia-Cordero and S. J. Maerkl, "A 1024-sample serum analyzer chip for cancer diagnostics," Lab on a Chip **14**, 2642-2650 (2014).

251.   P. J. Keeling, "Diversity and evolutionary history of plastids and their hosts," American Journal of Botany **91**, 1481-1493 (2004).

252.   S. Sabella, R. P. Carney, V. Brunetti, M. A. Malvindi, N. Al-Juffali, G. Vecchio, S. M. Janes, O. M. Bakr, R. Cingolani, F. Stellacci, and P. P. Pompa, "A general mechanism for intracellular toxicity of metal-containing nanoparticles," Nanoscale **6**, 7052-7061 (2014).

253.   R. F. Domingos, D. F. Simon, C. Hauser, and K. J. Wilkinson, "Bioaccumulation and Effects of CdTe/CdS Quantum Dots on Chlamydomonas reinhardtii – Nanoparticles or the Free Ions?," Environmental Science & Technology **45**, 7664-7669 (2011).

254.   C. H. Foyer and G. Noctor, "Redox Homeostasis and Antioxidant Signaling: A Metabolic Interface between Stress Perception and Physiological Responses," The Plant Cell Online **17**, 1866-1875 (2005).

255.   M. Hanikenne, S. S. Merchant, and P. Hamel, "Chapter 10 - Transition Metal Nutrition: A Balance Between Deficiency and Toxicity," in *The Chlamydomonas Sourcebook (Second Edition)*, E. H. H. B. S. B. Witman, ed. (Academic Press, London, 2009), pp. 333-399.

256.   C. Lamelas, J. P. Pinheiro, and V. I. Slaveykova, "Effect of Humic Acid on Cd(II), Cu(II), and Pb(II) Uptake by Freshwater Algae: Kinetic and Cell Wall Speciation Considerations," Environmental Science & Technology **43**, 730-735 (2009).

257.   Y. Wang, J. Fang, S. S. Leonard, and K. M. Krishna Rao, "Cadmium inhibits the electron transfer chain and induces Reactive Oxygen Species," Free Radical Biology and Medicine **36**, 1434-1443 (2004).

258.   V. I. Slaveykova and K. Startchev, "Effect of natural organic matter and green microalga on carboxyl-polyethylene glycol coated CdSe/ZnS quantum dots stability and transformations under freshwater conditions," Environmental Pollution **157**, 3445-3450 (2009).

259.   X. He, Y. Pan, J. Zhang, Y. Li, Y. Ma, P. Zhang, Y. Ding, J. Zhang, Z. Wu, Y. Zhao, Z. Chai, and Z. Zhang, "Quantifying the total ionic release from nanoparticles after particle-cell contact," Environmental Pollution **196**, 194-200 (2015).

260.   Y. Bae, N. Myung, and A. J. Bard, "Electrochemistry and Electrogenerated Chemiluminescence of CdTe Nanoparticles," Nano Letters **4**, 1153-1161 (2004).

261.   H. Jiang and H. Ju, "Enzyme-quantum dots architecture for highly sensitive electrochemiluminescence biosensing of oxidase substrates," Chemical Communications, **5**, 404-406 (2007).

262.   L. Dennany, M. Gerlach, S. O'Carroll, T. E. Keyes, R. J. Forster, and P. Bertoncello, "Electrochemiluminescence (ECL) sensing properties of water

soluble core-shell CdSe/ZnS quantum dots/Nafion composite films," Journal of Materials Chemistry **21**, 13984-13990 (2011).

263. X. Hu, H. Han, L. Hua, and Z. Sheng, "Electrogenerated chemiluminescence of blue emitting ZnSe quantum dots and its biosensing for hydrogen peroxide," Biosensors and Bioelectronics **25**, 1843-1846 (2010).

264. P. Reiss, M. Protière, and L. Li, "Core/Shell Semiconductor Nanocrystals," Small **5**, 154-168 (2009).

265. S. Dutta-Gupta and O. J. F. Martin, "Strongly coupled bio-plasmonic system: Application to oxygen sensing," Journal of Applied Physics **110**, 044701 (2011).

266. Y. Choi, Y. Park, T. Kang, and L. P. Lee, "Selective and sensitive detection of metal ions by plasmonic resonance energy transfer-based nanospectroscopy," Nature Nanotechnology **4**, 742-746 (2009).

267. G.-Y. Liou and P. Storz, "Reactive oxygen species in cancer," Free Radical Research **44**, 479-496 (2010).

268. L. Raj, T. Ide, A. U. Gurkar, M. Foley, M. Schenone, X. Li, N. J. Tolliday, T. R. Golub, S. A. Carr, A. F. Shamji, A. M. Stern, A. Mandinova, S. L. Schreiber, and S. W. Lee, "Selective killing of cancer cells by a small molecule targeting the stress response to ROS," Nature **475**, 231-234 (2011).

269. D. Trachootham, J. Alexandre, and P. Huang, "Targeting cancer cells by ROS-mediated mechanisms: a radical therapeutic approach?," Nature Review Drug Discovery **8**, 579-591 (2009).

270. J. J. Foti, B. Devadoss, J. A. Winkler, J. J. Collins, and G. C. Walker, "Oxidation of the Guanine Nucleotide Pool Underlies Cell Death by Bactericidal Antibiotics," Science **336**, 315-319 (2012).

271. J. H. Doroshow and K. J. A. Davies, "Comparative cardiac oxygen radical metabolism by anthracycline antibiotics, mitoxantrone, bisantrene, 4'-(9-acridinylamino)-methanesulfon-m-anisidide, and neocarzinostatin," Biochemical Pharmacology **32**, 2935-2939 (1983).

272. R. T. Dorr, "Bleomycin pharmacology: mechanism of action and resistance, and clinical pharmacokinetics," Seminars in Oncology **19**, 3-8 (1992).

Behind the scene

A coup de foudre in French means to fall in love suddenly, fiercely. That is what happened with me and EPFL.

EPFL is one of the world's top universities and NAM is a group known worldwide for nanophotonics and plasmonics, therefore I am very proud to conduct my PhD among the best. All of this became possible thanks to the NAM leader, a person who accepted me as a PhD, Prof. Olivier Martin. Olivier, thank you very much for introducing me to MMP and Monte Carlo simulations, for finding spotting robot for me, for your writing guidelines, for sharing your vision on microfluidic chips and many other things, which didn't fit in here. Thank you for supporting me when my experiments did not work and my papers were rejected. Despite this bumpy road through physics, engineering and biology, I think that we achieved some fascinating results and had our victories. This work would not be possible without a generous support from the Swiss National Science Foundation in the framework of NRP 64 "Opportunities and risks of nanomaterials" project.

Enrico Fermi once noted: "If the result confirms the hypothesis, then you've made a measurement. If the result is contrary to the hypothesis, then you've made a discovery". In the beginning of my PhD, despite all my attempts to perform a measurement, I was always ending up with a discovery. Luckily, in addition to Olivier, I had two more amazing supervisors, who actually initiated this incredible merge of random media and oxidative stress: Dr. Christian Santschi and Dr. Guillaume Suarez. I am very thankful to Guillaume, who spent a lot of time with me in the lab and introduced me to all the know-hows and tricks of doing biological experiments. Christian is always open for scientific discussions and his insightful questions and discussions greatly improved my understanding of random media and oxidative stress. His enormous experience in experiments helped me to design various devices presented in this thesis. Overall, Christian crafted in me a spirit of an adept experimentalist.

The thesis examination is the final accord in every PhD. Therefore, many students are extremely nervous about it. And once it's done, they try to forget it like it was a bad dream. As for me, I really enjoyed my PhD examination and I think about it only with the smile. Prof. Gehr, Prof. Gijs and Prof. Muskens had tough and insightful questions, but everything was done in the atmosphere of friendly scientific discussion. I am extremely thankful to them for this great experience and for reading my thesis.

I believe that the person is heavily influenced by others around. In this sense, I was extremely lucky to work in the group of very talented, smart and bright guys. In my mind, Krishnan is always open to scientific discussions and helped me a lot in my scientific writings. Andrea is an example of professionalism and introduced me to microfluidics. Shourya is always there, taught me a lot about simulations, microscopy, and biology; I will be always astonished by his broad and deep knowledge. I am really indebted to Raziman, who is super-smart, super-nice and proof-read this entire thesis! Kuang-Yu and Mohsen are two guys who are always ready for the late night sessions in the clean room and week-end experiments with two-photon microscopy. My abstract is in French thanks to sincere help of Gabriel and Jeremy. Chen and Robert, I really enjoy our trips, original ideas and awesome company during lunch. Even though we rarely see Xiaolong, we all know he is somewhere in the cleanroom. It was a pleasure to transfer my biosensing knowledge to our new members and simply great guys: Madasamy and Bastien. I was also extremely lucky to have great collaborators: Nadia, who brought algae and taught me biology; Oriol, who opened for me the world of 2D materials; Prof. Vera Slaveykova, Dr. Paul Bowen and Prof. Andras Kis. I am very grateful to Prof. Sebastian Maerkl for the utilization of the microarray robot, to Dr. Victor Cadarso and Prof. Jurgen Brugger for the utilization of the ink-jet spotter, to Prof. Christof Holliger for the access to the algae incubator, to Dr. Alexandre de Titta for the access to the plate reader, to Ms. Elena Cano for the autoclave and to Mr. Sylvain Coudret for assistance with ICP-MS. Finally, special thanks go to David and to our awesome secretaries Beatrice, Cathy and Pierrette.

Sharing a home with others has been one of my greatest experiences. It was very nice to chat, relax, travel and simply rest from my thesis in the company of my nice roommates: Benjamin, Kana and Helene. I am also greatly indebted to my previous roommates, Alain and Antonin, who became one of my best friends in Switzerland and who made me feel at home. A special thanks goes to Anh for her nice food and for introducing me to Võ-Việt-Nam.

There are numerous small things that had huge impact on my thesis. At some point every PhD student falls into the phycological hole. I am really grateful to P. H. D. comics who were always there to tell me that I was not the only one doing PhD with a lot of problems. When I had just begun my PhD, the space between my head and the computer was the most insuperable barrier found in nature. In other words, I could not transform my thoughts into text and I was really bad at writing. Since that time I've begun to enjoy it quite a lot. Hence a big thanks goes to Prof. Kristin Sainani from Stanford University, who revolutionized my view on the writing process. Hans Christian Andersen stated that "where words fail, music speaks". Indeed, music always helped me: some great tracks have supported and motivated me during my entire PhD. In particular, this thesis was inspired by Vivaldi's ambitious and sincere Winter.

It is a great pleasure to have such family as mine, since they always supported me in all I did. It was always nice to come back to Lviv and enjoy their company. Also I am really grateful to my awesome friends, whom I haven't seen for ages, but who are always there to help me and most importantly always believe in me (even at times when I don't

believe in myself). In particular, this work would not be possible without one special friend – my fiancée. Every day of my PhD, she had to listen about all my experiments and my results. I believe that these frequent explanations helped me to rethink fundamental basics of my work and to keep my focus on what I was doing.

At the end, I believe that all of this was given by God. Therefore, I would like to end with the verse from Romans 11:36: "For from Him and through Him and for Him are all things. To Him be the glory forever! Amen."

Route du Pavement, 1
1018 Lausanne, Switzerland

DOB: 28/10/1988
volodymyr.koman@epfl.ch
volodia.koman@gmail.com

VOLODYMYR B. KOMAN

EDUCATION

Oct/2011 – May/2015	*Ph. D.*, Nanophotonics and Metrology Laboratory (NAM), Swiss Federal Institute of Technology (EPFL), in the frame of NRP 64 program "Opportunities and Risks of Nanomaterials". Thesis Advisor: Prof. Olivier Martin.
Sep/2009 – Jun/2011	*Master of Science*, Erasmus Mundus Program in Photonics, Ghent University, *with the greatest distinction.*
Sep/2005 – Jun/2009	*Bachelor in Applied Physics*, Optics Specialization, Ivan Franko National University of Lviv, *with honors.*

WORK EXPERIENCE

2014	Teaching assistant for the course Optics Laboratories, EPFL.
2012 – 2014	Teaching assistant for the course Ingnieurie Optique, EPFL.
2012 – 2014	Teaching assistant for the course Advanced Optics, EPFL.
2010	Summer Internship at Semiconductor Components Group, University of Twente, July – September.
2008 – 2009	Secretary at SPIE Student Chapter, Ivan Franko National University of Lviv.
2008 – 2009	Summer Internship at Laboratory of Optoelectronics, Ivan Franko National University of Lviv, June – August both years.

SCHOLARSHIPS/AWARDS

2014	Selected to represent EPFL at GYSS 2014 with "Future with "green" nanomaterials" project.
2013	Best Poster Award at Photonics Day 2013, EPFL.
2011	Best Performance Award at Erasmus Mundus Master in Photonics.
2009 – 2011	Erasmus Mundus Master in Photonics Scholarship.
2009	SPIE Officer Travel Grant.
2009	President of Ukraine Scholarship.

PUBLICATIONS

In preparation

12. N.R. von Moos, **V.B. Koman**, C. Santschi, O.J.F. Martin, P. Bowen, L. Maurizi and V.I. Slaveykova, *The non-invasive continuous monitoring of sub-toxic oxidative stress triggered by nano-TiO$_2$ in Chlamydomonas reinhardtii* in preparation.

Submitted

11. **V.B. Koman**, N.R. von Moos, C. Santschi, V.I. Slaveykova and O.J.F. Martin, *New insights in ROS dynamics: multi-layered microfluidic chip for ecotoxical studies on aquatic microorganisms,* submitted to Nanotoxicology.

10. **V.B. Koman**, C. Santschi and O.J.F. Martin, *Novel multiplexed optical biosensors: highly sensitive, non-invasive and kinetics measurements,* submitted to Biomedical Optics Express.

9.   **V.B. Koman**, C. Santschi and O.J.F. Martin, *Maximal absorption regime in random media,* submitted to Energy Express: Optics Express.

2015

8.   **V.B. Koman**, C. Santschi, N.R. von Moos, V.I. Slaveykova and O.J.F. Martin, *Portable oxidative stress sensor: Dynamic and non-invasive measurements of extracellular H_2O_2 released by algae*, Biosensors and Bioelectronics 68, pp. 245-252 (2015), doi:10.1016/j.bios.2014.12.044.

7.* **V.B. Koman**, C. Santschi and O.J.F. Martin, *Multiscattering-enhanced absorption spectroscopy*, Analytical chemistry 87 (3), pp. 1536–1543 (2015), doi: 10.1021/ac502267q.

2014

6.** O. Lopez Sanchez, E. Alarcon Llado, **V. Koman**, A. Foncuberta i Morral, A. Radenovic and A. Kis, *Light Generation and Harvesting in a Van der Waals Heterostructure*, ACS Nano 8 (3), pp. 3042–3048 (2014), doi: 10.1021/nn500480u.

2013

5.*** **V. Koman**, G. Suarez, Ch. Santschi, V.J. Cadarso, J. Brugger, N. von Moos, V.I. Slaveykova and O.J.F. Martin, *A portable microfluidic-based biosensor for extracellular H_2O_2 measurements*, Proc. SPIE 8572, Advanced Biomedical and Clinical Diagnostic Systems XI, pp. 857281-8 (2013), doi:10.1117/12.2008329.

2010

4.   I. Polovynko, S. Rykhlyuk, **V. Koman** and V. Davydov, *Pleochroism in Potassuim Cobalt Sulfate Hexahydrate Crystals*, Ukrainian Journal of Physics 55, pp.175–180 (2010).

2009

3.   I. Polovynko, S. Rykhlyuk, **V. Koman** and I. Karbovnyk, *Modification of the optical spectra of mixed $K2Co_xNi_{1-x} (SO_4)_26H_2O$ crystals*, Journal of Applied Spectroscopy 311, pp.4704–4707 (2009), doi: 10.1007/s10812-009-9140-z.

2.   I. Polovynko, S. Rykhlyuk, I. Karbovnyk, **V. Koman**, M. Piccini and M. C. Guidi, *A new method of growing $K_2Co_xNi_{1-x}(SO_4)_2*6H_2O$ (x=0; 0.4; 0.8; 1) mixed crystals and their spectral investigation*, Journal of Crystal Growth 76, pp.116–120 (2009), doi: 10.1016/j.jcrysgro.2009.09.006.

1.   I. Polovynko, S. Rykhlyuk and **V. Koman**, *Investigation of optical absorption spectra of $K_2Mg_xNi_{1-x}(SO_4)_2·6H_2O$ crystals*, Electrical Engineering 60, pp.163–167 (2009).

NEWS HIGHLIGHTS

*   Chemical & Engineering News, 93, 2, p.24 (2015): "Polymer Beads Improve Detection Limits Of Absorption Spectroscopy".

**   EPFL News 24/04/2014: "The magic of Molybdenite: solar cells and light-emitting diodes".

*** Le Nouvelliste, p.18, 8/4/2013: "Les nanoparticules stressent les cellules, mais elles ne les tuent pas forcément".

CONFERENCES
2014

15. **V. Koman**, Ch. Santschi, O.J.F. Martin, *Measuring the optical absorption of 10 nm gold nanoparticles using multiscattering-enhanced absorption spectroscopy*

in a dielectric metamaterials, META 14, Singapore, May 20–25 2014, p. E25 (oral presentation).

14. N. von Moos, **V. Koman**, Ch. Santschi, O.J.F. Martin, V.I. Slaveykova, *Interactions between nanoparticles and aquatic microorganisms and their toxic effects at the cellular and subcellular level*, SETAC Europe 24th Annual Meeting in Basel, May 11–15 2014, p. WE178 (poster presentation).

13. O. Lopez Sanchez, E. Alarcon Llado, **V. Koman**, A. Foncuberta i Morral, A. Radenovic and A. Kis, *Light Generation and Harvesting in a Van der Waals Heterostructure*, Bulletin of the American Physical Society, Denver, USA, March 3–7 2014, p. L51 (oral presentation).

2013

12. **V. Koman**, Ch. Santschi, G. Suárez, O.J.F. Martin, *A portable platform for oxidative stress measurements*, Frontiers 2013 Symposium, Lausanne, Switzerland, June 21–22 2013, p. 14 (poster presentation).

11. **V. Koman**, G. Suárez, Ch. Santschi, V.J. Cadarso, J. Brugger, N. von Moos, V.I. Slaveykova, O.J.F. Martin, *A portable microfluidic-based biophotonic sensor for extracellular H2O2 measurements*, Proc. SPIE 8572 2013, San Francisco, USA, February 5 2013, p. 8572181–7 (oral presentation).

2012

10. **V. Koman**, G. Suarez, Ch. Santschi, V.J. Cadarso, J. Brugger and O.J.F. Martin, *A microfluidic probe for optical detection of extracellular H_2O_2,* Annual meeting of the Swiss Society for Biomedical Engineering, Lausanne, Switzerland, August 27–28 2012, p. 20 (poster presentation).

9. **V. Koman**, G. Suarez, Ch. Santschi, V.J. Cadarso, J. Brugger, V.I. Slaveykova and O.J.F. Martin, *Optical detection of extracellular H_2O_2 using multiscattering matrices*, Gordon Research Conference on Bioanalytical Sensors, Newport, USA, June 17–22 2012, p. 13 (poster presentation).

2009

8. I. Polovynko, S. Rykhlyuk, **V. Koman**, D. Klimchuk, *Tutton salts crystals K2Fe(SO4)2*6H2O as sensors for ionized radiation*, Computers in electronics: science research, Chynadievo, Ukraine, September 17–20 2009, p. 99 (oral presentation).

7. **V. Koman**, I. Polovynko, S. Rykhlyuk, *Optical investigation of Tutton salts mixed crystals*, Proc. SPIE 7212 2009, San Jose, USA, January 26–28 2009, p. 43, (poster presentation).

2008

6. **V. Koman**, I Polovynko, S. Rykhlyuk, *Optical investigation of Tutton salts mixed crystals*, IX Polish-Ukrainian Meeting and XXIX International School on Ferroelectrics physics, Kraków, Poland, September 14–18, 2008, p.9 (poster presentation).

5. I. Polovynko, S. Rykhlyuk, I. Karbovnyk, **V. Koman**, M. Piccinini, M. Cestelli Guidi, *Optical spectra investigation of K2CoxNix-1(SO4)2 6H2O (x = 0,1; 0,4; 0,8; 1)mixed crystals*, XIV-th International Seminar on Physics and Chemistry of Solids ISPCS'08, Lviv, Ukraine, June 1–4, 2008, p. 29 (oral presentation).

4. **V. Koman**, S. Rykhlyuk, *Optical absorbance in K2CoxZn1-x(SO4)2 6H2O (x = 0,1; 0,2; 0,3; 0,5; 0,6; 0,7; 1) crystals*, International conference of students and young scientists in theoretical and experimental physics HEUREKA- 2008, Lviv, Ukraine, May 19–21 2008, p. D5 (oral presentation).

3. I. Polovynko, S. Rykhlyuk, I. Karbovnyk, **V. Koman**, *Isomorphous replacement influence on optical properties of K2CoxNi1-x(SO4)2 6H2O (x = 0; 0,4; 0,8; 1) crystals*, Recent problems in electrotechnics, Lviv, Ukraine, January 31 2008, p. 51–52, (oral presentation).

2007

2. **V. Koman**, *The dependence of metal nano-clusters' surface energy on its size and structure*, International conference of students and young scientists in theoretical and experimental physics HEUREKA-2007, Lviv, Ukraine, May 22–24, 2007, p. D47 (oral presentation).

2006

1. **V. Koman**, *Research of solar photoelements on the basis of semiconductor heterostructures AlGaAs-GaAs*, International conference of students and young scientists in theoretical and experimental physics HEUREKA-2006, Lviv, Ukraine, May 15–17, 2006, p. B60 (oral presentation).

LANGUAGES

- Ukrainian   Mother tongue
- English   Fluent
- Russian   Fluent
- French   Conversational
- Polish   Conversational